MHD Wave Modes in Solar Magnetic Flux Tubes with Various Cross-Sectional Shapes

Anwar Aldhafeeri

Supervisors:
Dr Gary Verth
Dr Viktor Fedun

The University Of Sheffield.

University of Sheffield

School of Mathematics and Statistics

A thesis submitted in partial fulfilment of the requirements for the degree of

Doctor of Philosophy

February 2021

I would like to dedicate this thesis to my husband Ahmad Aldhafeeri for his continuous support and significant encouragement.

Acknowledgements

First of all, I express my great thanks to God. I want to express my heartfelt and great thanks to my two supervisors, Drs. Gary Verth and Viktor Fedun, for their support and guidance that they gave me throughout my Ph.D. I overcame many difficulties and completed this work successfully thanks to their scientific, distinctive, and wise guidance; It was a great honor and privilege for me to work under the supervision of Drs. Gary Verth and Viktor Fedun.

I want to offer my thanks to the many people for their support and advice, which made the successful completion of this thesis possible.

I want to express my deep gratitude to my advisor, Dr. Istvan Ballai, for his encouragement, continued support, and academic pieces of advice that he have provided. It was his encouragement and advice supportive of accomplishing this work.

From the bottom of my heart, I thank my parents, who have been instrumental in encouraging me to complete my Ph.D. and have always believed in me that I can accomplish this work. I thank them for all the love, giving, and support over the past years. Without you, none of this would have been possible.

I want to give special thank and gratitude to my husband, Ahmed Aldhafeeri, who accompanied me throughout my studies and was the first supporter, loyal friend, and loving husband. I thank him for his patience, happiness, and all hope that he has given to me. For everything, I dedicate this thesis to you.

I want to give special thanks to my lovely children Nora, Al Walid, and Al Maha for their love, smile, support, and happiness that they have given to me through the years. I want to thank my family and friends for their support and love specially my young sister Reem Aldhafeeri.

I want to thank Sheffield University for all support and funding for AGU meeting. I want to thank the Saudi Government, King Faisal University, the Royal Embassy, the Saudi Cultural Bureau, and the Ministry of Higher Education for my scholarship and for supporting my study.

Declaration of Authorship

I hereby declare that, except where clear reference is made to the work of others, the contents of this dissertation are original and have not, in whole or in part, been submitted to this or any other university for consideration for any other degree or qualification. This dissertation is my own work and contains nothing which is the outcome of work done in collaboration with others, except as specified in the text and Acknowledgements. This dissertation contains fewer than 80,000 words including appendices, bibliography, footnotes, tables and equations.

Anwar Aldhafeeri
February 2021

Abstract

Here we present three different models that can be tested against observed sunspot oscillations: (i) A magnetic flux tube of circular cross-sectional shape with the axis parallel to the observer's line of sight; (ii) a magnetic flux tube of elliptical cross-sectional shape with the axis parallel to the observer's line of sight; (iii) a magnetic flux tube of actual cross-sectional shape with the axis parallel to the observer's line of sight. The theory of MHD wave modes in cylindrical magnetic waveguides is well developed. In this work we will solve the dispersion relation in cylindrical magnetic waveguides using a new numerical algorithm for solving transcendental equations.

Next, we will present a model that predicts the MHD wave modes of compressible magnetic flux tubes with an elliptical cross-section. Therefore, the developed numerical algorithm is also implemented to solve the dispersion relation for elliptical magnetic waveguides. From a practical point of view the information from the resultant dispersion diagrams does not actually show what these MHD modes will actually look like in observational data. Therefore, we will illustrate the spatial structure of the eigenfunctions of these MHD wave modes to explain how the eccentricity affects different wave modes when the flux tube axis is parallel to the observers line of sight. Finally, we present a model that predicts the MHD wave modes of compressible magnetic flux tubes using the actual observed cross-sectional shape. We will illustrate the spatial structure of the eigenfunctions of these MHD wave modes and compare them with other models, i.e cylindrical and elliptical.

List of Publications

This Thesis is based on the following publications:

- MHD wave modes of solar magnetic flux tubes with elliptical cross-section, Anwar Aldhafeeri, Gary Verth, Wernher Brevis, David B. Jess, Max McMurdo and Viktor Fedun (Accepted).
- MHD wave modes of solar magnetic flux tubes with realistic cross-section, Anwar Aldhafeeri, Viktor Fedun, Gary Verth and Matthew Lennard (submitted to Apj journal).

The following publication is not included in this Thesis:

- A novel approach to identify resonant MHD wave modes in solar pores and sunspot umbrae: $B-\omega$ analysis, M. Stangalini, D. B. Jess G. Verth, V. Fedun, B. Fleck, S. Jafarzadeh, P. H. Keys, M. Murabito, D. Calchetti, A. A. Aldhafeeri, F. Berrilli, D. Del Moro, S. M. Jefferies, J. Terradas, R. Soler (Accepted).

Contents

List of Figures

CHAPTER 1

Introduction

1.1 A brief history of solar science

For more than 4.6 billion years, the Sun has provided us with energy. However, many secrets of the Sun are still a mystery for scientists, e.g., the variety of phenomena that occur on its surface such as the origin of the solar wind (see, e.g. Vaquero and Vázquez, 2009; Despois and Gargaud, 2006) and many others. Exploration of the sun and the phenomena occurring on its surface began around 2000 BC, when the first solar eclipse was recorded in China (see, e.g. Eddy, 1980; Priest, 2014). Astronomers observed some dark areas on the Sun's surface, but could not explain them. The first observation of a sunspot dated back to 800 BC in ancient Greece. The beginning of 17^{th} century can be considered a significant starting point for understanding and defining many astronomical events. In 1609, Johannes Kepler studied the heliocentric system. He expanded the study of Copernicus to include elliptical orbits of the planets around the Sun. The most important event in astronomy was when the telescope was designed by Hans Lippershey in 1609. This invention contributed to a much better understanding of many astronomical phenomena which were not possible to study before. Dark areas on the Sun were observed by Chinese astronomers or what are now known as sunspots, were the first observed telescopically in late 1610 by Galileo Galilei and Thomas Harriot (see Figure 1.1). There is still controversy about who was first to record sunspots: some references attribute the first sunspot recording to British astronomer and mathematician, Thomas Harriot, in 1610, then followed by Galileo Galilei in 1612. In the same year Galileo Galilei investigated and tracked sunspots' movement across the solar disk and concluded that the Sun rotates around its own axis. The discoveries were not limited to sunspots only. The study was extended to include many important aspects of the Sun and astronomy. In 1619, Johannes Kepler explained the orientation of comet's tails by a directed

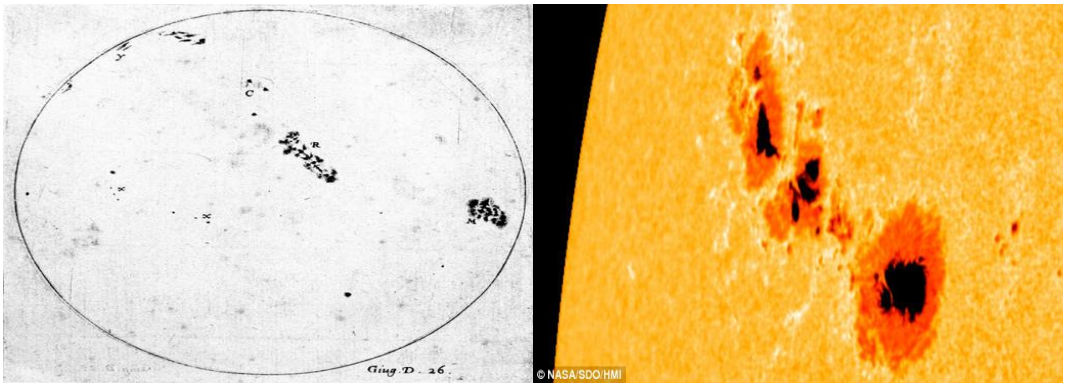

(a) Galileo Galilei: sunspots (b) Sunspots, courtesy of NASA.

Figure 1.1: Left panel: representation of a sunspot in the early seventeenth century. Right panel: a high-resolution sunspot observation courtesy of SDO/HMI.

solar wind. In the late 1660s, Isaac Newton laid the foundation for solar spectroscopy.

In the late 18^{th} century, the nebular hypothesis was formulated by Pierre Simon de Laplace in 1796. He proposed a gravitational collapse of a large, slowly rotating gas cloud to explain the solar system's formation.

In the late 19^{th} century, most studies were focused on solar spectroscopy due to the discovery of solar spectroscopy such as William Herschel, who was the first to detect the Sun's invisible infrared radiation in 1800, and Johann Wilhelm Ritter, who detected solar ultraviolet radiation in 1801. One of the most important discoveries in the middle of 19^{th} century was the Doppler effect, defined as the change in frequency of a wave due to the motion of the source detected by an observer in a different reference frame, discovered by Christian Doppler and named after him. Astronomers not only monitored sunspots, but they also went further and studied the sunspot cycle as well, which is known as the change in the number of sunspots which starts from a minimum and then increases into more sunspots (that is, about 250 sunspots) and back to a minimum again. In 1843, Samuel Heinrich Schwabe was the first astronomer who discovered the sunspot cycle and defined the 11 year sunspot period. The Swiss astronomer, Rudolf Wolf then confirmed what Schwabe found (Arlt, 2014). In 1852, Edward Sabine discussed how the sunspot cycle is directly linked to magnetic field activity. The study of sunspot distribution was also studied by Spörer, who discovered his law for sunspot distribution in 1861 (Lockyer, 1904). British astronomers Carrington and Hodgson were the first to observe a solar flare in 1859. In 1889 George Ellery Hale developed

the first spectroheliograph for the Kenwood Astrophysical Observatory. His instrument was designed to capture a photographic image of the Sun at a single wavelength of light.

The progress and development in the 20^{th} century contributed to exploring the Sun more and more accurately. Solar physics evolved during the last century due to the innovation of new and accurate telescopes and instruments. Astronomers and physicists contributed in the past two centuries to accomplishing and discovering many important phenomena in solar physics, some of them mentioned previously. Researchers in 20^{th} century followed the same path and made great progress with advanced modern spacecraft. The French solar physicist Bernard Lyot developed the first instrument (coronagraph) in 1931 that blocks out light emitted by the Sun's actual surface so that the corona can be observed. This helps to see the corona in full daylight. In 1940, the German astrophysicist Walter Grotrian observed coronal spectral lines, and the results revealed that the coronal temperature was million of degrees (Russell, 2018).

Hannes Alfvén initiated the concept of magnetohydrodynamics (MHD) and Cowling (1976) summarised the theory of MHD in his book in 1956. In 1962, Leighton discovered the five-minute oscillations in the solar photosphere (see, e.g. Leighton et al., 1962*a*). The most important achievements that revolutionised solar physics and astronomy is discovering dark absorption lines in the solar spectrum by Joseph von Fraunhofer. The spectroscope's further development has contributed greatly to providing researchers the opportunity to conduct much analysis and explain many plasma processes. Space-based solar observations began regularly in the 60's with the Orbiting Solar Observatories (OSO). This continued with the launch of the Japanese Hinotori satellite in the 80's and many others successful solar observatories such as Yohkoh (or Solar-A) satellite, Hinode (SOLAR-B), Solar Dynamics Observatory (SDO), the Interface Region Imaging Spectrograph (IRIS), and the Solar and Heliospheric Observatory (SOHO). In 1995, NASA and The European Space Agency (ESA) launched SOHO. This spacecraft provided us with many important discoveries about the solar wind and its speed. The Japanese solar observatory spacecraft Yohkoh helped us reveal the dynamic nature of the corona and magnetic reconnection in solar flares in the 1990s (Priest, 2014). In 2004, samples of solar wind particles were brought back to Earth and studied thanks to NASA's Genesis spacecraft. The Japanese spacecraft Hinode (JAXA) revealed magnetic waves in the chromosphere in 2006. The first three-dimensional images

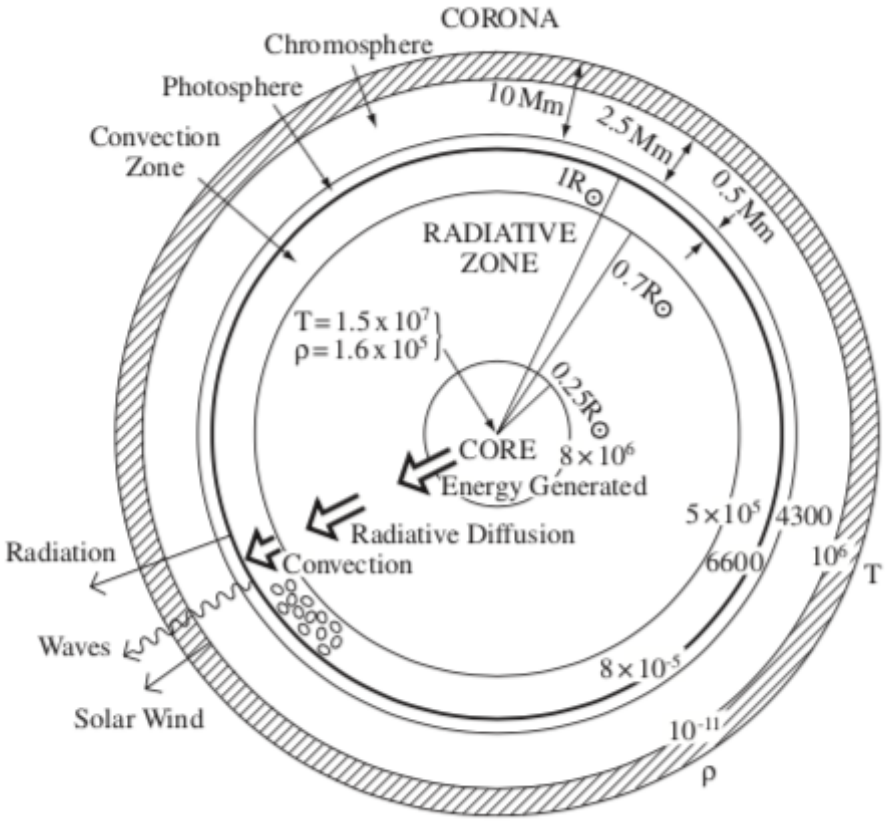

Figure 1.2: The overall structure of the Sun, courtesy of Priest (2014).

of the Sun were obtained by the double-spacecraft Solar Terrestrial Relations Observatory (STEREO) NASA mission in 2007. The remarkable development in the theory of MHD, besides ground-based observations, have provided us with an opportunity to understand the Sun better than was ever possible in the previous two centuries.

Now we live in a very exciting era of the modern ground and space-based solar observational facilities. Just recently, The Daniel K. Inouye Solar Telescope (DKIST), Solar Orbiter and Solar Parker Probe become operational. These new instruments will provide solar researchers with unprecedented hi-resolution observational data ($\approx 30km$) and will definitely lead to our better understanding of the physics of the Sun.

In the following Section, we will discuss the structure of the Sun and its atmosphere.

1.1.1 Internal structure of the Sun and its atmosphere

The Sun is a G2V main-sequence star located in the centre of the solar system. It has a diameter of about 1.39 million kilometers, or 109 times the Earth's

diameter, and it is located at about 90 million miles away from the Earth. The mass of the Sun is about 1.99×10^{30} kg. The surface gravity of the Sun is 274 ms^{-2}. One of the most important and abundant elements that make up the Sun is hydrogen, which accounts for 92% of its composition, helium, accounting for 7.8%, besides trace amounts of other heavy elements such as carbon, nitrogen, oxygen, and silicon (see, e.g. Priest, 2014). Nuclear fusion occurs in the Sun's core, and this is the source of solar energy. The hydrogen fuses into helium due to the huge pressure of up to 265 billion bar. The structure of the Sun can be divided into two parts: the interior layers and atmosphere.

In this Section, we discuss the internal and external structures of the Sun and the definition of some important phenomena and features that occur on its surface. A general description of the Sun's structure can be found, for example, in Aschwanden (2005); Priest (2014).

1.1.1.1 The solar interior

The solar interior contains three main layers: the core, radiative zone, and convection zone.

The core is located in the centre of the Sun and is the hottest and most dense part of the Sun with a temperature of about 15.7 million kelvin (K) and a density of 150 g/cm^3, which up to 150 times larger than the density of water. It contains 34% of the Sun's mass and extends from the center of the Sun to $20-25\%$ of its radius. It also has a tremendous pressure of about 265 billion bar that causes high temperatures and the fusion of hydrogen to helium, a process which will persist for about another 4 billion years. This process releases all the energy emitted from the Sun (see Figure 1.2).

The radiative Zone is the layer above the core that extends up to about 70% of the solar radius. The density of this layer varies between 20 g/cm^3 to 0.2 g/cm^3 and decreases from the bottom to the top of the radiative zone. The photons generated in the core are slowly transferred via radiation and conduction through this layer. The density of the material in this region prevents photons from travelling a long distance without colliding with another particle, causing a change in direction and losing some energy. Photons take about a million years to escape this zone (Priest, 2014). Throughout this region, the temperature drops from about 7 million K at the bottom to about 2 million K at the top (see Figure 1.2).

The convection Zone allows the transfer of heat and light through the convective process. Its depth is about 200,000 km, and it transmits energy

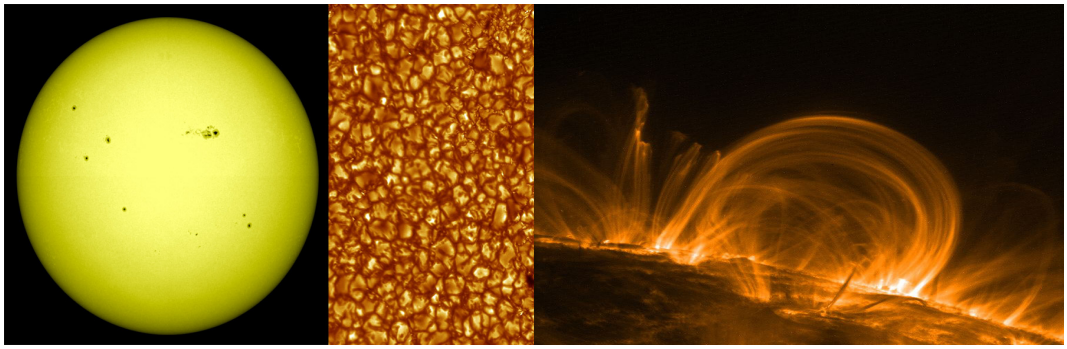

(a) Photosphere (b) Coronal loop

Figure 1.3: The left image shown the feature of photosphere such as sunspot (black region on solar atmosphere) and granules. The right image shown a coronal loop, courtesy of NASA.

from the edge of the radiation region to the Sun's surface. The plasma at the bottom is scorching, and bubbles form until they reach the surface; where they lose their heat to space. As the plasma cools, it returns to the bottom of this layer again (see Figure 1.2).

The latest model of the Sun adds one interior region called **tachocline** is thin layer containing the strong radial differential rotation at the base of the convection zone and this layer separates the radiative zone and convection zone. This layer is probably significant in the generation of the global solar magnetic field.

1.1.1.2 The solar atmosphere

The solar atmosphere is divided into four regions: photosphere, chromosphere, transition region, and corona. The physical characteristics of each region differ from the others, and based on these physical characteristics, the effect and structure of the magnetic field on each region varies. For instance, in the photosphere, plasma pressure is greater than magnetic pressure, so the plasma β, which is defined as the ratio of plasma pressure to magnetic pressure, is of order unity or larger. In contrast, in the corona, the magnetic pressure dominates, so the plasma β is small, i.e., less than one. The plasma β can be written as

$$\beta = \frac{nk_BT}{B^2/\mu_0}. \tag{1.1}$$

where μ_0 is the magnetic permeability of free space, which is defined as

$$\mu_0 = 4\pi \times 10^7 \text{ N/A}^2, \tag{1.2}$$

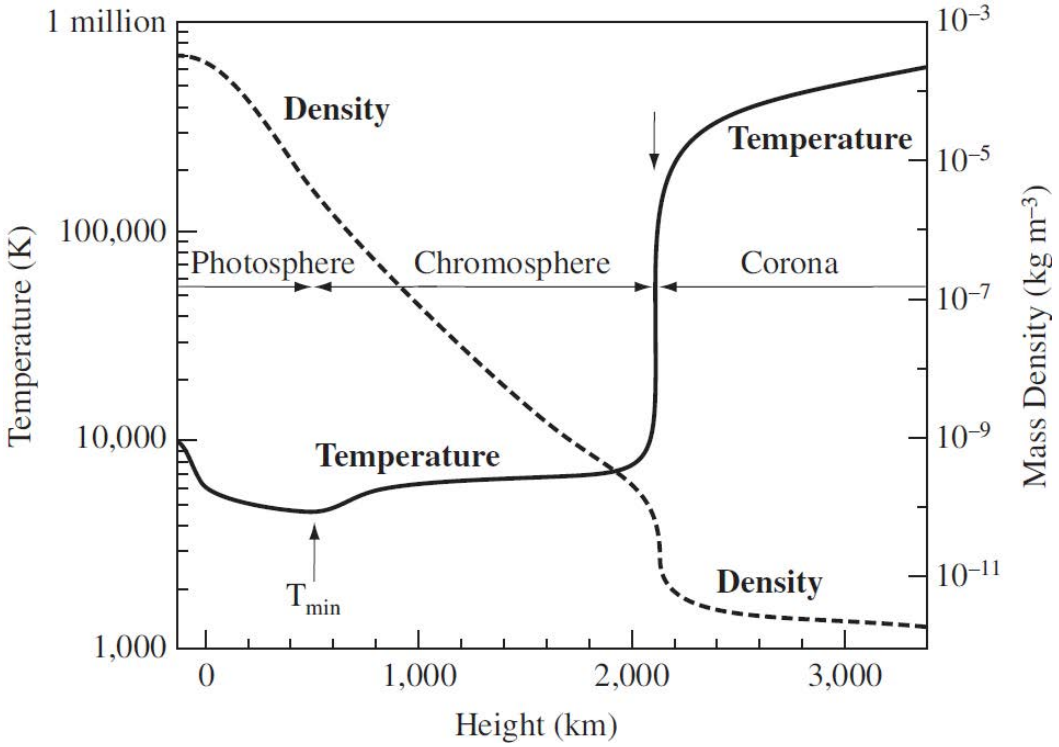

Figure 1.4: The mean variation of the density and temperature in the Sun's atmosphere, courtesy of Avrett and Loeser (2008).

$k_B \approx 1.38 \times 10^{-23}\text{JK}^{-1}$ is the Boltzmann constant, T is the temperature, and n is the total number density.

Photosphere: This is the 300 miles thick visible part of the solar atmosphere. It is the lowest layer of the Sun's atmosphere and is the most dense relative to the upper layers. The photosphere contains many features related to solar magnetic activity or convection, and is dominated by bright, bubbling granules of plasma and dark sunspots. The magnetic field mostly emanates from intergranular lanes (see Figure 1.3). **Granules** are a small convection cell pattern with a bright centre of hot rising gas and a cooler edge where the gas sinks (see Figure 1.3). Granules have an irregular shape and cover the whole photosphere. They are formed as a result of the temperature gradient near the surface of the Sun. Granules have a wide range of widths, from 0.2 Mm to 2 Mm with a lifetime of about 5 to 10 minutes. **Sunspots** are cool, darker spots than the surrounding area on the Sun's photosphere; sunspots will be discussed in more detail in Section 1.2. The photosphere emits the bulk of heat and light that reaches the Earth. The temperature of the photosphere decreases outwards (see Figure 1.4). The temperature at the bottom of the photosphere is about 6400 K, while at the top is about 4400 K.

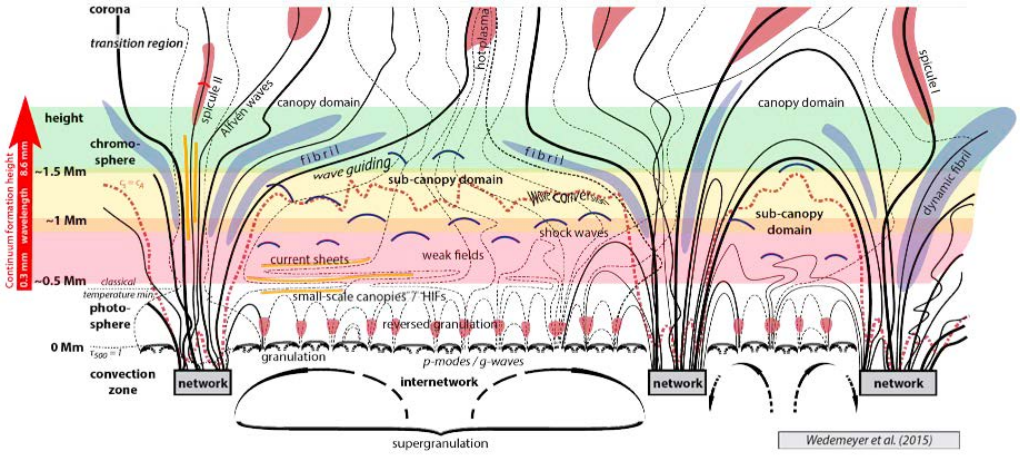

Figure 1.5: The structure of the quiet Sun lower atmosphere. The magnetic field lines are represented by the solid lines and field lines with footpoints in the internetwork are shown by thin dashed lines. Large arrows at the bottom represent large-scale convective flows and small arrows represent the flows on smaller spatial scales, courtesy of Wedemeyer-Böhm et al. (2009).

Chromosphere: The next layer that sits above the photosphere layer is known as the chromosphere which is extending to an average height of $\sim$ 2000 km above the photosphere (see Figure 1.2). The chromosphere conducts heat from the interior of the Sun to the transition region and corona. The chromospheric temperature increases and the density decreases with height. The chromospheric temperature varies between $\sim$ 4500 K and $\sim$ 20000 K with minimum of approximately $\sim$ 3800 K. The chromosphere is characterised by spicules which emerge outwards. **Spicules** are defined as plasma jets extending from the photosphere up toward the chromosphere (Bray and Loughhead, 1974; Zirin, 1998; Tavabi et al., 2012; Porfir'eva and Yakunina, 2016). The lifetime of spicules is about 15 minutes. Spicules make up one percent of the Sun's surface, and **prominences** are a dense, bright ionised gas eruptions on the Sun's surface and can extend up to thousands of kilometers from the chromosphere to corona (see, e.g. Carpmael, 1870; Lockyer and Lockyer, 1902; Buss, 1926; Aschwanden, 2005; Priest, 2014).

Transition Region: This region is known as the narrow layer between the chromosphere and solar corona where the temperature rises from about 8000 to approximately 1,000,000 K (see, e.g. Burton et al., 1971; Boehm-Vitense, 1984).

Corona: The fourth layer and the outermost part of the Sun's atmosphere is the corona. The corona is characterised by a higher temperature than the lower layers of the solar atmosphere. The Sun's corona extends millions of

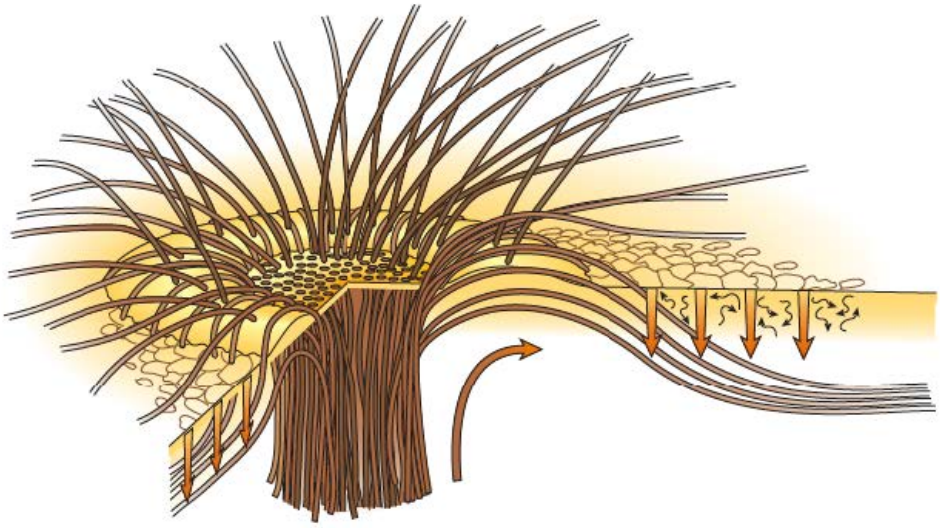

Figure 1.6: A sketch of the magnetic field topology of sunspot in the lower solar atmosphere. The brown lines shows the distribution of magnetic field lines close to solar surface for the inner circle (umbra), surrounding ring (penumbra) and granular vicinity of the spot. The arrows illustrate the convection motion. Courtesy of Thomas et al. (2002).

kilometers into external space (see, e.g. Burton et al., 1971; Boehm-Vitense, 1984; Kerr, 2012; Witze, 2017). The magnetic field dominates in the corona. The corona is structured by magnetic loops and open coronal hole regions and can be seen during a solar eclipse. Coronal loops are magnetic arcs that begin and end in the photosphere (see Figure 1.3). They may expand up to thousands of kilometers into corona with extremely high temperatures. The coronal density is about 10 million times less than Sun's surface. As a result of the low density, the corona looks much less bright than of the Sun's surface. One of the most important dilemmas in physics of the Sun is knowing the cause of the high temperature in corona (see, e.g. Peter et al., 2008; Rappazzo and Velli, 2010; Winebarger et al., 2012; Bourdin et al., 2014).

1.2 Sunspots

Our review in Section 1.1 about the crucial achievements in solar physics's history shows that sunspot observations dominated solar physics's history, being the first identifiable feature on the solar surface observed by telescopes. Sunspots are still the focus of many scientists' attention, especially studying the phenomenon of waves observed in sunspots. A brief description of the

basic structures and oscillations in sunspots will be presented next section.

1.2.1 Sunspot properties

Sunspots are defined as regions located on the Sun's surface, which are cool, darker than the surrounding, and appear where strong regions of magnetic field spread from solar interior through the surface. Sunspots are known as one of the most important features of the photosphere. Sunspots are relatively dark region because their magnetic field causes partial inhibition of convective transport of heat. Therefore, they are cooler than their surroundings with average temperatures around 3800 K while average temperatures around is 5800 K. A strongly magnetized region characterizes sunspots. A complex active region can develop due to strong magnetic field concentrations and can be classified according to the size of the sunspots, distribution, penumbra, and magnetic field properties (McIntosh, 1990). Large formations of sunspots can be seen from the ground with the naked eye without the need for a telescope (Solanki, 2003). Sunspots have a typical radius of 10 Mm to 20 Mm and consist of an umbra and a penumbra. The central dark spot is called the umbra and has a vertical magnetic field located at the centre. The typical strength of the magnetic field in an the umbra is about 2.8 kG and decreases gradually with radius (Thomas et al., 2002). The umbra's radius is about 40 percent of the whole sunspot radius. The lighter annulus surrounding the dark spot is known as penumbra and has an inclined magnetic field with a mean value of 70 to 80 degrees at the edge of the spot. The strength of the magnetic field in penumbra falls to less than 700 G to 900 G.

1.2.2 Sunspot oscillations

In the previous Section, we discussed the magnetic field configurations related to sunspots, in the umbra and penumbra of sunspot (see Figure 1.6). Through studies that have been conducted for decades on the properties of waves from the low photosphere to the high chromosphere, many important things have been proven, including that the behaviour of waves above sunspots differs in both the photosphere and the chromosphere, and the oscillations that have periods of a few minutes are most prominent in sunspots (see, e.g. Gurman et al., 1982; Kentischer and Mattig, 1995; Rouppe van der Voort et al., 2003; Centeno et al., 2006). Global oscillations were monitored with periods ranging from hours to days in sunspots.

In the following sections we will describe the main properties of waves and oscillations in the umbral and penumbral regions of sunspots.

1.2.2.1 Waves and oscillations in the umbra and penumbra

The investigation and study of solar oscillations began with the discovery of pressure waves in the photosphere (Leighton et al., 1962*b*). After detecting acoustic p-modes that propagate within the convection zone and the photosphere, important oscillations were also measured in the atmosphere of sunspots (Beckers and Tallant, 1969; Zirin and Stein, 1972). Giovanelli (1972) have classified these into three different types of oscillations,

- Five-minute oscillations in sunspots at the photospheric level,
- Three-minute oscillations and umbral flashes at the chromospheric level,
- Running penumbral waves in the penumbral chromosphere.

The periods of the characteristic p-modes peak at 5 min in the local region in the lower photosphere. Kobanov (1990) carried out observations of oscillations in six sunspots by a differential method and found that sunspot umbrae oscillates as a whole. Scheuer and Thomas (1981); Thomas and Scheuer (1982); Thomas (1984) suggested that the 3-minute photospheric oscillations, which often appear as individual peaks in velocity power spectra, might be a resonant mode of sunspots, with a cavity that could be located in the sunspot umbra at subphotospheric layers. In the umbral photosphere, three-minute oscillations were also observed. It was found that these oscillations are dominant in the chromosphere (see, e.g. Gurman et al., 1982; Kentischer and Mattig, 1995; Rouppe van der Voort et al., 2003; Centeno et al., 2006), and therefore, they have the high-frequency tail that are allowed to propagate into chromosphere (see, e.g. Bogdan and Judge, 2006). Lites (1986) found that the regions with high oscillatory power in the 3-min band were uncorrelated with those with of high oscillatory power in the 5-min band. Lites (1986) argued that the photosphere's 5-min oscillations do not drive the 3-min chromospheric oscillations. As umbral three-minute oscillations dominate in the chromosphere, many studies have focused on this type of oscillation in the chromosphere and upper photosphere. Stangalini et al. (2012) analysed magnetic pores by using IBIS observations (photospheric FeI 617.3 nm line) and found that three-minute waves are strictly confined to the umbral region and are present at the height of formation of this line. Small-scale fluctuations in sunspot umbrae were also

identified by the observing of chromospheric oscillations at high-spatial resolution (see, e.g. Socas-Navarro et al., 2009; Bharti et al., 2013; Yurchyshyn et al., 2014).

One of the largest chromospheric phenomena are running penumbral waves, which appear as bright coherent quasi-circular bands in a chromospheric line's spectral intensity. They propagate radially outward across the sunspot penumbra (see, e.g. Zirin and Stein, 1972; Giovanelli, 1972). The periodical oscillations of penumbral waves were discovered after the detection of umbral flashes. Many authors suggested that running penumbral waves could be another manifestation of slow linear conversion of magneto-acoustic-gravity (MAG) waves upwards along the inclined magnetic field (Bloomfield et al., 2007; Felipe et al., 2010). Lites (1988) analysed observations of penumbral magneto-acoustic oscillations and found that in the outer penumbra, 5-min velocity oscillations dominate. It was also shown that at photospheric heights there is a ring of minimum power halfway between the inner and the outer penumbral boundary. Besides that, the authors found that oscillations of much lower frequencies are dominant in the chromospheric region.

1.3 Magnetohydrodynamic theory

1.3.1 Properties of plasma

Plasma is the fourth, and unique state, of matter that we can describe as an ionized gas that is characterized, in general, by a mixture of neutrals, ions (positive), and electrons. Plasma can be strongly influenced by magnetic fields and high temperatures, which leads to electrons being separated from their nuclei. This results in negative and positive charges moving separately. These charges, called electrons and ions, make the plasma a good conductor of electricity that is highly affected by a magnetic field, i.e., the ions in the plasma react to magnetic fields because they are charged (the plasma is so hot that all the negatively charged electrons are removed from the atoms, leaving them with a positive charge). The most important plasma properties that can be found in a more accurate definition of plasma is that the plasma is a quasi-neutral gas of charged particles that exhibit collective behaviour (see, e.g. Jardine, 1994; Chen, 2016). Therefore, the first of the most important characteristics in which a plasma is distinguished is the medium that is electrically neutral , meaning that the number of positive and negative charges are equal and that

their overall charge densities cancel each other in equilibrium. Thus, if we assume that n_e and n_i are the number densities of electrons and ions respectively, with charge state Z, then these are locally balanced, i.e.,

$$n_e \simeq Z n_i. \tag{1.3}$$

The ion density, n_i, can be defined as,

$$n_i = \frac{\text{number of particles}}{\text{volume}}, \quad [n_i] = \text{m}^{-3}. \tag{1.4}$$

Likewise, both electron n_e and n_a neutral density can be defined in the same way. It is also worth noting that, according to Gauss's law, an electrostatic field will appear immediately in the case of a net charge imbalance. Likewise, according to Ampere's law, the same set of charges moving with specific velocities will give rise to a current density which in turn, induces a magnetic field. In addition, the net charge imbalance produces an electric field with a spatial range of the *Debye length* (see, e.g. Gurnett and Bhattacharjee, 2005),

$$\lambda_D = \sqrt{\frac{\epsilon_0 k_B T}{e^2 n}}, \tag{1.5}$$

where ϵ_0 is the permittivity of vacuum which can be written as

$$\epsilon_0 = \frac{1}{\mu_0 c^2} \approx 8.854187817... \times 10^{-12}\ \text{Fm}^{-1}, \tag{1.6}$$

and μ_0 is the magnetic permeability of free space, which is defined as

$$\mu_0 = 4\pi \times 10^7\ \text{N/A}^2, \tag{1.7}$$

with $c \approx 2.998 \times 10^8 \text{ms}^{-1}$ being the speed of light, $k_B \approx 1.38 \times 10^{-23}\text{JK}^{-1}$ is the Boltzmann constant, T is the temperature, $e = 1.6 \times 10^{-19}C$ and n is the total number density of electrons or ions.

An ionized gas with a very large number of particles in the sphere of radius λ_D can be defined as plasma. This defines the plasma parameter as

$$N_D = \frac{4}{3}\pi \lambda_D^3 n \gg 1. \tag{1.8}$$

The second property, the collective behaviour arises because the charged particles interact through long distance electromagnetic forces which means that the disturbances resulting from the long-range electromagnetic forces affect the movement of a large number of ions and electrons. This, in turn, governs collective behaviour in the response to the perturbations of electromagnetic fields (see, e.g. Chen, 1984).

1.3.1.1 Plasma criteria

Plasma forms 99 % of the visible cosmic matter between the stars and galaxies. The Sun is the most important example of an ionized gas for humankind (see, e.g. Choudhuri, 2018). The Earth is surrounded by a dense plasma called the ionosphere and interacts by a tenuous plasma called the solar wind.

The physical description of a plasma requires many important parameters such as the characteristic time scale, length scales and a minimum number of charged particles by unit volume. Therefore, there are important criteria that must be taken into account to consider an ionised gas as a plasma. The electrons oscillate as a whole around the equilibrium state due to their displacement around positive ions and electrical forces drive these oscillations. The time required for these oscillations to occur is one of the most important temporal factors in plasma. These oscillations can only develop if the oscillation period, t_p, is short compared with mean free time between collisions t_c, i.e.

$$t_p \ll t_c \quad or \quad \frac{t_c}{t_p} \gg 1, \tag{1.9}$$

where $t_p = 1/\omega_{pe}$ and ω_{pe} is electron plasma frequency which can be defined as

$$\omega_{pe} = \sqrt{\frac{n_e e^2}{m_e \epsilon_0}}, \tag{1.10}$$

where m_e is the effective electron mass.

The Debye length is one of the main spatial parameters that help in defining plasmas. If the length scale, L, of system is larger than the Debye Length, we can consider the plasma to be quasi-neutral, i.e.

$$\lambda_D \ll L. \tag{1.11}$$

The study of continuous plasma behaviour is governed by what is known as MHD theory, which treats the plasma as a single electrically conducting fluid interacting with an external magnetic field.

1.3.2 The equations of MHD

The complexity of plasma behaviour and the influence of magnetic fields makes the solar atmosphere an interesting and challenging subject to study. The MHD framework provides a good description of large scale and slow plasma

dynamics and it is restricted to phenomena that having characteristic velocity slow compared to the speed of light in vacuum. The characteristic times are much larger than the gyration time of the ions, and the characteristic length scales are much greater than ion gyro radius and mean free path length. The basic equations of MHD are a reduced form of Maxwell's equations together with Ohm's law, the gas law, and equations of mass continuity, momentum, and energy. The MHD approximation for Maxwell's equations is based on the assumption that the plasma is electrically neutral. The displacement current is negligible from Maxwell's equations since this deals with high frequency effects on much smaller timescales than the MHD approximation is valid for. Specifically, the MHD time scale is much larger than the time required for light to traverse the plasma. We begin by introducing the Maxwell's equations as following:

$$\nabla \times \mathbf{B} \quad = \quad \mu_0 \mathbf{j} + \frac{1}{c^2} \frac{\partial \mathbf{E}}{\partial t}, \tag{1.12}$$

where $\mathbf{B}$ is the magnetic field, $\mathbf{E}$ is the electric field, $\mathbf{j}$ the current density. This equation is known as Ampére's circuital law, which shows that the magnetic field could be generated by either currents or time-varying electric field.

$$\nabla \times \mathbf{E} \quad = \quad -\frac{\partial \mathbf{B}}{\partial t}, \tag{1.13}$$

$$\nabla \cdot \mathbf{E} \quad = \quad \frac{\rho^*}{\epsilon}. \tag{1.14}$$

where ρ^* the charge density. Equations (1.13) and (1.14) are the Maxwell-Faraday equations and Gauss's law for an electric field, respectively. These equations state that either electric charges or time - varying magnetic field may create an electric field.

$$\nabla \cdot \mathbf{B} \quad = \quad 0. \tag{1.15}$$

Equation (1.15) is Gauss's law for magnetism, or the solenoidal condition, which implies that there no magnetic monopoles.

The next equation is Ohm's law which shows that the current density is proportional to the total electric field. Therefore, Ohm's law links the electric, magnetic and velocity fields via the current density.

$$\mathbf{j} = \sigma(\mathbf{E} + \mathbf{v} \times \mathbf{B}), \tag{1.16}$$

where σ is electrical conductivity.

The following equation is the induction equation which links the magnetic field and velocity of an electrically conductive fluid.

$$\frac{\partial \mathbf{B}}{\partial t} = \nabla \times (\mathbf{v} \times \mathbf{B}) + \eta \nabla^2 \mathbf{B}, \tag{1.17}$$

where $\eta = 1/\mu_0 \sigma$ is the magnetic diffusivity.

The mass continuity equation is the equation for the evolution of the density, which can written as follwing

$$\frac{d\rho}{dt} = -\rho \nabla \cdot \mathbf{v}, \tag{1.18}$$

where $\mathbf{v}$ is velocity of a plasma. The last equation is the energy equation which states that the rate of increase heat for unit volume as it moves in space is due to the net effect of the energy sinks and sources.

$$\rho \mathbf{T} \frac{ds}{dt} = -\mathcal{L}, \tag{1.19}$$

where $\mathcal{L}$ is the energy loss function, T is the plasma temperature and s is the entropy per unit mass of plasma.

1.3.3 The theory of MHD waves

The interaction between plasma and the magnetic field in the solar atmosphere supports a rich variety of complex phenomena in the Sun. One phenomenon is that this interaction excites and supports wave propagation. For example, we can observe ubiquitous MHD waves in sunspots. There are many different MHD wave modes present on the Sun as a result of different restoring forces and these have aroused the interest of many researchers. To properly analyse and understand the behaviour of MHD waves that we observe in the solar atmosphere we should find the relevant wave solutions for the MHD equations.

The wave solutions of the MHD equations provide understanding for the observed behaviour of waves in the Sun's atmosphere. The ideal MHD equations which neglect viscosity, electrical resistivity, and thermal conductivity are:

$$\frac{d\rho}{dt} = -\rho \nabla \cdot \mathbf{v}, \tag{1.20}$$

$$\rho \frac{d\mathbf{v}}{dt} = -\nabla P + \rho \mathbf{g} + \frac{1}{4\pi} \left[(\nabla \times \mathbf{B}) \times \mathbf{B} \right], \tag{1.21}$$

$$\frac{d}{dt} \left(P \rho^{-\gamma} \right) = 0, \tag{1.22}$$

$$\nabla \times (\mathbf{v} \times \mathbf{B}) = \frac{\partial \mathbf{B}}{\partial t}, \tag{1.23}$$

$$\nabla \cdot \mathbf{B} = 0. \tag{1.24}$$

These equations are expressed only in terms of the variables ρ, P, $\mathbf{v}$, and $\mathbf{B}$, where ρ, P, $\mathbf{v}$, and $\mathbf{B}$ are density, pressure, velocity, and magnetic field. We start from the ideal MHD equations and rewrite them for adiabatic processes by eliminating the pressure term in Equation (1.21) using the relation $\nabla P = c_S^2 \nabla \rho$, introducing the sound speed $c_S^2 = \frac{\gamma P}{\rho}$, where γ is the ratio of specific heats and using vector identities to substitute Equation (1.24) into Equations (1.21) and (1.23). The ideal MHD equations then take the form,

$$\frac{d\rho}{dt} = -\rho \nabla \cdot \mathbf{v}, \tag{1.25}$$

$$\rho \frac{d\mathbf{v}}{dt} = -c_S^2 \nabla \rho + \rho \mathbf{g} + \frac{1}{4\pi} \left[-\frac{1}{2} \nabla B^2 + (\mathbf{B} \cdot \nabla) \mathbf{B} \right], \tag{1.26}$$

$$\frac{\partial \mathbf{B}}{\partial t} = -\mathbf{B}(\nabla \cdot \mathbf{v}) + (\mathbf{B} \cdot \nabla)\, \mathbf{v} - (\mathbf{v} \cdot \nabla)\, \mathbf{B}. \tag{1.27}$$

1.3.4 Dispersion relation

The most common method used to find the wave solutions is by linearising the ideal MHD equations. Let us set up a small perturbation from the equilibrium and investigate whether disturbances propagate as MHD waves. By neglecting the second order perturbations and the gravity term to obtain the following linearised MHD equations,

$$\frac{d\rho_1}{dt} = -\rho_0 \nabla \cdot \mathbf{v}_1, \tag{1.28}$$

$$\rho \frac{\partial \mathbf{v}_1}{\partial t} = -c_S^2 \nabla \rho_1 + \frac{1}{4\pi} \left[-\nabla (\mathbf{B}_0 \cdot \mathbf{B}_1) + (\mathbf{B}_0 \cdot \nabla) \mathbf{B}_1 \right], \tag{1.29}$$

$$\frac{\partial \mathbf{B}_1}{\partial t} = -\mathbf{B} \left(\nabla \cdot \mathbf{v}_1 \right) + (\mathbf{B}_0 \nabla \cdot)\, \mathbf{v}_1. \tag{1.30}$$

Here ρ_0, $\mathbf{v}_0$, and $\mathbf{B}_0$ are the background plasma density, velocity and magnetic field quantities and ρ_1, $\mathbf{v}_1$, and $\mathbf{B}_1$ are the perturbed quantities, correspondingly.

1.3.5 Dispersion relation of wave propagation in an unbounded and homogeneous plasma

The nature of wave propagation in an unbounded and homogeneous plasma has been discussed previously, e.g. Cowling (1976). By assuming a homogeneous

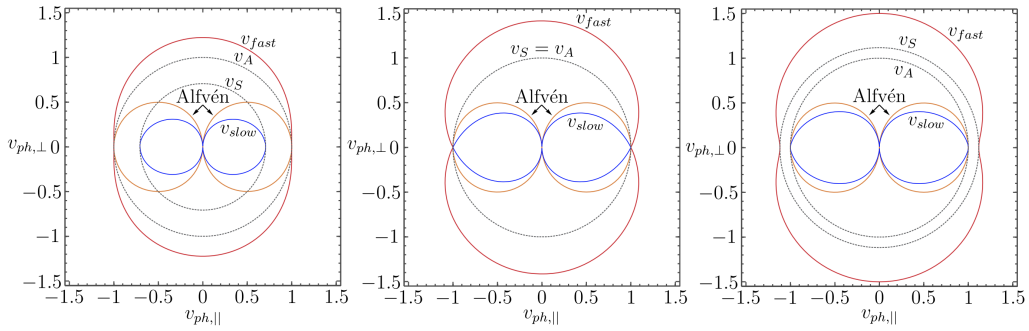

Figure 1.7: Friedrich's diagrams showing the phase speeds of the magneto-acoustic and Alfvén waves under different background conditions.

magnetic field as $B_0\hat{z}$ and the wave vector $k = (k_x, 0, k_z)$ in the xz-plane, Equations (1.28)-(1.30) can be combined as,

$$\frac{\partial^4 \Delta}{\partial t^4} - (c_S^2 + v_A^2)\frac{\partial^2}{\partial t^2}\nabla^2\Delta + c_S^2 v_A^2 \frac{\partial^2}{\partial z^2}\nabla^2\Delta = 0, \tag{1.31}$$

here $v_A = \frac{B_0}{\sqrt{\mu_0 \rho_0}}$ is the Alfvén speed and $\Delta = div\ \mathbf{v}$. In order to obtain a dispersion relation, we introduce the Fourier components $\Delta = \hat{\Delta}(x)\exp(i\omega t + ily + ikz)$. If the perturbed velocity is perpendicular to the wave vector ($\mathbf{k}\cdot\mathbf{v}_1 = 0$), we will obtain the dispersion relation which describes the Alfvén wave,

$$\omega^2 = v_A^2 k^2 \cos^2(\theta). \tag{1.32}$$

Here θ is the angle between the wavevector, $\mathbf{k}$, and the background magnetic field, $\mathbf{B_0}$. This describes an incompressible wave where the only restoring force is magnetic tension.

Allowing for compressibility ($\mathbf{k}\cdot\mathbf{v}_1 \neq 0$), we obtain the dispersion relation for fast and slow magneto-acoustic waves.

$$\omega^4 - k^2(c_S^2 + v_A^2)\omega^2 + k_z^2 k^2 c_S^2 v_A^2 \cos^2(\theta) = 0. \tag{1.33}$$

Figure 1.7 from Jess et al. (2015) illustrates the propagation of waves in a uniform unbounded magnetised plasma. It is clear that the Alfvén and the slow magneto-acoustic waves cannot propagate perpendicular to the magnetic field direction, unlike the fast magneto-acoustic waves which can. The Alfvén wave has a phase speed ($v_{ph} = \frac{\omega}{k}$) and $v_{ph} \leq v_A$ while the slow magneto-acoustic wave has a phase speed $0 \leq v_{ph} \leq min(c_S, v_A)$. The fast magneto-acoustic wave has a phase speed $max(c_S,\ v_A) \leq v_{ph} \leq (c_S^2 + v_A^2)^{\frac{1}{2}}$.

1.3.6 Dispersion relations of MHD wave propagation in a magnetically structured atmosphere

Wave propagation in an unbounded homogeneous plasma has features that are completely different from those which propagate in a bounded and inhomogeneous plasma. Inhomogeneity and the structure of the plasma can have a very strong influence on the propagation of waves. Therefore, it is important to study wave propagation in bounded inhomogeneous plasma configurations. Previous models for different solar features include the magnetic interface, magnetic slab and magnetic cylinder. These simple but instructive models provided the basis for understanding, e.g waves observed in coronal loops. All these cases will be covered in the next sections.

1.3.6.1 MHD surface waves at magnetic interface

High-resolution images of the Sun show that there are very inhomogeneous regions of plasma e.g., at the edge of sunspots and coronal loops. A basic model for plasma inhomogeneity is to have plasma parameters changing discontinuously at some spatial location. One such example of an inhomogeneous plasma structure is a discontinuity interface. Wentzel (1979) investigated the effect of compressibility on the propagation of surface waves at a single interface and derived an expression for the energy carried by such waves. This study obtained the dispersion relation for isothermal disturbances but he did not investigate the solutions as fully as Roberts (1981*a*), who provided a more general understanding of wave propagation at a magnetic interface. Roberts (1981*a*) derived the dispersion relation for surface wave propagation in a sharply structured plasma. The dispersion relation governing wave propagation at a magnetic interface discussed by Roberts (1981*a*) is,

$$\rho_i(k^2v_{Ai}^2-\omega^2)(m_e^2+l^2)^{\frac{1}{2}}+\rho_e(k^2v_{Ae}^2-\omega^2)(m_i^2+l^2)^{\frac{1}{2}}=0, \tag{1.34}$$

where,

$$m_i^2 = \frac{(k^2c_{Si}^2-\omega^2)(k^2v_{Ai}^2-\omega^2)}{(c_{Si}^2+v_{Ai}^2)(k^2c_T^2-\omega^2)}, \tag{1.35}$$

$$m_e^2 = \frac{(k^2c_{Se}^2-\omega^2)(k^2v_{Ae}^2-\omega^2)}{(c_{Se}^2+v_{Ae}^2)(k^2c_{Te}^2-\omega^2)}, \tag{1.36}$$

$$c_{Ti}^2 = \frac{c_{Si}^2v_{Ai}^2}{c_{Si}^2+v_{Ai}^2}, \tag{1.37}$$

$$c_{Te}^2 = \frac{c_{Se}^2v_{Ae}^2}{c_{Se}^2+v_{Ae}^2}. \tag{1.38}$$

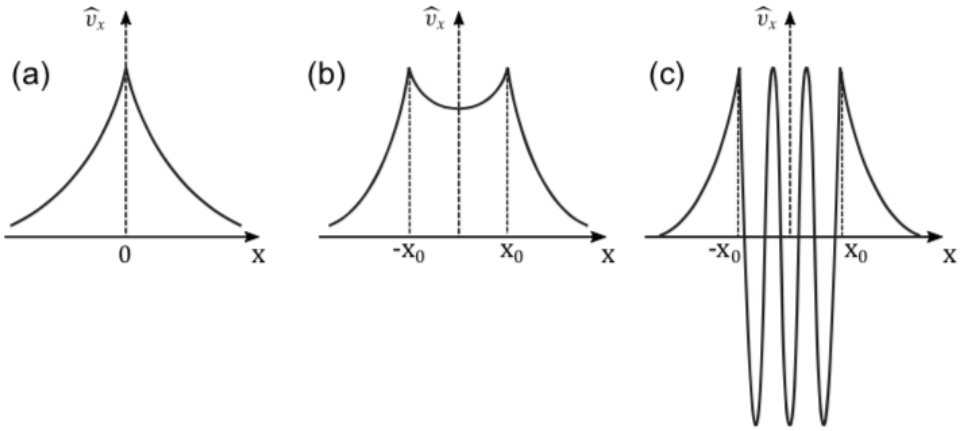

Figure 1.8: A schematic picture the profile of the velocity amplitude for (a) trapped waves on an interface; (b) surface waves in a slab; (c) body waves in a slab. Adapted from (Priest, 2014).

Here, c_T is tube speed and the subscripts i and e refer to the different neighbouring regions.

Roberts (1981*a*) found that slow surface waves can propagate only when one side of the interface is field free. In addition, fast surface waves may propagate if the plasma in one region is cooler than the other. Such "trapped" surface waves have the general property that their wave amplitude and energy decrease with increasing distance from the magnetic interface (see Figure 1.8).

1.3.6.2 MHD waves in a magnetic slab

The second example of waves propagation in a sharply structured atmosphere is an isolated magnetic slab. The behaviour of MHD waves that propagate in slab has been discussed previously by many authors. For instance, Parker (1974) described the occurrence of surface waves in an isolated slab for an incompressible plasma. Cram and Wilson (1975) studied wave propagation in a compressible slab. Interestingly they showed that the fast wave is not a free mode of vibration of the slab. Roberts (1981*b*) found that the result of Cram and Wilson (1975) was only true if the slab was warmer than its field-free environment. Roberts (1981*b*) derived the dispersion relation governing MHD wave propagation in an isolated magnetic slab of width $2x_0$,

$$(k^2 v_{Ai}^2 - \omega^2) m_e = \frac{\rho_e}{\rho_i} \omega^2 m_i \begin{pmatrix} \tanh \\ \coth \end{pmatrix} (m_i x_0), \tag{1.39}$$

where,

$$m_e^2 \;=\; k^2 - \frac{\omega^2}{c_{Se}^2}. \tag{1.40}$$

Roberts (1981*b*) found that there are two main magneto-acoustic modes, the sausage and kink modes, that have various sub-categories, e.g. slow/fast body and surface waves (see Figure 1.8). The fast magneto-acoustic wave propagates only if the slab is cooler than or equal to the temperature the field-free environment.

CHAPTER 2

Solar atmospheric magnetohydrodynamic wave modes in magnetic flux tubes of circular cross-sectional shape

2.1 MHD waves in a magnetic cylinder

Edwin and Roberts (1983) provided a simple but instructive model for coronal loops and flux tubes by analysing wave propagation in a magnetic cylinder by considering a straight magnetic ($\mathbf{B}_{0i} = B_{0i}\ \mathbf{z}$) flux tube with circular cross-section embedded within a uniform magnetic field ($\mathbf{B}_{0e} = B_{0e}\ \mathbf{z}$). Here, $\mathbf{z}$ is the unit vector in the z direction, which is parallel to the flux tube axis; index 0 corresponds to the unperturbed equilibrium state; all dependent variables inside the flux tube have index i, while quantities outside the tube are denoted with index e. The flux tube boundary is defined by r_a.

The linear equation governing magnetohydrodynamic modes can be found in Section 1.3.3. Linear perturbations about this equilibrium lead to the Equations (1.28-1.30) in Section 1.3.4 (see, e.g. Lighthill, 1960; Cowling, 1976; Roberts, 1981*a*; Aschwanden, 2005) and they can be combined to obtain:

$$\frac{\partial^4 \Delta}{\partial t^4} - (c_S^2 + v_A^2)\frac{\partial^2}{\partial t^2}\nabla^2\Delta + c_S^2 v_A^2 \frac{\partial^2}{\partial z^2}\nabla^2\Delta = 0. \tag{2.1}$$

In the cylindrical coordinate system ($r,\ \theta,\ z$) the Laplace operator can be represented as,

$$\nabla^2 = \frac{\partial^2}{\partial r^2} + \frac{1}{r}\frac{\partial}{\partial r} + \frac{1}{r^2}\frac{\partial^2}{\partial \theta^2} + \frac{\partial^2}{\partial z^2}. \tag{2.2}$$

The solution of Equation (2.1) takes the form,

$$\Delta = R(r)\exp(i(\omega t + n\theta + kz)), \tag{2.3}$$

where k is the wavenumber in z direction, n is the azimuthal wavenumber in θ direction, ω is the angular frequency and the function $R(r)$ is to be determined. By substituting Equation (2.3) in Equations (1.28-1.30) which can be written

in term of $\nabla \cdot \mathbf{v}$, the perturbed MHD variables in the cylindrical coordinate system can be derived explicitly as (see e.g. Spruit, 1982*a*),

$$v_r = A\frac{\omega^2 - k^2c_S^2}{\omega^2 m_i^2}\frac{d}{dr}\mathfrak{B}_\mathfrak{n},$$

$$v_\theta = iA\frac{\omega^2 - k^2c_S^2}{\omega^2 m_i^2}\frac{n}{r}\mathfrak{B}_\mathfrak{n},$$

$$v_z = -A\frac{ikc_S^2}{\omega^2}\mathfrak{B}_\mathfrak{n},$$

$$b_r = -B_0\frac{k}{\omega}v_r,$$

$$b_\theta = B_0\frac{k}{\omega}v_\theta,$$

$$b_z = iAB_0\frac{\omega^2 - k^2c_S^2}{\omega^3}\mathfrak{B}_\mathfrak{n},$$

$$P = iA\rho_0\frac{c_S^2}{\omega}\mathfrak{B}_\mathfrak{n},$$

$$P_T = -\frac{i\rho_0}{\omega^3}(c_S^2 + v_A^2)(\omega^2 - k^2c_T^2)\mathfrak{B}_\mathfrak{n}.$$

Here, A is an arbitrary amplitude and the perturbed velocity components are given by $\mathbf{v} = v_r$, v_θ and v_z in the r, θ and z directions, respectively; the perturbed magnetic field components are given by b_r, b_θ and b_z. P is the pressure perturbation and P_T is the total pressure perturbation, i.e the sum of kinetic and magnetic plasma pressures. $\mathfrak{B}_\mathfrak{n}$ is the Bessel function and

$$m_i^2 = \frac{(k^2c_{Si}^2 - \omega^2)(k^2v_{Ai}^2 - \omega^2)}{(c_{Si}^2 + v_{Ai}^2)(k^2c_{Ti}^2 - \omega^2)}. \tag{2.4}$$

After substitution of Equation (2.3) into Equation (2.1) we obtain,

$$\frac{d^2R}{dr^2} + \frac{1}{r}\frac{dR}{dr} - \left(m_i^2 + \frac{n^2}{r^2}\right)R = 0, \tag{2.5}$$

2.1.1 The general solution inside the magnetic flux tube

The solution of Equation (2.5) confined within boundary r_a of magnetic flux tube, $r < r_a$, we take,

$$\Delta_i = R(r) = \begin{cases} A_i I_n(m_i r) & \mathrm{m}_i^2 > 0, \\ B_i J_n(m_i r) & \mathrm{n}_i^2 = -m_i^2 > 0. \end{cases} \tag{2.6}$$

where A_i and B_i are arbitrary constants, I_n and J_n are Bessel functions, and n is the order of Bessel functions.

2.1.2 The general solution outside of the magnetic flux tube

In order to obtain the solution outside of the magnetic flux tube ($r > r_a$), we assume that there is no propagation of energy away from, or towards the boundary of magnetic flux tube in the external region,

$$\Delta_e = R(r) = A_e K_n(m_e r), \tag{2.7}$$

where A_e is an arbitrary constant. Here K_n denotes a modified Bessel function, and n is the order of Bessel functions.

2.1.3 The general dispersion relation

Background pressure balance implies that,

$$p_{0i} + \frac{B_{0i}^2}{2\mu_0} = p_{0e} + \frac{B_{0e}^2}{2\mu_0}, \tag{2.8}$$

where p_{0i} and p_{0e} are plasma pressure inside and outside of the magnetic cylinder and B_{0i} and B_{0e} are magnetic field inside and outside of the magnetic flux tube.

By taking into account the continuity of radial velocity component, v_r, and the total (gas plus magnetic) pressure across the boundary of magnetic flux tube $r = r_a$, we obtain the dispersion relation.

- For surface waves ($m_i^2 > 0$),

$$\rho_i(k^2 v_{Ai}^2 - \omega^2) m_e \frac{K_n'(m_e r_a)}{K_n(m_e r_a)} = \rho_e(k^2 v_{Ae}^2 - \omega^2) m_i \frac{I_n'(m_i r_a)}{I_n(m_i r_a)}. \tag{2.9}$$

- For body waves ($m_i^2 = -n_i^2 < 0$),

$$\rho_i(k^2 v_{Ai}^2 - \omega^2) m_e \frac{K_n'(m_e r_a)}{K_n(m_e r_a)} = \rho_e(k^2 v_{Ae}^2 - \omega^2) n_i \frac{J_n'(n_i r_a)}{J_n(n_i r_a)}. \tag{2.10}$$

  Here, the dash denotes the derivative of Bessel functions with respect to its argument.

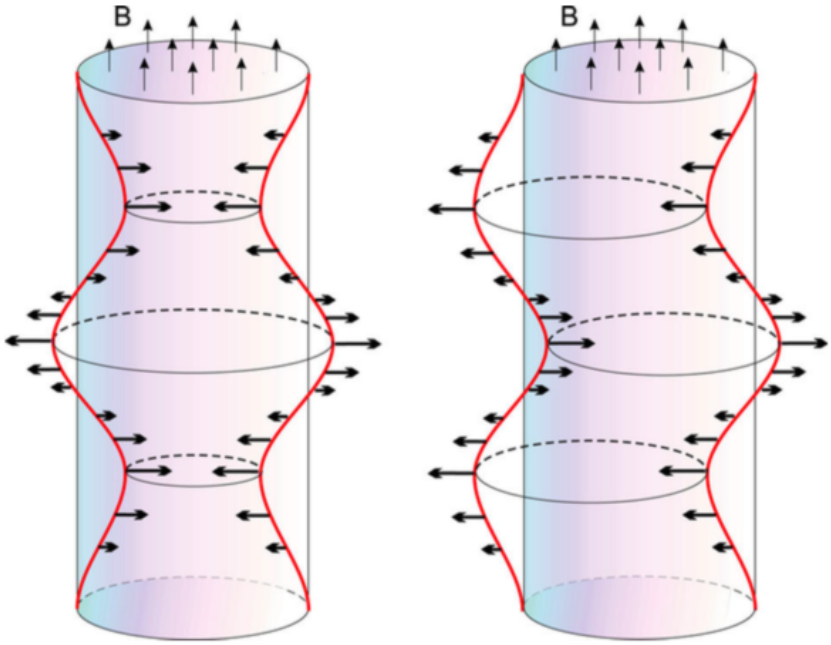

Figure 2.1: The red line cylindrical magnetic wave guides schematic diagram shows the longitudinal (sausage) and transversal (kink) modes. The left diagram illustrates the sausage wave which is excited by a periodic stretching and squeezing of the magnetic field while the right diagram illustrates the kink wave which is characterized by a displacement of the symmetry axis magnetic flux tube. The thick arrows show the velocity amplitudes and the thin arrows indicate the direction of the background magnetic field. Image takes from (Morton et al., 2012)

.

2.2 Model

2.2.1 New numerical algorithm for solving transcendental equations

We have developed a new numerical algorithm to solve developed transcendental equations with application to solving MHD dispersion relations. The routine that we developed uses the bisection method with a matrix technique to solve an equation of two variables. In addition, we can further refine the solution for each value of wavenumber.

2.2.2 Description of the method

We started by defining the boundary limits and possible wavenumbers. To do this we divided the phase speed into many intervals. Each interval has an upper, a_i, and a lower, b_j, bound. Then we applied these boundaries with

a wavenumber in two matrices so each element in the matrix represents the function values with a boundary limit and wavenumber. We created an upper matrix U which contained the function values with an upper bound and a wavenumber. We also created a lower matrix L that contained the function values with a lower bound and a wavenumber.

$$Lower\ matrix = \begin{bmatrix} f(a_1,k_1) & f(a_1,k_2) & \cdots & f(a_1,k_n) \\ f(a_2,k_1) & f(a_2,k_2) & \cdots & f(a_2,k_n) \\ \vdots & & \ddots & \\ f(a_n,k_1) & f(a_n,k_2) & \cdots & f(a_n,k_n) \end{bmatrix},$$

$$Upper\ matrix = \begin{bmatrix} f(b_1,k_1) & f(b_1,k_2) & \cdots & f(b_1,k_n) \\ f(b_2,k_1) & f(b_2,k_2) & \cdots & f(b_2,k_n) \\ \vdots & & \ddots & \\ f(b_n,k_1) & f(b_n,k_2) & \cdots & f(b_n,k_n) \end{bmatrix}.$$

Next, a multiplication was performed in which each of the elements in the upper matrix multiplied the corresponding element in lower matrix. Thus, we obtain the UL matrix.

$$UL = \begin{bmatrix} f(a_1,k_1)\cdot f(b_1,k_1) & f(a_1,k_2)\cdot f(b_1,k_2) & \cdots & f(a_1,k_n)\cdot f(b_1,k_n) \\ f(a_2,k_1)\cdot f(b_2,k_1) & f(a_2,k_2)\cdot f(b_2,k_2) & \cdots & f(a_2,k_n)\cdot f(b_2,k_n) \\ \vdots & & \ddots & \\ f(a_n,k_1)\cdot f(b_n,k_1) & f(a_n,k_2)\cdot f(b_n,k_2) & \cdots & f(a_n,k_n)\cdot f(b_n,k_n) \end{bmatrix}.$$

In addition, we created three matrices that represent the value of the upper bound and lowers bound of phase speed and wavenumber with the same dimension of the multiplication. The elements in each matrix have the same order of the equivalent elements in the multiplication e.g., matrix A and B repeat the values of the first column for all columns while the matrix K repeats the first row for all rows. The matrices created are as follows:

$$A = \begin{bmatrix} a_1 & a_1 & \cdots & a_1 \\ a_2 & a_2 & \cdots & a_2 \\ \vdots & & \ddots & \\ a_n & a_n & \cdots & a_n \end{bmatrix},$$

$$B = \begin{bmatrix} b_1 & b_1 & \cdots & b_1 \\ b_2 & b_2 & \cdots & b_2 \\ \vdots & & \ddots & \\ b_n & b_n & \cdots & b_n \end{bmatrix},$$

$$K = \begin{bmatrix} k_1 & k_2 & \cdots & k_n \\ k_1 & k_2 & \cdots & k_n \\ \vdots & & \ddots & \\ k_1 & k_2 & \cdots & k_n \end{bmatrix}.$$

After the multiplication, we looked for where the multiplication has a negative sign and determine the location of these signs to extract the values from matrix A, matrix B and matrix K. Then, we put the values extracted in three arrays for A, B and K to test them and find solutions. Then we implemented the bisection method to test only these elements in the three arrays because we knew that only these elements satisfy the condition that the multiplication of the function at the upper bound with the lower bound is less than zero. The method works by picking up each element of these three arrays and then moving to the next element until all elements are tested and the solution is found.

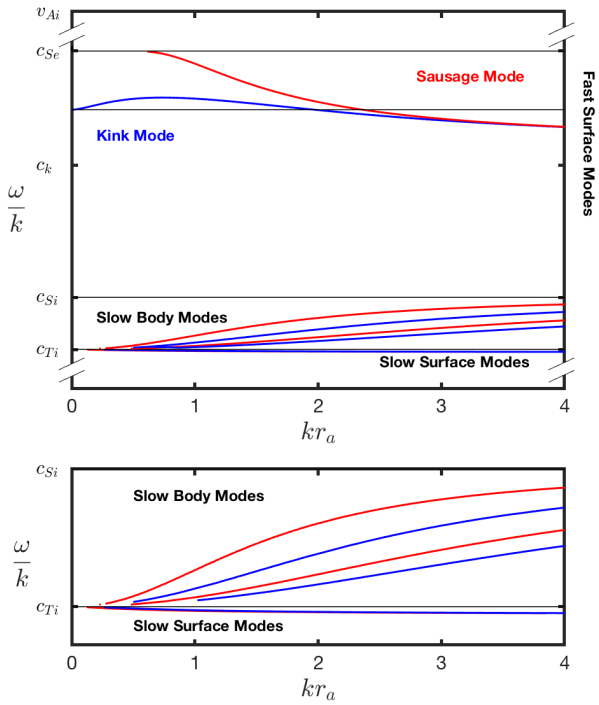

Figure 2.2: The phase speeds of modes under photospheric conditions were shown. The bottom panel shows a magnification of the section corresponding to the slow body and surface waves. The blue line represents kink modes while the red line represents sausage modes.

2.2.3 Photospheric tubes

The numerical algorithm described in Section 2.2.2 was applied to solve the dispersion relation equations governing wave propagation in a magnetic cylinder, as was done by Edwin and Roberts (1983). We have adapted this model to the actual physical plasma conditions. Under photospheric conditions, we

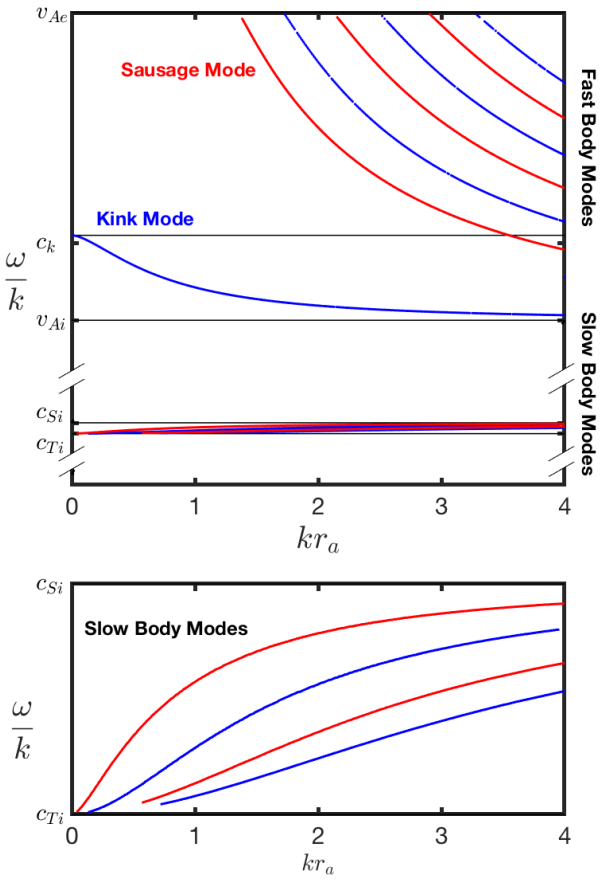

Figure 2.3: The phase speeds (ω/k) of modes under coronal conditions were shown. The bottom panel shows a magnification of the section corresponding to the slow body waves. The blue line represent kink modes and the red line represent sausage modes. kr_a is wavenumber.

assume that the background plasma temperature, density and pressure in umbra is less than the in the penumbra and the magnetic field strength is greater in the umbra than the penumbra (see, e.g. Maltby et al. 1986). This leads to the following relations between the characteristic plasma speeds: i.e., v_{Ai}, $c_{Se} > c_{Si}$, v_{Ae}. These particular conditions have important consequence for the types of MHD wave modes that can be supported by such a waveguide. Specifically, under these conditions, the MHD wave modes with the largest phase speeds, v_{ph}, in the z direction are surface modes with $v_{ph} \in (c_{Si}, c_{Se})$, with the largest amplitude oscillations at the umbra/penumbra boundary. In addition, we found that such of a waveguide can support the slow body modes and these have a slower phase speeds in the z direction with $v_{ph} \in (c_{Ti}, c_{Si})$ (see Figure 2.2).

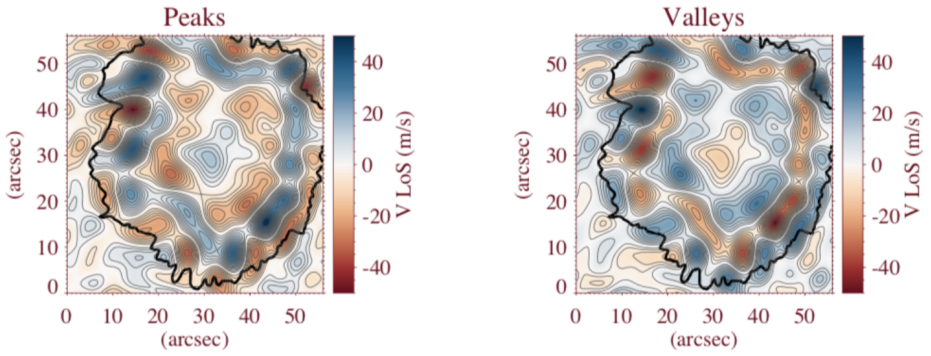

Figure 2.4: Instantaneous map of the filtered Doppler velocity, derived from the IBIS Fe I 6173 Å spectral imaging sequence. Courtesy of Dr Marco Stangalini.

2.2.4 Coronal loops

The solutions obtained by solving Equations (2.10) under coronal conditions: i.e., $c_{Se} < v_{Ai} < v_{Ae}$ are a slow body waves (kink and sausage) modes that have a phase speed between c_{Ti} and c_{Si} and fast body waves (kink and sausage) modes that have a phase speed between v_{Ai} and v_{Ae}. The sausage mode causes expansions and contractions of the plasma structure and kink mode illustrates the mode that causes the displacement of the axis of the plasma structure (see Figure 2.1). Figure 2.3 illustrates the behaviour of the sausage ($m = 0$) and kink ($m = 1$) body modes of oscillations. There are no surface modes under conditions expected in coronal conditions.

These results under photosperic and coronal conditions correspond well to the result found by Edwin and Roberts (1983). This is evidence of the effectiveness of the method used, which will be used later in finding solutions of the dispersion relation of the MHD waves propagate in the magnetic flux tubes with elliptical cross sectional shape in Chapter 3.

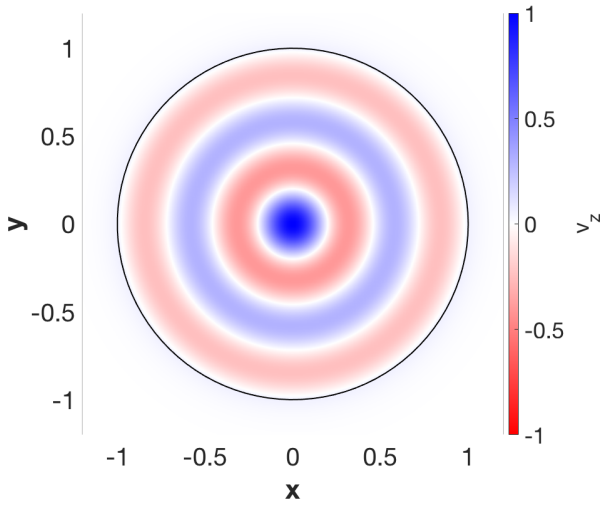

Figure 2.5: Sausage mode were plotted under coronal conditions, i.e. v_{Ae}, $v_{Ai} > c_{Si}$, c_{Se}.

2.3 Sausage mode

Here, the cylindrical model will be used to give an explanation of wave mode shown on Figure 2.4. In this model, the line of sight (LOS) magnetic (b_z) and velocity (v_z) perturbations are simply proportional to each other. The observed MHD wave mode is almost rotationally symmetric (apart from the small region at the top left of the umbra) with four nodes in the radial direction. Hence, the approximate rotational symmetry of the oscillatory motion is closest to the sausage wave mode in a cylindrical waveguide and the presence of radial nodes tells us that it is higher order radial harmonic. It is clearly seen that the observed modes have nodes in the radial direction (see Figure 2.4). As we mentioned, in previous Section the surface modes do not have nodes in the radial direction this does not match with what we observe. The only MHD wave modes which can have nodes in the radial direction are body modes and these have a slower phase speeds in the z direction with $v_{ph} \in (c_{Ti}, c_{Si})$. Under these conditions the sausage mode internal solution for the LOS velocity and magnetic perturbations is given by $v_z \propto b_z \propto J_0(|m_i|r_a)$, where J_0 is the zeroth order Bessel function of the first kind. Under the chosen sunspot conditions should be $m_i^2 < 0$ for the required body mode solution in Equation 2.10. To closely approximate the observed radial mode structure of the sausage mode shown in Figure 2.4. We see that the fourth radial node occurs in the neighbourhood of the umbra/penumbra boundary. The fourth zero of

$J_0(|m_i|r_a)$ occurs when $|m_i|r_a \approx 11.79$. Although we do not know the values of k_z, v_{ph} and the characteristic plasma speeds that define m_i this estimate helps us to constrain the solutions of the full dispersion relation derived in Section 2.1.3. The particular ratios used to numerically solve the dispersion relation are $v_{Ai} = 2c_{Si}, c_{Se} = 1.5c_0, v_{Ae} = 0.5c_{Si}$. Total pressure balance between the internal and external plasma demands that $\rho_e/\rho_i = (2c_{Si}^2 + \gamma v_{Ai}^2)/(2c_{Se}^2 + \gamma v_{Ae}^2)$. Taking $\gamma = 5/3$ for a neutral hydrogen gas gives $\rho_e/\rho_i = 1.76$. For the slow sausage body mode shown Figure 2.2 the chosen solution has $v_{ph} = 0.95$, $k_z = 16.69$ and $|m_i r_a| = 12.13$.

It appears that the mode obtained from numerical modeling in Figure 2.5 is almost similar to the mode observed in Figure 2.4, which gives an initial impression that this observed pattern is the sausage modes. However, we will make more sure whether this result really gives correct explanation of the observed mode. We will confirm whether the observed mode is actually sausage mode in Chapter 4.

CHAPTER 3

Solar atmospheric MHD wave modes in magnetic flux tubes of elliptical cross-sectional shape

The purpose of this Chapter is to present the result on study of the behaviour of magnetohydrodynamic (MHD) wave modes that propagate in compressible magnetic flux tubes with an elliptical cross-section, embedded in a magnetic environment. The dispersion relation, which describes the behaviour of MHD wave modes permitted in an elliptical magnetic flux tube, is solved numerically. Distortion of the spatial structure of the purely real eigenmodes from the well known circular flux tube model has been considered. The problem has been studied under both photospheric and coronal conditions. Our result show that (i) solutions in the form of even Mathieu functions are more sensitive to the value of eccentricity than solutions with the form of odd Mathieu functions; (ii) if ellipticity of the magnetic flux tube cross-section is increased, a sausage mode ($m = 0$) can not be easily identified; (iii) even solutions which correspond to the fluting mode ($m = 3$) can be misinterpreted as a kink mode ($m = 1$) due to their similarities. In contrast to the fluting modes which are polarised along the major axis and strongly depend on the ellipticity of the magnetic flux tube, the kink and sausage surface modes are practically unaffected by ellipticity. Several examples of the spacial structure of the eigenmodes permitted in the pores and sunspots have been visualised. The solutions obtained in approximation of cylindrical symmetry are in good agreement with previous studies.

3.1 Introduction

High-resolution ground and space-based observations of the solar atmosphere in combination with the theory of magnetohydrodynamic (MHD) wave propagation provides us with an opportunity to understand the behaviour of observed waves in more detail. Since the discovery by Alfvén (1942), which states that plasma supports wave-like variation in the magnetic field, much research

effort has been devoted to the study of MHD waves and oscillations in the solar atmosphere under a variety of plasma parameters and different magnetic structures. MHD wave propagation in unbounded homogeneous plasma was previously analysed by many researchers such as Lighthill (1960); Cowling (1976); Parker (2004); Goedbloed and Poedts (2004); Aschwanden (2005); Priest (2014).

MHD wave propagation in a bounded inhomogeneous plasma configuration has been extensively studied in the past. For example, (see, e.g. Verth, 2008; Fedun, 2008; Goossens et al., 2014; Jess et al., 2015). Verth (2008) investigated the effect of an inhomogeneous magnetic field on coronal loop oscillations. The effects caused by the presence of a magnetic twist in cylindrical flux tubes have been studied by Fedun (2008). Goossens et al. (2014) studied the kink wave in solar magnetic flux tubes and found that the velocity field is naturally a sum of both transverse and rotational motion. Jess et al. (2015) reviewed the characterization and interpretation of oscillations that appear in the solar chromosphere.

A variety of analytical models have been used to analyse wave propagation in the magnetic interface (Wentzel, 1979; Musielak et al., 2000; Huang et al., 2017; Roberts, 1981*a*; Ballai et al., 2011; Vickers et al., 2018), magnetic slab (Parker, 1974; Cram and Wilson, 1975; Roberts, 1981*b*; Hornsey et al., 2014; Pascoe and Nakariakov, 2016; Mather et al., 2018). Magnetic cylinders with a vertical magnetic field have been studied by Edwin and Roberts (1983); Erdélyi and Fedun (2007); Verth (2007); Jess et al. (2015) and for the case of a twisted magnetic field, by Ruderman et al. (2014); Giagkiozis et al. (2016); Williams et al. (2016); Fedun et al. (2017). In particular, Wentzel (1979) investigated the effect of compressibility on the propagation of surface waves at a single interface and derived an expression for the energy carried by such waves. The author has obtained the dispersion relation for the isothermal plasma disturbances without analysis of solutions. Later, Roberts (1981*a*) provided a more general study of MHD wave behaviour at the magnetic interface and analysed propagation of slow surface waves when one side of the interface is magnetically free. It was shown that "trapped" surface waves have the general property that their wave amplitude and, therefore, energy decreases with distance from the magnetic interface. Ballai et al. (2011) investigated the nature of globally propagating waves at the spherical interface under solar corona conditions and has shown that the frequency of waves is increased as the density of plasma decreases at the interface.

In relation to MHD wave propagation in slab geometry, Parker (1974) has described the occurrence of surface waves in the isolated slab for the incompressible plasma approximation. Cram and Wilson (1975) studied wave propagation in a compressible slab. The authors have shown that fast MHD waves are not free modes of the slab. Roberts (1981*b*) obtained the dispersion relation governing MHD wave propagation in an isolated magnetic slab and specified two main magneto-acoustic modes; the sausage and the kink waves. These have various sub-categories e.g. slow/fast body and surface waves. The fast magneto-acoustic wave propagates only if the magnetic slab temperature is less than or equal to the temperature of the field-free environment. Furthermore, Roberts (1981*b*) investigated wave propagation in a slender slab and found that the kink mode may exist in this regime as well, i.e. when the width of the waveguide is much less than the longitudinal wavelength. Interestingly, under these conditions, the sausage mode can be either a body or surface wave with a phase speed that is close to the tube speed.

Edwin and Roberts (1983) proposed a simple but instructive model for the analysis of MHD wave propagation in magnetic flux tubes which is based on cylindrical geometry. In spite of the complexity of realistic magnetic configurations, many previous studies were focused on studying the behaviour of waves in the magnetic cylinder under different conditions because of the simplicity of the model. For example, Erdélyi and Fedun (2007) analysed the effect of compressible magnetically twisted flux tubes on MHD sausage waves. The authors have found that the period of sausage mode oscillations depends on the magnetic twist. More studies in categorizing and interpreting wave propagation in the solar chromosphere were reviewed by Jess et al. (2015). Verth (2007) showed that the frequency and amplitude of the standing fast kink mode can provide us with information regarding the density and magnetic structure of coronal loops.

Ruderman (2003) studied the resonant damping of oscillations of coronal loops with elliptic cross-sections under the assumption of zero plasma-β. Erdélyi and Morton (2009) studied wave propagation in a compressible magnetic flux tube with an elliptical cross-section when finite plasma-β is considered. It was found that the thin flux tube approximation supports the propagation of slow sausage and the fast body mode. Under coronal conditions, the slow and fast body waves for both kink and sausage modes were present, while under photospheric conditions the slow body waves and fast surface waves for kink and sausage modes were present.

Despite the fact that the high-resolution ground-based observations show a great variety of sunspots, a number of studies were devoted to the analysis of the plasma behaviour in a magnetic waveguide with an elliptical cross-section. For instance, Liu et al. (2016) studied the flare-induced rotation of a sunspot with an elliptical shape. There is observational evidence of elliptic pores shown by Keys et al. (2018).

It is well known that the sunspots and pores do not have an ideal circular cross-sectional shape, (see Figure 3.1, for example). As a result, any imbalance in the diameter of the waveguide requires the use of an elliptical coordinate system instead of a cylindrical one. In this Chapter, we attempt to analyse the MHD modes permitted in the elliptical magnetic flux tubes. The corresponding dispersion relation has been solved numerically under both photospheric and coronal conditions.

This Chapter is tailored to identifying wave modes in pores and sunspots that can be closely approximated with elliptical cross-sections. From observational data (see e.g. Jess et al., 2017; Kang et al., 2019; Albidah et al., 2021) we are restricted to an analysis of the spatial structure of the oscillations inside the umbral regions of pores and sunspots only. The oscillatory signal decays too rapidly outside of these regions to analyse with any certainty. Hence, this indicates that we are observing slow mode type wave modes (which do not strongly perturb the boundary). From a modelling point of view, the difference in external/internal values of magnetic field strength and density only affects the decay rate length scale of the oscillation outside of the waveguide. The internal spatial structure of the mode is largely unaffected and is not of primary interest for the purposes of our study.

This Chapter is structured as follows. In Section (3.2), we derive the general dispersion relation which describes the linear magneto-acoustic waves in a compressible magnetic flux tube with an elliptical cross-section. In Section (3.3) and (3.4) the numerical solutions of this relation obtained under coronal and photospheric conditions are analysed. In Section (3.5), the MHD wave modes under coronal and photospheric conditions are investigated. In Section (3.6) we conclude our results.

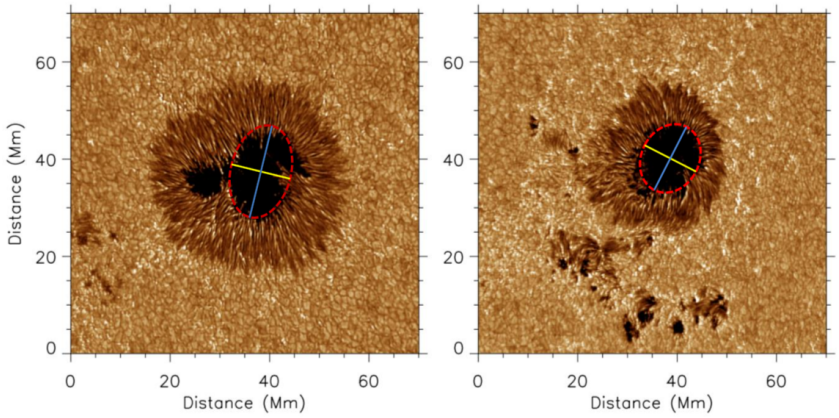

Figure 3.1: Two active regions, NOAA AR12565 (left) and NOAA AR12149 (right), captured in the G-band by the Rapid Oscillations in the Solar Atmosphere (see, e.g. Jess et al., 2010) instrument at the Dunn Solar Telescope. Each panel shows a non-circularly symmetric sunspot structure, highlighting the existence of elliptical magnetic field concentrations in the solar atmosphere. The eccentricity of the elliptical shape of the left image is 0.76, while in the right image the eccentricity is 0.58.

3.2 General dispersion relation

Let us consider a straight magnetic flux tube ($\mathbf{B}_{0i} = B_{0i}\ \mathbf{z}$) with an elliptical cross-section embedded in a uniform external magnetic field ($\mathbf{B}_{0e} = B_{0e}\ \mathbf{z}$), where $\mathbf{z}$ is the unit vector parallel to the flux tube axis. The index "0" corresponds to the unperturbed equilibrium state; all dependent variables inside the flux tube have index "i", while quantities outside the tube are denoted with index "e". The cross-section of the flux tube, perpendicular to its axis, is most conveniently described by the elliptic coordinate system (s, ϕ) shown in Figure 3.2. The flux tube boundary is defined by the confocal ellipse s_0 (see blue line in Figure 3.2).

The well-known equation governing small-amplitude MHD waves, obtained by linearizing the ideal MHD equations (see, e.g. Lighthill, 1960; Cowling, 1976; Roberts, 1981*a*; Aschwanden, 2005), is

$$\frac{\partial^4 \Delta}{\partial t^4} - (c_S^2 + v_A^2)\frac{\partial^2}{\partial t^2}\nabla^2\Delta + c_S^2 v_A^2 \frac{\partial^2}{\partial z^2}\nabla^2\Delta = 0, \tag{3.1}$$

where

$$\Delta = \nabla \cdot \mathbf{v}, \quad v_A = \frac{B_0}{\sqrt{\mu_0 \rho_0}}, \quad c_S = \sqrt{\gamma \frac{p_0}{\rho_0}}.$$

Here, Δ is the divergence of velocity perturbation $\mathbf{v}$, v_A is the Alfvén speed, c_S is the sound speed, μ_0 is the magnetic permeability, γ is the ratio of specific heats, p_0 is the unperturbed kinetic plasma pressure and ρ_0 is the plasma

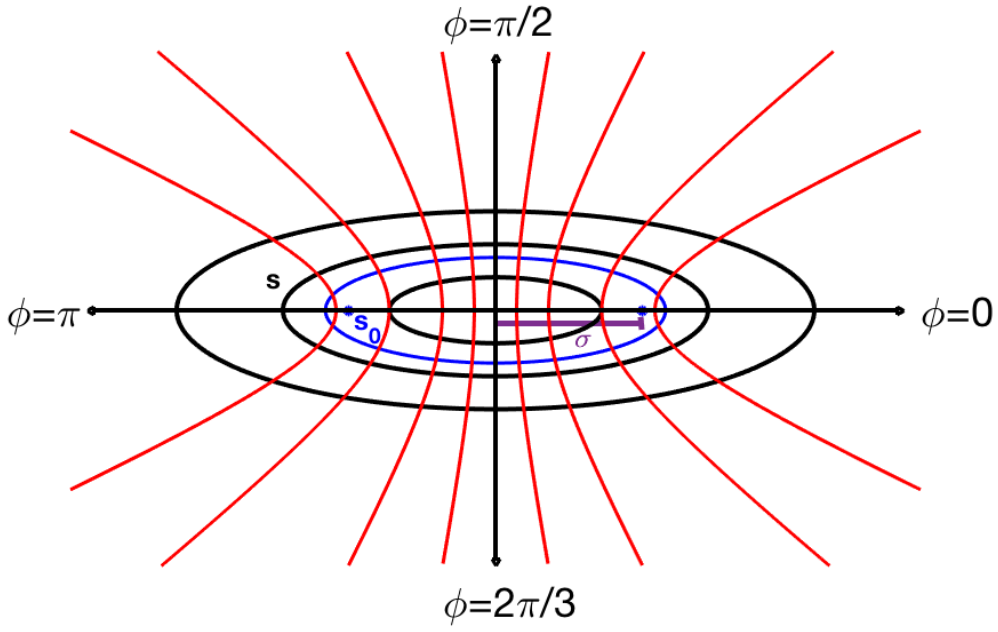

Figure 3.2: A sketch of the elliptic coordinate system in the x, y plane which is perpendicular to the magnetic flux tube axis. The elliptic coordinates are $(s,\ \phi)$, where s is a non-negative real number and $\phi \in [0, 2\pi]$. The confocal ellipses are shown as contours of the constant values of s and the orthogonal hyperbolas correspond to the constant ϕ contours. The blue confocal ellipse s_0 shows the boundary of the magnetic flux tube. The distance between the centre of the ellipse and the focal points is σ.

unperturbed density. In the elliptic cylindrical coordinate system $(s,\ \phi,\ z)$ the Laplacian operator can be represented as:

$$\nabla^2 = H^{-2}\left(\frac{\partial^2}{\partial s^2} + \frac{\partial^2}{\partial \phi^2}\right) + \frac{\partial^2}{\partial z^2}, \tag{3.2}$$

where

$$H^2 = \sigma^2\left(\sinh^2(s) + \sin^2(\phi)\right), \tag{3.3}$$

is a scale factor and σ is the distance between the centre of the ellipse and its focal points (see Figure 3.2). The connection to the Cartesian coordinate system are given by,

$$x = \sigma\cosh(s)\cos(\phi), \qquad y = \sigma\sinh(s)\sin(\phi),$$

where the x-axis is directed along the major axis of the ellipse and the y-axis is directed along its minor axis.

By applying Fourier decomposition and separation of variables the solution of Equation (3.1) can be represented as:

$$\Delta = S(s)\Phi(\phi)\exp(i(kz - \omega t)), \tag{3.4}$$

where k is the wavenumber in z direction, ω is the angular frequency and the functions $S(s)$ and $\Phi(\phi)$ are to be determined. By substituting Equation (3.4) in Equation (3.1) the perturbed components of velocity $\mathbf{v}$, magnetic field $\mathbf{b}$, pressure p and total pressure p_T, i.e the sum of kinetic and magnetic plasma pressures, in the elliptic coordinate system can be derived explicitly as (see e.g. Erdélyi and Morton, 2009):

$$v_s(s,\,\phi) = -\left(\frac{\omega^2 - k^2 c_S^2}{H\omega^2 m_0^2}\right)\frac{\partial S(s)}{\partial s}\Phi(\phi),$$

$$v_\phi(s,\,\phi) = -\left(\frac{\omega^2 - k^2 c_S^2}{H\omega^2 m_0^2}\right)S(s)\frac{\partial \Phi(\phi)}{\partial \phi},$$

$$v_z(s,\,\phi) = -\left(\frac{ikc_S^2}{\omega^2}\right)S(s)\Phi(\phi),$$

$$b_s(s,\,\phi) = B_0\frac{k}{\omega}v_s(s,\,\phi),$$

$$b_\phi(s,\,\phi) = -B_0\frac{k}{\omega}v_\phi(s,\,\phi),$$

$$b_z(s,\,\phi) = -iB_0\frac{\omega^2 - k^2c_S^2}{\omega^3}S(s)\Phi(\phi),$$

$$p(s,\,\phi) = -i\rho_0\frac{c_S^2}{\omega}S(s)\Phi(\phi),$$

$$p_T(s,\,\phi) = -\frac{i\rho_0}{\omega^3}(c_S^2 + v_A^2)(\omega^2 - k^2c_T^2)S(s)\Phi(\phi),$$

$$\rho(s,\,\phi) = -\frac{i\rho_0}{\omega}S(s)\Phi(\phi).$$

Here, v_s, v_ϕ and v_z are the perturbed velocity components in the s, ϕ and z directions, respectively; b_s, b_ϕ and b_z are the perturbed magnetic field components; ρ is the plasma density perturbation. It is clear that the density perturbation is proportional to other MHD variables. Note that all other components are proportional to the same functions.

Next let us represent Equation (3.1) in elliptic cylindrical coordinates. By substituting ∇^2 from Equation (3.2) and Δ from Equation (3.4) into Equation (3.1) we obtain

$$H^{-2}\left(\frac{1}{S}\frac{\partial^2 S}{\partial s^2}+\frac{1}{\Phi}\frac{\partial^2 \Phi}{\partial \phi^2}\right)+\frac{4}{\sigma^2}m_0^2=0, \tag{3.5}$$

where

$$m_0^2=\frac{\sigma^2}{4}\frac{(\omega^2-k^2c_S^2)(\omega^2-k^2v_A^2)}{(c_S^2+v_A^2)(\omega^2-k^2c_T^2)}. \tag{3.6}$$

and

$$c_{Ti}^2 \;=\; \frac{c_S^2 v_A^2}{c_S^2+v_A^2} \tag{3.7}$$

is the tube speed. By using the scale factor given by Equation (3.3), Equation (3.5) can be rewritten as

$$\frac{1}{S}\frac{\partial^2 S}{\partial s^2}+4m_0^2\sinh^2(s)=-\left(\frac{1}{\Phi}\frac{\partial^2 \Phi}{\partial \phi^2}+4m_0^2\sin^2(\phi)\right). \tag{3.8}$$

By introducing the separation constant h, Equation (3.8) can be reduced to two ordinary differential equations, where h is the constant to be determined (see appendix A).

$$\frac{d^2\Phi}{d\phi^2}+(h-2m_0^2\cos(2\phi))\Phi=0 \tag{3.9}$$

and

$$\frac{d^2 S}{ds^2}-(h-2m_0^2\cosh(2s))S=0. \tag{3.10}$$

The Equation (3.9) and Equation (3.10) represent the Mathieu equation and modified Mathieu equation in case of h and m_0 being real and $m_0^2>0$ (see e.g., Mathieu, 1868; Abramowitz and Stegun, 1964).

The quantity m_0^2 under elliptical coordinates has an opposite sign of m_0^2 under cylindrical coordinates. Note that $\frac{4}{\sigma^2}m_0^2$ in elliptical coordinates is equal to $-m_0^2$ in cylindrical coordinates (see e.g. Edwin and Roberts, 1983; Spruit, 1982*a*).

In order to obtain the periodic solution of the Mathieu equation, the particular value of m_0^2 should be suitably related to the parameter h which has an infinite set of distinct values (see appendix A for more detail). The Mathieu equations have odd solutions with respect to the minor axis denoted by

Table 3.1: The permitted combination of the indexes of the radial Mathieu function with respect to the major (even solution), $C_m(s,\, m_0^2)$ and minor (odd solution), $S_m(s,\, m_0^2)$ axes. Here, $m = 2n + j$ is the order of Mathieu function and $j = 0$ corresponds to the even order of the Mathieu function. For the odd Mathieu function of even order, n starts from 1 and, therefore, the case $m = 0$ for S_{2n} can not be realized.

m	C_{2n}	S_{2n}
0	$n = 0$	n/a
2	$n = 1$	$n = 1$
4	$n = 2$	$n = 2$
6	$n = 3$	$n = 3$
:	:	:

Table 3.2: The permitted combination of the radial Mathieu function indexes with respect to the major (even solution), $C_m(s,\, m_0^2)$ and minor (odd solution), $S_m(s,\, m_0^2)$ axes. Again, the quantity $m = 2n + j$ is the order of Mathieu function and $j = 1$ corresponds to the odd order of the Mathieu function.

m	C_{2n+1}	S_{2n+1}
1	$n = 0$	$n = 0$
3	$n = 1$	$n = 1$
5	$n = 2$	$n = 2$
7	$n = 3$	$n = 3$
:	:	:

$S_{2n+j}(s,\, m_0^2)$ for radial Mathieu functions and $s_{2n+j}(\phi,\, m_0^2)$ for angular Mathieu functions. The even solutions with respect to the major axis are denoted by $C_{2n+j}(s,\, m_0^2)$ for radial Mathieu functions and $c_{2n+j}(\phi,\, m_0^2)$ for angular Mathieu functions(see, e.g. McLachlan, 1947), where $n \in \mathbb{N}$ and $j = 0, 1$ (see the Table 3.1 and 3.2 for more details).

The modulus of m_0 in the Mathieu functions argument plays a crucial role in determining how much the confocal ellipse node is of the modes. There is an infinite set of possible values of m_0 that satisfy the boundary conditions. On the other side, even and odd Mathieu functions have an even and odd order which correspond to the different hyperbola nodes.

In elliptic coordinates, the modified Mathieu function given by Equation (3.10) is the solution of the radial Mathieu equation, and corresponds to the Bessel equation in polar coordinates. When $m_0^2 > 0$, the solutions of Equation (3.10) are oscillatory radial Mathieu functions which can be represented as a series of Bessel functions of first kind (J_m) (see Appendix B). This case provides the internal part of the solutions for body modes (Section 3.2.1).

When $m_0^2 < 0$, Equation (3.10) becomes

$$\frac{d^2S}{ds^2} - (h + 2m_0^2\cosh(2s))S = 0 \tag{3.11}$$

and the solutions are non-oscillatory radial Mathieu functions which can be represented as a series of modified Bessel functions of the first kind (I_m) (see appendix C). These provide the internal part of the solutions for surface modes (see Section 3.2.1). There are also evanescent modified Mathieu functions of the third kind which can be written as a series of modified Bessel functions of the second kind (K_m) and the first kind (I_m), when $m_e^2 < 0$ (see Appendix D). These functions correspond to the external part of the solutions for both body and surface modes (see Section 3.2.2).

3.2.1 The general solution inside the magnetic flux tube

The even and odd solutions of Equations (3.10) and (3.11), confined within the flux tube boundary confocal ellipse s_0 ($s < s_0$), are

$$\Delta_i = S(s)\Phi(\phi) = \begin{cases} A_0 C_{2n+j}(s,\, m_{0i}^2) c_{2n+j}(\phi,\, m_{0i}^2) & \text{even}, \\ B_0 S_{2n+j}(s,\, m_{0i}^2) s_{2n+j}(\phi,\, m_{0i}^2) & \text{odd}. \end{cases}, \tag{3.12}$$

Here, A_0 and B_0 are arbitrary constants and

$$m_{0i}^2 = \frac{\sigma^2}{4}\frac{(\omega^2 - k^2c_{Si}^2)(\omega^2 - k^2v_{Ai}^2)}{(c_{Si}^2 + v_{Ai}^2)(\omega^2 - k^2c_{Ti}^2)}.$$

Let us introduce the Θ_m^E and Θ_m^O notations for the internal body mode solutions where the superscripts E and O denote the even and odd solutions, respectively. The subscript m relates the elliptical to the cylindrical wave modes, i.e., sausage ($m = 0$), kink ($m = 1$) and fluting ($m \geq 2$), see Table 3.1 and 3.2 for more details.

When $m_{0i}^2 > 0$ the internal even and odd body mode solutions are:

$$\Theta_m^E(m_{0i}, s) = C_{2n+j}(s,\, m_{0i}^2), \tag{3.13}$$

$$\Theta_m^O(m_{0i}, s) = S_{2n+j}(s,\, m_{0i}^2). \tag{3.14}$$

We introduce Ξ_m^E and Ξ_m^O notations for the even and odd internal surface mode solutions, respectively.

When $m_{0i}^2 < 0$ the internal surface mode solutions are:

$$\Xi_m^E(|m_{0i}|, s) = C_{2n+j}(s,\, m_{0i}^2), \tag{3.15}$$

$$\Xi_m^O(|m_{0i}|, s) = S_{2n+j}(s,\, m_{0i}^2). \tag{3.16}$$

The functions Θ and Ξ used here can be represented in the form of series of the bessel functions J_m and I_m (see appendices B, C and D). The representation of obtained solutions in the Bessel functions form is more convenient for numerical calculations.

3.2.2 The general solution outside the magnetic flux tube

For $m_{0e}^2 < 0$ in the external region ($s > s_0$) the amplitude of the non-oscillatory perturbations decays with distance from the magnetic flux tube and, therefore:

$$\Delta_e = S(s)\Phi(\phi) = \begin{cases} A_e FeK_{2n+j}(s,\, m_{0e}^2)c_{2n+j}(\phi,\, m_{0e}^2) & \text{even}, \\ B_e GeK_{2n+j}(s,\, m_{0e}^2)s_{2n+j}(\phi,\, m_{0e}^2) & \text{odd}. \end{cases}, \tag{3.17}$$

Here,

$$m_{0e}^2 = \frac{\sigma^2}{4}\frac{(\omega^2 - k^2 c_{Se}^2)(\omega^2 - k^2 v_{Ae}^2)}{(c_{Se}^2 + v_{Ae}^2)(\omega^2 - k^2 c_{Te}^2)},$$

and A_e and B_e are the arbitrary constants and $FeK_{2n+j}(s,\, m_{0e}^2)$ and $GeK_{2n+j}(s,\, m_{0e}^2)$ are the modified Mathieu functions of the third kind. Let us introduce the notations for the even and odd external evanescent solutions as Ψ_m^E and Ψ_m^O, respectively, so

$$\Psi_m^E(|m_{0e}|, s) = FeK_{2n+j}(s,\, m_{0e}^2),$$
$$\Psi_m^O(|m_{0e}|, s) = GeK_{2n+j}(s,\, m_{0e}^2).$$

3.2.3 The general dispersion relation

To obtain the equilibrium and the general dispersion relation, the background pressure balance has to be satisfied, i.e.:

$$p_{0i} + \frac{B_{0i}^2}{2\mu_0} = p_{0e} + \frac{B_{0e}^2}{2\mu_0}. \tag{3.18}$$

Here, p_{0i} and p_{0e} are the plasma pressures inside and outside of the magnetic flux tube, B_{0i} and B_{0e} are the magnetic fields in corresponding regions.

By taking into account the continuity of the velocity v_s and total plasma pressure (p_T) across the boundary of magnetic flux tube $s = s_0$ (see e.g. Equation (3.18)), the dispersion relations for body modes ($m_{0i}^2 > 0$) can be written as:

$$\frac{v_{ph}^2 - c_{Si}^2}{m_{0i}^2 v_{ph}^2} M_{0e} \frac{\Theta_m'^{E,O}(m_{0i}, s_0)}{\Theta_m^{E,O}(m_{0i}, s_0)} = \frac{v_{ph}^2 - c_{Se}^2}{m_{0e}^2 v_{ph}^2} M_{0i} \frac{\Psi_m'^{E,O}(|m_{0e}|, s_0)}{\Psi_m^{E,O}(|m_{0e}|, s_0)} \tag{3.19}$$

Table 3.3: The symmetrical properties of the Mathieu functions.

Mathieu functions	Order	Major axis	Minor axis
even	even	symmetrical	symmetrical
even	odd	symmetrical	asymmetrical
odd	even	asymmetrical	asymmetrical
odd	odd	asymmetrical	symmetrical

Similarly the dispersion relation for surface modes ($m_{0i}^2 < 0$) is given by

$$\frac{v_{ph}^2 - c_{Si}^2}{m_{0i}^2 v_{ph}^2} M_{0e} \frac{\Xi_m'^{E,O}(|m_{0i}|, s_0)}{\Xi_m^{E,O}(|m_{0i}|, s_0)} = \frac{v_{ph}^2 - c_{Se}^2}{m_{0e}^2 v_{ph}^2} M_{0i} \frac{\Psi_m'^{E,O}(|m_{0e}|, s_0)}{\Psi_m^{E,O}(|m_{0e}|, s_0)}. \tag{3.20}$$

Here, $v_{ph} = \frac{\omega}{k}$ is the phase speed, and

$$M_{0i} = \rho_{0i}(c_{Si}^2 + v_{Ai}^2)(c_{Ti}^2 - v_{ph}^2),$$
$$M_{0e} = \rho_{0e}(c_{Se}^2 + v_{Ae}^2)(c_{Te}^2 - v_{ph}^2).$$

The prime in Equations (3.19)-(3.20) denotes the derivative of the Mathieu function in respect to the confocal ellipse curve s.

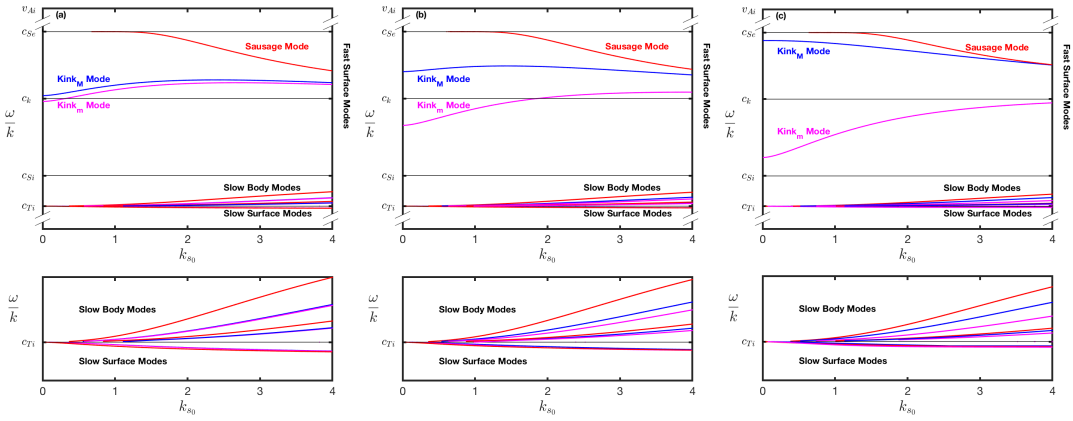

Figure 3.3: The phase speed (ω/k) of slow body and surface modes and fast surface modes are shown under photospheric conditions. The panels a), b) and c) correspond to the different values of eccentricity of the magnetic flux tube cross-section, i.e. $\epsilon = 0.24$ ($s_0 = 2.1$), $\epsilon = 0.65$ ($s_0 = 0.99$) and $\epsilon = 0.84$ ($s_0 = 0.60$). The bottom panels show the zoom of corresponding regions from the panels above. The blue curves on all plots show the kink modes polarised along major axis of elliptical cross-section of the magnetic flux tube (indicated as capital M as an index), magenta curves represent the kink modes polarised along minor axis (indicated as m as an index) and the red curves represent the sausage modes.

3.3 Coronal conditions

To model coronal conditions, we assume that the internal plasma temperature, density and pressure are greater than at the external region and internal magnetic field strength is less than external. These correspond to the following relations between the characteristic plasma speeds: $v_{Ae}, v_{Ai} > c_{Si}, c_{Se}$. The chosen conditions are required for slow and fast body waves to occur. Therefore, if we choose $v_{Ai} > v_{Ae}$, fast body waves are absent and only two of the infinitely many slow body waves are shown (Edwin and Roberts, 1983). The wave solutions must satisfy the physical conditions, whereby the oscillations are mainly confined to the ellipse region and they decay outside of the boundary of the magnetic flux tube. Therefore, m_{0e}^2 should be negative in order to satisfy the evanescent solutions in the external region and m_{0i}^2 should be positive in order to satisfy the oscillation solutions in the internal region. For numerical calculations the following values of the characteristic speeds have been used: $v_{Ae} = 5c_{Si}$, $c_{Se} = 0.5c_{Si}$ and $v_{Ai} = 2c_{Si}$. In particular, v_{ph} is the normalised phase speed by internal sound speed $c_{Si} = 1$ and $k_{s0} = ke^{s_0}\sigma/2$ is dimensionless wavenumber k normalised by $e^{s_0}\sigma/2$. This term, i.e. $e^{s_0}\sigma/2 \to a$ if $b = a$ (i.e. elliptical cross section circular cross section). In more details, the distance between major axis a and minor axis b are connected with s_0 (where s_0 is the confocal elliptic cylinders centered on the origin) and $\sigma = \sqrt{a^2 - b^2}$. Therefore, the limit of $s_0 \to \infty$ corresponds to a tube with circular cross section and in the opposite, when $s_0 \to 0$, the tube cross-section is shrunk into the interval $[-\sigma, \sigma]$ of the x-axis, where σ is a quantity with the dimension of length.

For this set of chosen parameters the total pressure balance between the internal and external plasma requires $\frac{\rho_e}{\rho_0} = 0.21$. The numerical algorithm described in Section 2.2.2 was applied to solve Equations (3.19) and (3.20). The set of solutions were obtained: (i) the slow kink and sausage body modes that have a phase speed ranging between internal tube speed, c_{Ti}, and internal sound speed, c_{Si}, (ii) fast kink and sausage body modes with a phase speed ranging between internal Alfvén speed, v_{Ai}, and external Alfvén speed, v_{Ae}, (see Figure 3.3). It was also found that eccentricity defined as

$$\epsilon = \frac{1}{\cosh(s_0)} \tag{3.21}$$

has strong effect on the behaviour of solution. In particular, as the ellipticity of the cross-section increased, the difference in the phase speeds of the two kink

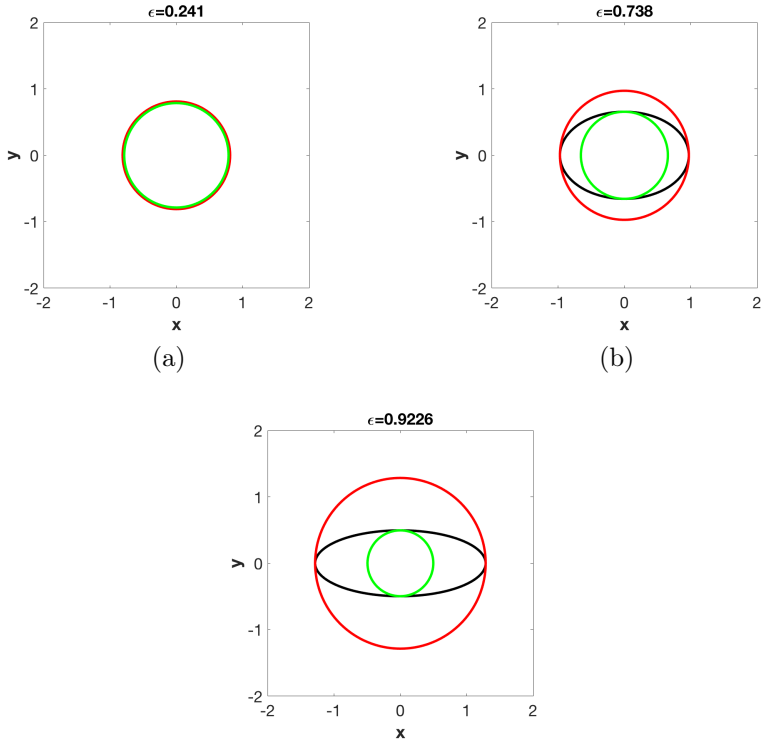

(a) (b) (c)

Figure 3.4: The diagrams compare the circle size with an ellipse. This diagram shows how the frequency of wave polarised in vertical and horizontal directions of elliptical shape can be compared with the frequency of wave polarised in a circular shape. The ellipse represented by the black color, and the red and green color represent the circle used to approximate the ellipse arcs in vertical and horizontal directions with the circle. Panel (a) shows the case when the ellipse is almost equal to the circle, panel (b) shows the case when the eccentricity of the ellipse is moderate, and panel (c) shows the situation when the eccentricity of the ellipse is very high.

modes which are polarised along the major axis and the minor axis is also increased. If ellipticity decreased, i.e. in the approximation of a circular shape, the difference in the phase speeds of the two kink modes is also decreased. It is clear from Figure 3.3 that in panels (a,d) when ($\epsilon = 0.24$), the solution polarised along major axis and minor axis is almost identical, while the differences between the phase speed increased in panels (b,e) when ($\epsilon = 0.65$) and (c,f) when ($\epsilon = 0.84$), as ellipiticiy is increased. We found that the fast body waves (the kink modes) polarised along minor axis has higher phase speed that those polarised along the major axis. As the ellipticity of the tube increases, the major axis stretches while the minor axis is contracted. This, in turn, allows the waves polarised the minor axis to have a higher phase speed as it

has more space than the wave polarised along major axis. The contrast, for slow waves, as we can see in panels (d,e and f) of Figures 3.3, the situation is completely opposite, so the waves that are polarised on the minor axis have smaller frequency than those polarised along the major axis, and the reason is because the slow magneto-acoustic waves are polarised mainly longitudinally, along the field lines, this make it less affected by the change in shape of the cross-section.

3.4 Photospheric conditions

Adapting this model to consider realistic physical plasma conditions of a sunspot under photospheric conditions, we assume that the internal plasma temperature, density and pressure are smaller than the external values of their corresponding parameters, and internal magnetic field strength is greater than its external value. This leads to the following relations between the characteristic plasma speeds: $v_{Ai}, c_{Se} > c_{Si}, v_{Ae}$. These conditions are needed for surface waves to occur. For example, if the internal plasma is cooler than the external plasma these conditions allow a fast surface wave to propagate with a phase speed c_{Se}. If the internal magnetic field strength is greater than external value these conditions will allow a slow surface mode with phase speed equal to c_{Ti}. For the numerical calculations we used the following ratios: $v_{Ae} = 0.5c_{Si}$, $c_{Se} = 1.5c_{Si}$ and $v_{Ai} = 2c_{Si}$. The total pressure balance between the internal and external plasma requires $\frac{\rho_e}{\rho_0} = 1.76$. Since for slow body mode $m_{0i}^2 > 0$ and $m_{0e}^2 < 0$, the dispersion Equation (3.19) was used. The case $m_{0i}^2 < 0$ and $m_{0e}^2 < 0$ correspond to the slow and fast surface mode and, therefore, the dispersion equation (3.20) is applicable for the surface wave. Under photospheric conditions we obtained: (i) slow kink and sausage surface modes, and slow kink and sausage body modes that have phase speeds between c_{Ti} and c_{Si}, (ii) fast kink and sausage surface modes which have the phase speed between the kink speed $c_k = \sqrt{(\rho_i v_{Ai}^2 + \rho_e v_{Ae}^2)/(\rho_i + \rho_e)}$ and c_{Se} (see Figure 3.5). The effect of ellipticity on solutions under photospheric conditions is similar to its effect on solutions under coronal conditions, as we see in the Figure 3.5, so the more the ellipticity, the greater the difference between the phase speed in between the polarised waves on both the minor and the major axis, but it is worth noting here that the phase speed of the fast surface waves polarised along the minor axis is less than the phase speed of the waves along the major axis, that is, here the condition is completely opposite to the phase speed of fast body

waves under coronal conditions. Perhaps the reason is that the surface waves have a maximum amplitudes at the boundary, which means that the directed frequency of wave polarised in the direction of the minor axis is equal to the frequency of a circular cross section of the same arc size in the direction of the minor axis, and the frequency of the polarised wave on the major axis is equal to the frequency of a wave in the size of a circular cross section equal to the arc in that direction (see Figure 3.4).

Our results show perfect agreement with the results obtained previously by Erdélyi and Morton (2009). In the following sections we discuss the obtained mode patterns and the effect of ellipticity on MHD modes in more details.

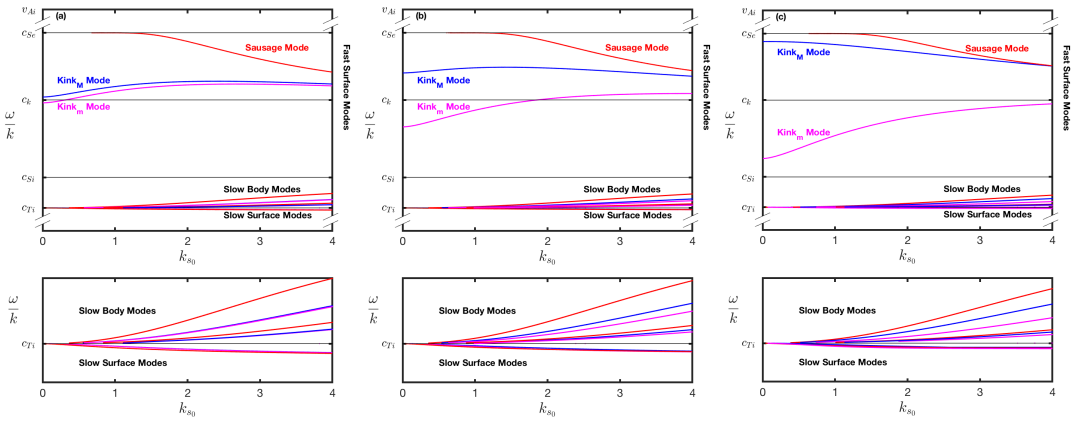

Figure 3.5: The phase speed (ω/k) of slow body and surface modes and fast surface modes are shown under photospheric conditions. The panels a), b) and c) correspond to the different values of eccentricity of the magnetic flux tube cross-section, i.e. $\epsilon = 0.24$ ($s_0 = 2.1$), $\epsilon = 0.65$ ($s_0 = 0.99$) and $\epsilon = 0.84$ ($s_0 = 0.60$). The bottom panels show the zoom of corresponding regions from the panels above. The blue curves on all plots show the kink modes polarised along major axis of elliptical cross-section of the magnetic flux tube (indicated as capital M as an index), magenta curves represent the kink modes polarised along minor axis (indicated as m as an index) and the red curves represent the sausage modes.

3.5 MHD wave modes under coronal and photospheric conditions

3.5.1 Coronal conditions

In the next section the main attention is paid to the fast and slow body modes since there are no surface modes under coronal conditions.

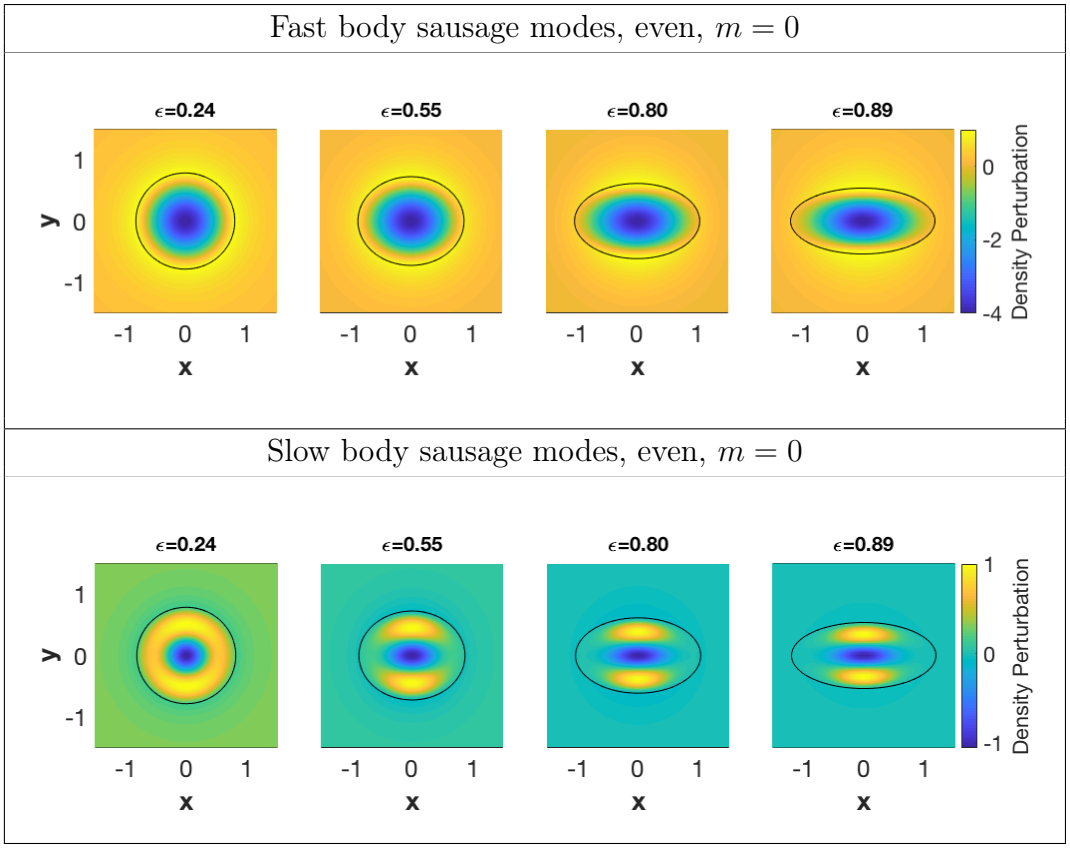

Figure 3.6: The normalised density perturbation calculated under coronal conditions i.e., v_{Ae}, $v_{Ai} > c_{Si}$, c_{Se} for different values of eccentricity. The upper panel shows the fast branch of the sausage mode which has no hyperbola node and no ellipse node. The lower panel shows the slow branch of sausage mode which has no hyperbola node and one ellipse node, i.e., even solution of the Mathieu equation. $m = 0$ represents the order of the Bessel function. For numerical calculations we used the fixed normalised value of the elliptical sunspot area to keep the smooth transition from circle to ellipse and to be able to explore the wave modes modification, the corresponding videos are currently available at: http://pdg.group.shef.ac.uk/Visualisations.html.

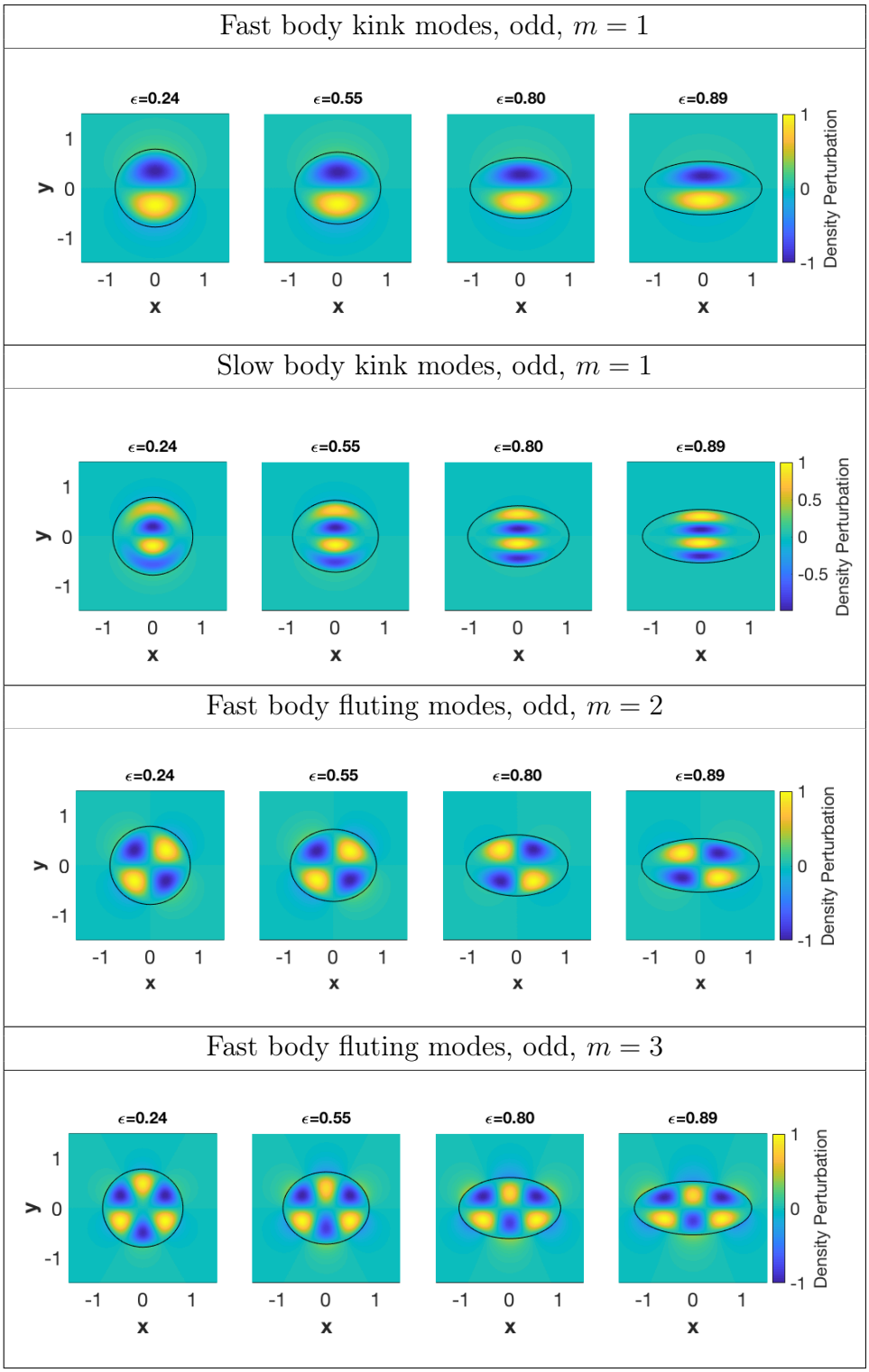

Figure 3.7: The normalised density perturbations under solar corona conditions (i.e., $v_{Ae}, v_{Ai} > c_{Si}, c_{Se}$) for the different values of eccentricity. From the top to bottom we show: the fast branch of the kink mode which has one hyperbola node and one ellipse node; the fast branch of the kink mode which has one hyperbola node and two ellipse nodes; the fast branch of the fluting ($m = 2$) mode which has two hyperbola nodes and one ellipse node; the fast branch of the fluting ($m = 3$) mode which has three hyperbola nodes and one ellipse node. (i.e., odd solution of Mathieu equation).

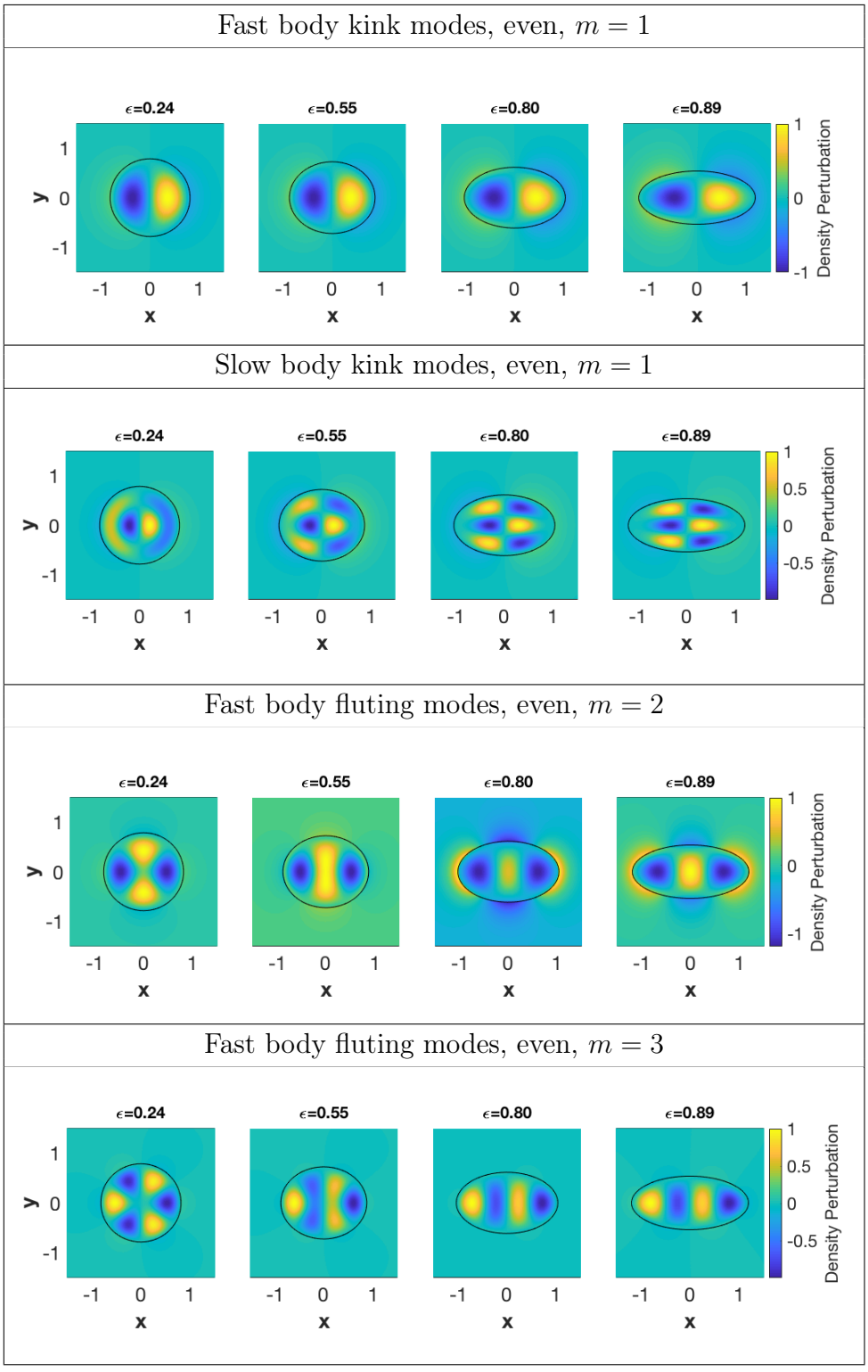

Figure 3.8: The normalised density perturbations under solar corona conditions (i.e., $v_{Ae}, v_{Ai} > c_{Si}, c_{Se}$) for the different values of eccentricity. From the top to bottom we show: the fast branch of the kink mode which has one hyperbola node and one ellipse node; the fast branch of kink mode which has one hyperbola node and two ellipse nodes; the fast branch of fluting ($m = 2$) mode which has two hyperbola nodes and one ellipse node; the fast branch of fluting ($m = 3$) mode which has three hyperbola nodes and one ellipse node. (i.e. even solution of the Mathieu equation).

3.5.1.1 Sausage mode

For the sausage modes ($m = 0$), the permitted combinations of the indices of the radial Mathieu function with respect to the major (even solution) and minor (odd solution) axes are shown in Table 3.1 and 3.2. Figure 3.6 illustrates the density perturbation of sausage modes by taking into account different eccentricity of the elliptical cross-section of the magnetic flux tube. The chosen value used to plot this mode is shown in Table E.1. The upper panels in Figure 3.6 shows the fundamental sausage modes. It is clear that as ellipticity, (ϵ) of the cross-section is increased, the sausage mode can be identified easier. However, for the case when we have higher order sausage modes (see the lower panels in Figure 3.6), the mode pattern changes in comparison to the pattern of the sausage mode for the circular cross-section. As ellipticity of the cross-section increased, the mode pattern of this mode became different from the sausage mode of the flux tube with circular cross-section (see Figure 3.6). This happens since as ellipticity of the tube increased, the length of the major axis of the flux tube increases while the minor axis of the tube shrinks. Therefore, the displacement limitation has to be extended to the first elliptic node along the major axis causing the separation of the displacement that surrounds it. As a result, for clear mode identification, it is necessary to take into account the symmetric properties of the Mathieu functions. Since $c_{2n}(\phi, m_{0i}^2) = c_{2n}(2\pi - \phi, m_{0i}^2)$, when solutions are even functions (the displacement or perturbation is polarised along the major axis) and when they have an even order expressed by $C_{2n}(s, m_{0i}^2)c_{2n}(\phi, m_{0i}^2)$, the displacement will be symmetric about the major and minor axes. Figure 3.6 shows the symmetric density perturbation with respect to the major and minor axes (see Table 3.3). The first and second panels in Table E.1 reveal the eccentricity, wave number and phase velocity which were used for visualisation of the fast body sausage mode solution under coronal conditions.

3.5.1.2 Kink mode

The parameters used to plot the kink mode ($m = 1$) are shown in the Table E.1 (see appendix E). For this set of parameters the fast body kink mode is shown in the top panels of Figures (3.7) and (3.8) while the slow body kink mode is shown in the second panels of the same figures. Since the displacement could be toward the major or minor axes, there are two polarised kink modes in the elliptical flux tube. The Mathieu functions of the even type describe the behaviour of the kink mode as a bulk transverse motion along the major

axis, while the Mathieu functions of the odd type describe the behaviour of the kink mode as a bulk of transverse motion along the minor axis. The first and second panels in Figure 3.7 illustrate the kink modes polarised along the minor axis for different flux tubes of diverse eccentricity, whereas the first and second panels in Figure 3.8 illustrate the kink modes polarised along the major axis for the different flux tubes of the diverse eccentricity. The first panel in Figures 3.7 and 3.8 represents the fundamental kink mode. As ellipticity, (ϵ) of the flux tube cross-section is increased, the fundamental kink mode can be easily identified for waves polarised along the major and minor axes.

However, as ellipticity of the flux tube cross-section is increased, the higher order kink mode polarised along the major axis appears similar to a fluting mode $m = 3$, hence, could be misinterpreted. The second panel in Figure 3.8 starting from the left displaying a kink mode for the case of the magnetic flux tube close to the circular cross-section and as one progresses to the right ends up as a kink mode with $\epsilon = 0.89$, which can lead to misinterpretation.

Alternatively, as ellipticity of the flux tube cross-section is increased, the kink overtone mode polarised along the minor axis can be easily identified. $C_{2n+1}(s, m_{0i}^2)c_{2n+1}(\phi, m_{0i}^2)$ represent the solution of the kink waves polarised along major axis. The even and odd solutions of the elliptic modes correspond to the kink mode of the circular membrane. Since $c_{2n+1}(\phi, m_{0i}^2)$=-$c_{2n+1}(\pi \pm \phi, m_{0i}^2)$, the density perturbation is symmetric about the major axis but it is asymmetric about the minor axis (see the first and second panel in Figure 3.8). $S_{2n+1}(s, m_{0i}^2)s_{2n+1}(\phi, m_{0i}^2)$ represents the solution of kink waves polarised along the minor axis. Since $s_{2n+1}(\phi, m_{0i}^2)$=$\mp s_{2n+1}(\pi \pm \phi, m_{0i}^2)$, the density perturbation is asymmetric about the major axis but it is symmetrical with respect to the minor axis i.e., the first and second panels in Figure 3.7.

3.5.1.3 Fluting modes

For fluting modes ($m \geq 2$), the values used for visualisation are presented in Table E.1. The third and fourth panels in Figures 3.7 and 3.8 illustrate perturbations in the density along the minor and major axes for different eccentricity values. From studying the third and fourth panels of Figure 3.8 it is shown that as the eccentricity of the flux tube is increased, the displacements of density merge. As a result, it may lead to the visual interpretation of these modes as a kink mode ($m = 1$). Note, the waves that are perturbed along the minor axis are less affected by the ellipticity, thus, one can clearly observe the

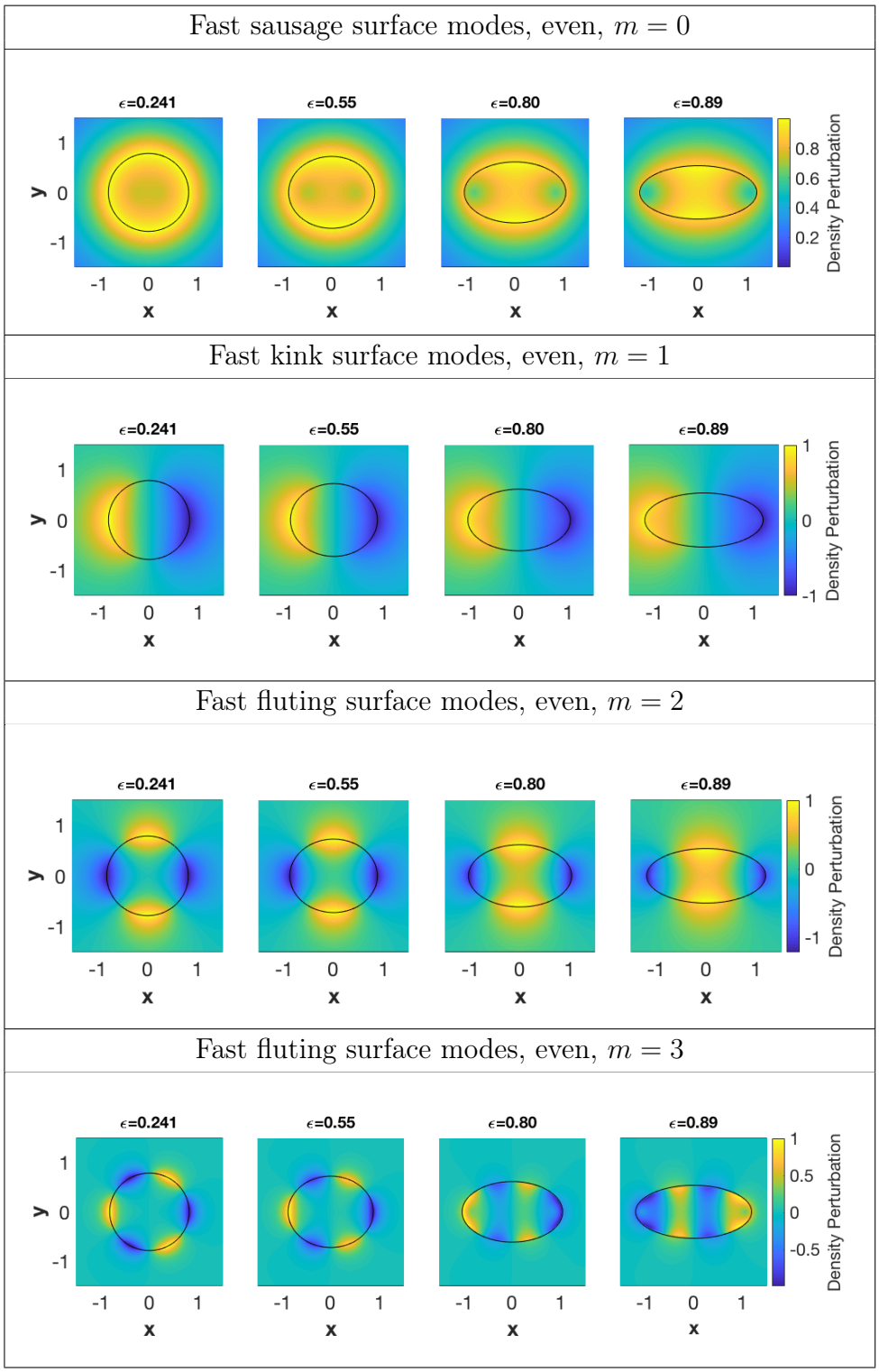

Figure 3.9: The normalised density perturbation under photospheric conditions (i.e., $v_{Ai}, c_{Se} > c_{Si}, v_{Ae}$) for different value of eccentricity. From the top to bottom on the corresponding panels we show: the fast surface branch of the sausage mode; the fast surface branch of kink mode; the fast surface branch of ($m = 2$) fluting mode; the fast surface branch of ($m = 3$) fluting mode (i.e., even solution of the Mathieu equation).

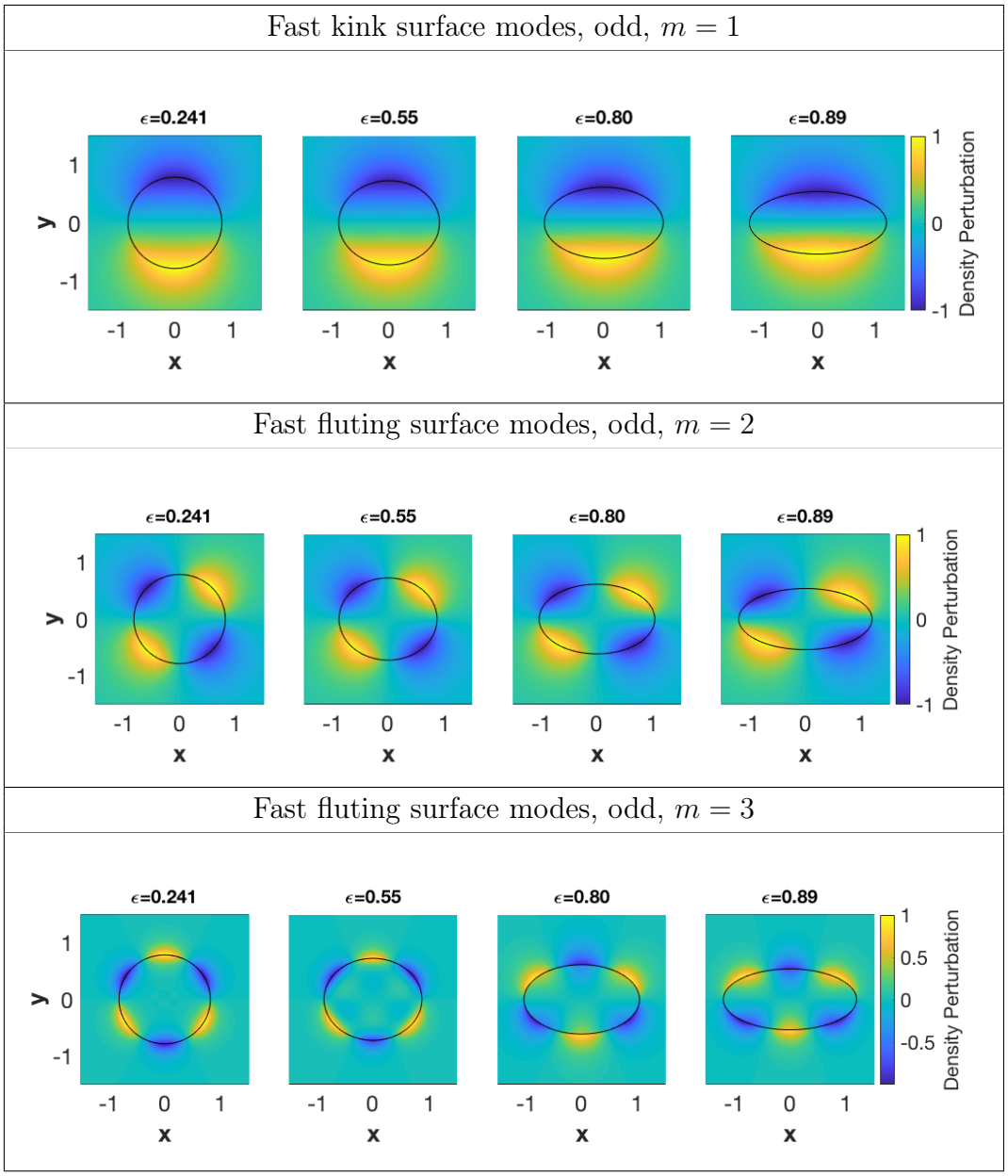

Figure 3.10: The normalised density perturbation under photospheric conditions (i.e., $v_{Ai}, c_{Se} > c_{Si}, v_{Ae}$) for the different value of eccentricity. From the top to bottom on the corresponding panels we show: the fast surface branch of the kink mode; the fast surface branch of the ($m = 2$) fluting mode; the fast surface branch of the ($m = 3$) fluting mode (i.e., odd solution of Mathieu equation).

fluting modes ($m = 2$) and ($m = 3$) as eccentricity increases, again, see the third and fourth panel in Figure 3.7.

For the fluting mode ($m = 2$), $C_{2n}(s, m_{0i}^2)c_{2n}(\phi, m_{0i}^2)$ represents the solution for perturbation along the major axis. Since $c_{2n}(\phi, m_{0i}^2)$=$c_{2n}(\pi \pm \phi, m_{0i}^2)$, the density perturbation is symmetric about both axes (see the third panel of Figure 3.8). $S_{2n+2}(s, m_{0i}^2)s_{2n+2}(\phi, m_{0i}^2)$ represents the solution for perturbation about the minor axis. Since $s_{2n+2}(\phi, m_{0i}^2)$=$\pm s_{2n+2}(\pi \pm \phi, m_{0i}^2)$, the density perturbation is asymmetric with respect to both axes (see the third panel in Figure 3.7).

For the fluting mode ($m = 3$), $C_{2n+1}(s, m_{0i}^2)c_{2n+1}(\phi, m_{0i}^2)$ represents the solution along the major axis. Since $c_{2n+1}(\phi, m_{0i}^2)$=-$c_{2n+1}(\pi \pm \phi, m_{0i}^2)$, the density perturbation is symmetric about the major axis but it is asymmetric about the minor axis (see the fourth panel of Figure 3.8). $S_{2n+1}(s, m_{0i}^2)s_{2n+1}(\phi, m_{0i}^2)$ represents the solution of fluting waves perturbed along the minor axis. Since $s_{2n+1}(\phi, m_{0i}^2)$=$\mp s_{2n+1}(\pi \pm \phi, m_{0i}^2)$, the density perturbation is asymmetric about the major axis and symmetric about the minor axis (see the fourth panel of Figure 3.7).

3.5.2 Photospheric conditions

In the next section the main attention is paid to the fast surface mode, as the slow body mode is similar to that investigated before under coronal conditions. The symmetrical properties will not be discussed as they were already presented in the section 3.5.1.

3.5.2.1 Sausage mode

The values used for visualisation of this mode are shown in Table E.2. The fast surface sausage mode is presented in the first panel on Figure 3.9. All four modes have the same wavelength, but have been calculated for different values of ellipticity, (ϵ) of the cross-section of magnetic flux tube. The first panel in Figure 3.9 shows the density perturbations which correspond to the sausage mode. As discussed before, the fundamental sausage mode is only very slightly affected by altering the ellipticity. Therefore, the identification of the surface fundamental sausage mode is easier. For example, from the first panel of the Figure 3.9, one can see that as ellipticity increased, the surface sausage mode can be identified more easily.

3.5.2.2 Kink Mode

The second panel of Figure 3.9 illustrates the density perturbation of the kink mode polarised along the major axis with differing eccentricity values in an elliptic tube while the first panel in Figure 3.10 illustrates the kink mode polarised along the minor axis. The parameters used for these calculations are presented in the Table E.2. The eccentricity of the flux tube does not affect the appearance of the kink surface mode as we only have fundamental kink surface modes unlike the body kink mode which is affected by the ellipticity of tube when we have higher order kink modes. Therefore, it is possible to observe both kink surface modes in the photosphere even if eccentricity is large.

3.5.2.3 Fluting modes

The third and fourth panels in Figure 3.9 represent the density perturbation of the $m = 2$ and $m = 3$ fluting mode, respectively. Both of them are perturbed along the major axis. The second and third panels in Figure 3.10 represent the density perturbation which corresponds to the fluting mode for $m = 2$ and $m = 3$ which are perturbed along the minor axis (see parameters used for this calculations in the Table E.2). The fluting surface modes which are perturbed along the major axis exhibit the same behaviour as fluting body modes perturbed along the major axis. It is difficult to determine the type of the mode other than the fluting surface modes perturbed along the minor axis. The second and third panels in Figure 3.10 show the fluting modes $m = 2$ and $m = 3$ as eccentricity is increased. The third and fourth panels in Figure 3.9 show that identification of the fluting modes $m = 2$ and $m = 3$ is more difficult.

3.6 Conclusions

In this Chapter, MHD modes of the magnetic flux tube with elliptical cross-section embedded in a magnetic environment are discussed. The spatial structure of wave mode identification was studied under both photospheric and coronal solar conditions. Special attention was paid to the investigation of the effect of eccentricity of a flux tube on the body modes under coronal and surface modes under photospheric conditions. The effect of the eccentricity of a flux tube varies according to the direction of the wave's polarisation along the axes with order of modes and the type of wave observed (body or surface waves).

The higher order modes are strongly affected by ellipticity of the flux tube when taking into account the direction of the polarised wave. Therefore, the higher order modes which are polarised along the major axis are strongly affected by the ellipticity of the tube, while those modes that are polarised along the minor axis are very slight effected by ellipticity. The eccentricity affects the wave modes polarised along major axis in a way that makes the mode look like another type of mode. This can lead to misinterpreting the wave mode in observations. For example, as ellipticity of the flux tube cross-section is increased, the fluting mode ($m = 3$) may be misinterpreted as a kink mode ($m = 1$) (see Figure 3.8). It is evident that the sausage mode ($m = 0$) cannot be easily identified (see Figure 3.6). As for fundamental modes, they are not affected by altering the ellipticity of the flux tube and it is easy to identify the mode type independent of the axis of perturbation, i.e. whether they are perturbed along the major or minor axis. For example, the kink overtone modes, which are polarised along the major axis are affected by ellipticity more than fundamental kink modes (see Figures 3.8 and 3.7). The body waves with higher order, which are polarised along the major axis are affected by ellipticity of the flux tube. In the case of surface waves, fluting modes ($m > 1$), which are polarised along the major axis, are only affected by the eccentricity of flux tube. All surface and body modes that are polarised along the minor axis and all the fundamental surface and body wave modes that are polarised along the minor and major axis are less sensitive to ellipticity. Despite the influence of ellipticity on the wave modes, we can identify the patterns by looking at the symmetry properties and the number of elliptical and hyperbolic nodes.

The obtained results can be useful for the interpretation of upcoming hi-resolution observations by, e.g DKIST and Solar Orbiter. It can be used for validation of MHD wave propagation in the wave-guides with non circular cross-section. This work will help both theorists and observers to understand how the spatial structure of the purely real eigenmodes are distorted from the well known circular flux tube model when ellipticity is considered. The study of the spatial structure of the MHD wave modes highlighted in this thesis opens a whole new avenue in understanding waves observed in localised magnetic structures in the Sun's atmosphere.

CHAPTER 4

MHD wave modes of solar magnetic flux tubes with realistic cross-sectional shapes

In this Chapter, we review the possibility of modelling magnetohydrodynamics (MHD) modes for direct comparison with the observational patterns. The expressions for the linear MHD perturbations of a magnetic flux tube are derived by assuming zero value of the vertical component of the velocity perturbation at the boundary of the flux tube which is in a good agreement with observations. The governing equation for the vertical velocity perturbation will be solved by taking into account the observed shape of the sunspot umbra. It is shown that the proposed model is applicable for the analysis of the slow body modes under photospheric conditions, as well as, for the fast body modes under coronal conditions. The obtained results also show that the proposed methodology works well for slow body modes for the case when k_z is very small at the boundary.

4.1 Introduction

The further understanding and interpretation of MHD waves signatures in a variety of realistic magnetic structures are important problems of modern solar physics. These waves may directly contribute to the heating of the corona. One of the key mechanisms of coronal heating could be through the damping of MHD waves (see, e.g. Cranmer 2020; Oran et al. 2017; Tiwari et al. 2019; Usmanov et al. 2016). By considering a combined transverse and torsional driver at the loop footprint, Guo et al. (2019) discussed wave based heating. The authors found that both transverse and torsional oscillations in coronal loops lead to the development of Kelvin-Helmholtz instabilities and, it therefore, may increase the effectiveness of wave heating. Karampelas et al. (2019) have studied the effects of wave heating in coronal loops via the energy dissipation from transverse waves in coronal loops by taking into account

the presence of gravitational stratification. Cases such as ideal, resistive, and viscous MHD were discussed. It was shown that the effect of gravity on the dynamic development of the system is important.

The observed MHD waves can also be used, indirectly, as a diagnostic tool for the study of properties and structure of the magnetic flux tubes. Analysis of these waves is mostly based on the theoretical models that use different types of MHD waveguides; most previous studies rely on the derivation of the dispersion relation for propagating or standing MHD waves in a simplified magnetic configurations, e.g. magnetic interface such as Musielak et al. (2000) who studied linear MHD surface wave propagation in a compressible plasma with a discontinuous interface in the magnetic field and temperature. The propagation of magnetoacoustic-gravity waves at a spherical interface was discussed by Ballai et al. (2011). The propagation of magneto-acoustic surface waves at a single density interface, in the presence of an inclined magnetic field was discussed by Vickers et al. (2018). Waves in a magnetic slab was discussed by many, including the study of sausage oscillations of plasma slabs, standing sausage modes in curved coronal slabs, and the dissipative instability that appears in a compressible partially ionized plasma slab embedded in a uniform magnetic field (see, e.g. Hornsey et al., 2014; Pascoe and Nakariakov, 2016; Mather et al., 2018). The dispersion relation for propagating or standing MHD waves in a magnetic cylinder have been studied by many, including the study of MHD waves in incompressible and compressible flux tubes with twisted magnetic fields, MHD waves in solar coronal loops, MHD waves in the solar chromosphere, and torsional Alfvén waves (see, e.g. Erdélyi and Fedun, 2006; Verth, 2007; Verth et al., 2010; Fedun and Erdélyi, 2010; Jess et al., 2015). Finally, the study of MHD wave propagation in elliptical flux tubes has been discussed by very few researches. Ruderman (2003) investigated the resonant damping of coronal loop oscillations in a magnetic tube with an elliptical cross-section in a zero plasma-β approximation. The propagation of MHD waves in finite plasma-β, compressible magnetic flux tubes with elliptical cross-sectional shapes by ignoring the explicit effects such as gravity or granular shear was investigated by Erdélyi and Morton (2009). They found that eccentricity has a strong effect on the solution behaviour.

Spectroscopic observations are one of the most important tools used to study the properties of the solar atmosphere. The identification and analysis of velocity and intensity perturbations help to obtain important information regarding the frequency and wavelength of MHD waves. For example, high

resolution UV spectroscopy provides us with high-resolution images of the solar atmosphere, which have contributed to increasing our knowledge of the dynamics of the upper layers of the solar atmosphere, (see, e.g. Bonnet 1978). Modern ground and space-based solar observatories, e.g. the Dunn Solar Telescope, Swedish Solar Telescope, Hinode etc., have already detected a number of oscillations that occur in the atmosphere of the Sun, based on spectroscopic measurements of the temporal and spatial variations of intensity and Doppler velocity emission from the chromosphere.

A number of observations (see, e.g. Sobotka et al. 1999; Mathew et al. 2003; Ryutova et al. 2008; Solanki 2003; Borrero and Ichimoto 2011; Schlichenmaier et al. 2016; Sobotka and Rezaei 2017; Keys et al. 2018; Houston et al. 2018) have shown that the cross-sectional shape of solar magnetic structures is usually far from circular. Therefore, to explain eigenmodes of the observable magnetic waveguides more precisely, it requires a more accurate representation of theoretically modelled cross-sectional shapes, as eigenmodes of waveguides are, in general, strongly determined by their cross-sectional shape Aldhafeeri et al. (2021). The theoretical studies of MHD wave propagation in the magnetic flux tubes with elliptical cross section are limited compared to those that have been devoted to the analysis of waves in waveguides with a circular cross section. The effect of ellipticity of the magnetic flux tube on MHD wave mode patterns has been analysed by Aldhafeeri et al. (2021). It has been shown, that in the case of an elliptical shape of the magnetic flux tube it is easy to misinterpret the observed wave modes. This result was the impetus for finding a new approach that clarifies and provides an accurate explanation of the type of observed wave mode patterns. In this Chapter, we have analysed the MHD wave modes in magnetic flux tubes and, in particular, in sunspots with arbitrary shape by applying the finite difference method (FDM) (see, e.g. Guo et al. 2017). Usually, FDM is used to solve a wide range of problems such as linear, non-linear, time independent and dependent problems with different kinds of boundary conditions. It has a wide use in many fields such as solving problems related to electric and magnetic fields (Binns and Lawrenson, 1973; Demerdash and Nehl, 1979; Hoole and Pearmain, 1992; Chari and Salon, 2000), physical problems such as solving problems related to stresses in a masonry dam, heating problems and flow (Kazem and Dehghan, 2018; Russell and Wheeler, 1983; Richardson and Glazebrook, 1911; Mattiussi, 2000; Ding et al., 2007; Guo et al., 2017; Demirbaş et al., 2020) and engineering disciplines such as the design of structures and hydraulic engineering (Perrone,

1978; Liszka and Orkisz, 1980; Széliga, 2014).

In this Chapter we focus on the study of the observed modes and how these wave modes change due to changes in the wave guide cross-sectional shape. The Chapter is structured as follows. In Section (4.2) we discuss the numerical model which was applied. Section (4.3) is devoted to the application of the proposed approach and the analysing of the circumstances our approach can and cannot be applied. Section (4.4) provides comparison between waves' signature in cylindrical, elliptical and irregular shape models. Section (4.5) is devoted to the study of method necessary to convert ellipse sunspots into actual shape. In Section (4.7) we conclude the results.

4.2 The numerical model

The simplest, however, illustrative model to study wave propagation in magnetic flux tubes, e.g. coronal loops, sunspots etc., is the cylindrical magnetic flux tube model (see, e.g. Wentzel 1979; Wilson 1979; Spruit 1982*b*; Edwin and Roberts 1983). This model provides the main features of the observed patterns of line of sight (LOS) magnetic and velocity perturbations. In applications to sunspots this model assumes that the oscillations are mainly confined to the umbral region and decay outside, i.e. in the penumbra. Despite the effectiveness of this model for sunspots with a circular cross-section, it cannot be applied to the patterns of MHD perturbations for sunspots with an irregular cross-section. Due to fact that the spatial structure of the eigenmodes is very sensitive to cross-sectional shape as we have shown in Chapter 3.

In our analysis of the cylindrical model, we assume that the sunspot umbra is the "internal region" of the magnetic flux tube and the penumbra is the "external region" by adopting different plasma parameters inside (i) and outside (e) the magnetic flux tube. This model requires the continuity of the radial velocity component and the total pressure (kinetic plus magnetic) across the boundary of the magnetic flux tube. However, we do not assume any preferred geometrical shape of the umbra.

By using the Cartesian coordinate system, we assume the plane of the photosphere to be the xy-plane and the vertical direction to be along the z axis. Then, we have to derive and solve the governing equation of the $\hat{v}_z$ velocity perturbation using the actual cross-sectional shape of the umbra and setting

$\hat{v}_z = 0$ at the umbra/penumbra boundary to be consistent with the observational data. The equation governing small amplitude MHD perturbations can be obtained by linearising the ideal MHD equations (see, e.g. Lighthill, 1960; Cowling, 1976; Roberts, 1981*a*; Aschwanden, 2005):

$$\frac{\partial^4 \Delta}{\partial t^4} - (c_S^2 + v_A^2)\frac{\partial^2}{\partial t^2}\nabla^2\Delta + c_S^2 v_A^2 \frac{\partial^2}{\partial z^2}\nabla^2\Delta = 0, \tag{4.1}$$

where

$$\Delta = \nabla \cdot \mathbf{v}, \quad v_A = \frac{B_0}{\sqrt{\mu_0 \rho_0}}, \quad c_S = \sqrt{\gamma \frac{p_0}{\rho_0}}.$$

Here, Δ is the divergence of velocity perturbation $\mathbf{v}$, v_A is the Alfvén speed, c_S is the speed of sound in the [medium/plasma], μ_0 is the magnetic permeability, γ is the ratio of specific heats, p_0 is the unperturbed kinetic plasma pressure and ρ_0 is the unperturbed plasma density. By using the Fourier form of Δ:

$$\Delta = \hat{v}_z(x, y)\exp[i(\omega t + kz)], \tag{4.2}$$

after some algebra one can obtain the internal governing equation of the $\hat{v}_z$ velocity perturbation is of Helmholtz type, i.e.

$$\frac{\partial^2 \hat{v}_z}{\partial x^2} + \frac{\partial^2 \hat{v}_z}{\partial y^2} - m_i^2 \hat{v}_z = 0, \tag{4.3}$$

where m_i^2 is the eigenvalue:

$$m_i^2 \quad = \quad \frac{(k_z^2 c_{Si}^2 - \omega^2)(k_z^2 v_{Ai}^2 - \omega^2)}{(c_{Si}^2 + v_{Ai}^2)(k_z^2 c_{Ti}^2 - \omega^2)}. \tag{4.4}$$

Here k_z is the vertical wavenumber, ω is the angular frequency and $c_{Ti} = \sqrt{\frac{c_{Si}^2 v_{Ai}^2}{c_{Si}^2 + v_{Ai}^2}}$ is the tube speed.

To identify the wave modes in the sunspot umbra, the following procedures have been applied: first, the shape of the umbra was determined by identifying its boundaries as vertices in the xy-coordinate system using TRACEBOUNDARY command in MATLAB (see Appendix F). Second, the eigenfunctions of Equation (4.3) for the particular geometry have been calculated, based on the eigenvalue m_i^2 in Equation (4.3). Implicit parameters of m_i^2 cannot be estimated from the observation data explicitly, however, this does not actually matter since we are interested in modelling the spatial structure of the eigenfunctions accurately and this only requires calculating the numerical values of m_i^2 which solve the eigenvalue problem subject to the stated boundary conditions. Then, we solve Equation (4.3) numerically using the standard DELSQ routine in MATLAB, which is a MATLAB implementation of the ARnoldi

PACKage (Lehoucq et al., 1998). This routine discretizes the domain for use as an input for EIGS. After that, we solve the final system of equations using EIGNS command in MATLAB. Finally, we obtain a set of discrete solutions of Equation (4.3).

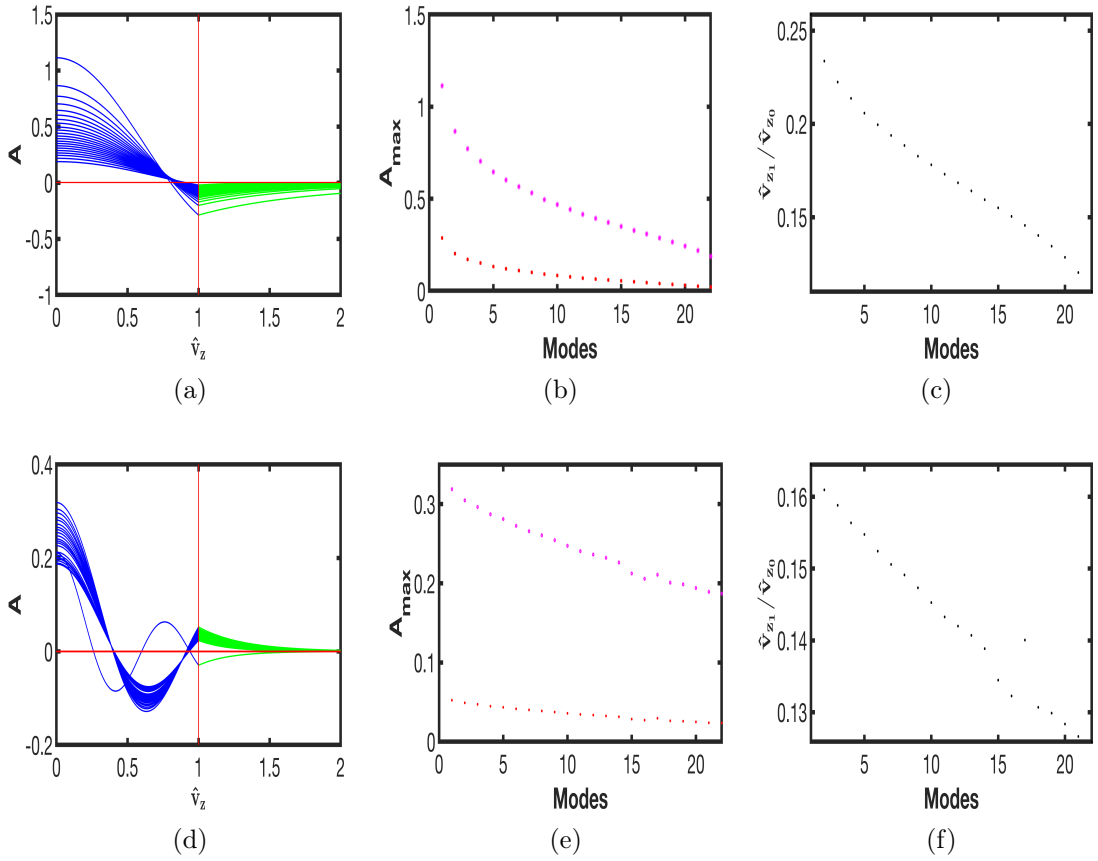

Figure 4.1: In panels (a), (b), and (c) we plot the behaviour of various slow sausage body modes calculated under photospheric conditions for the chosen value ($m_i < 4$). The same modes are shown in panels (d), (e), and (f) but for the chosen value $m_i \geq 4$. The the top (a) and bottom (d) left panels show dependence of the amplitude of $\hat{v}_z$ in z direction inside the tube (indicated in blue) and outside (green). The maximum amplitude of $\hat{v}_z$ inside the flux tube and at the boundary, are shown in the middle panels (b) and (d). The purple dots indicate the maximum amplitude of $\hat{v}_z$ inside the flux tube for various modes while the red dots show the maximum amplitude at the tube boundary. The ratio between maximum $\hat{v}_{z_1}$ at the boundary and the $\hat{v}_{z_0}$ is maximum of $\hat{v}_{zi}$ (inside the flux tube).

4.3 Applications of actual shape model

In this Section we discuss the conditions under which our numerical model can be used. Therefore, we study in detail the solutions obtained in a cylindrical geometry. Performing this study allows us to know when the $\hat{v}_z$ perturbation effect is very small on umbra/penumbura boundary. This is roughly consistent with proposed numerical model, which assumes $\hat{v}_z = 0$ at the umbra/penumbra boundary. Therefore, we have solved the following dispersion equations under cylindrical coordinates model (see, e.g. Spruit, 1982*b*; Edwin and Roberts, 1983; Aschwanden, 2005):

For surface waves ($m_i^2 > 0$), the dispersion relation takes the form

$$\rho_i(k^2 v_{Ai}^2 - \omega^2) m_e \frac{K_n'(m_e a)}{K_n(m_e a)} = \rho_e(k^2 v_{Ae}^2 - \omega^2) m_i \frac{I_n'(m_i a)}{I_n(m_i a)}. \tag{4.5}$$

For body waves ($m_i^2 = -n_i^2 < 0$), the dispersion relation takes the form

$$\rho_i(k^2 v_{Ai}^2 - \omega^2) m_e \frac{K_n'(m_e a)}{K_n(m_e a)} = \rho_e(k^2 v_{Ae}^2 - \omega^2) n_i \frac{J_n'(n_i a)}{J_n(n_i a)}, \tag{4.6}$$

where,

$$m_e^2 = \frac{(k^2 c_{Se}^2 - \omega^2)(k^2 v_{Ae}^2 - \omega^2)}{(c_{Se}^2 + v_{Ae}^2)(k^2 c_{Te}^2 - \omega^2)}, \tag{4.7}$$

$$c_{Te}^2 = \frac{c_{Se}^2 v_{Ae}^2}{c_{Se}^2 + v_{Ae}^2}. \tag{4.8}$$

Here, a is the radius of the magnetic flux tube, v_{Ae}, c_{S_e}, c_{Te}, ρ_e are the Alfvén speed, the sound speed, the tube speed and the plasma density outside of the tube respectively. K_n, I_n and J_n are the Bessel functions and the 'prime' denotes the derivative of Bessel function. The dispersion relationship provides the relation between the longitudinal wave number k (along the axis of the cylinder), and the frequency ω. Using the k and ω that are obtained from the dispersion relations 4.5 and 4.6, we plot and test the $\hat{v}_z$ component of velocity under coronal and photospheric conditions. We write $\hat{v}_z$ as the following:

$$\hat{v}_{zi} = -A_i \frac{ikc_{Si}^2}{\omega^2} J_n(m_i a),$$

$$\hat{v}_{ze} = -A_e \frac{ikc_{Se}^2}{\omega^2} K_n(m_e a),$$

where A_i and A_e are arbitrary constants to be determined.

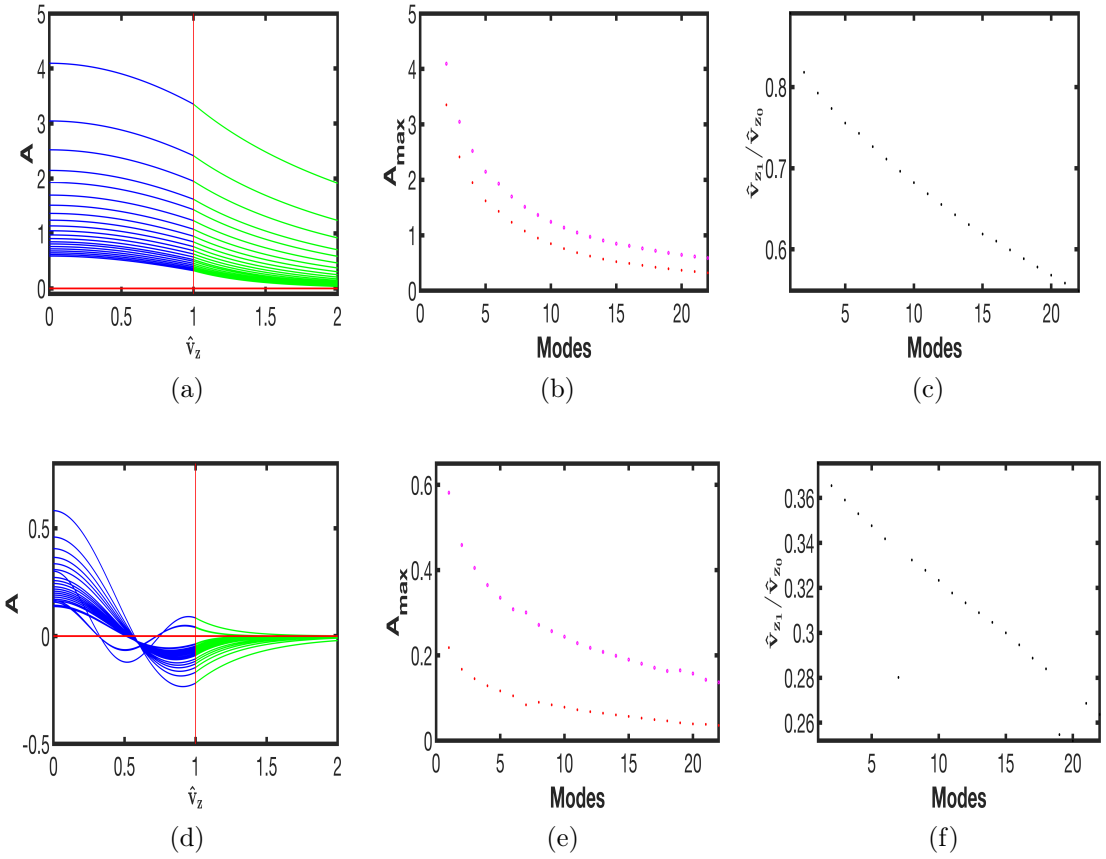

Figure 4.2: In panels (a), (b), and (c) we show the behaviour of various slow sausage body modes, calculated under coronal conditions for the chosen value ($m_i < 4$). The same modes are shown in panels (d), (e), and (f) but for the chosen value $m_i \geq 4$. The top (a) and bottom (d) left panels show dependence of the amplitude of $\hat{v}_z$ in z direction inside the tube (indicated in blue) and outside (green). The maximum amplitude of $\hat{v}_z$ inside the flux tube and at the boundary, are shown at the middle panels (b) and (e). The purple dots indicate the maximum amplitude of $\hat{v}_z$ inside the flux tube for various modes while the red dots shows the maximum amplitude at the tube boundary. The ratio between maximum $\hat{v}_{z_1}$ at the boundary and the $\hat{v}_{z_0}$ is maximum of $\hat{v}_{zi}$ inside the flux tube is shown in the rights panels (c) and (f). A is the amplitude of $\hat{v}_{zi}$.

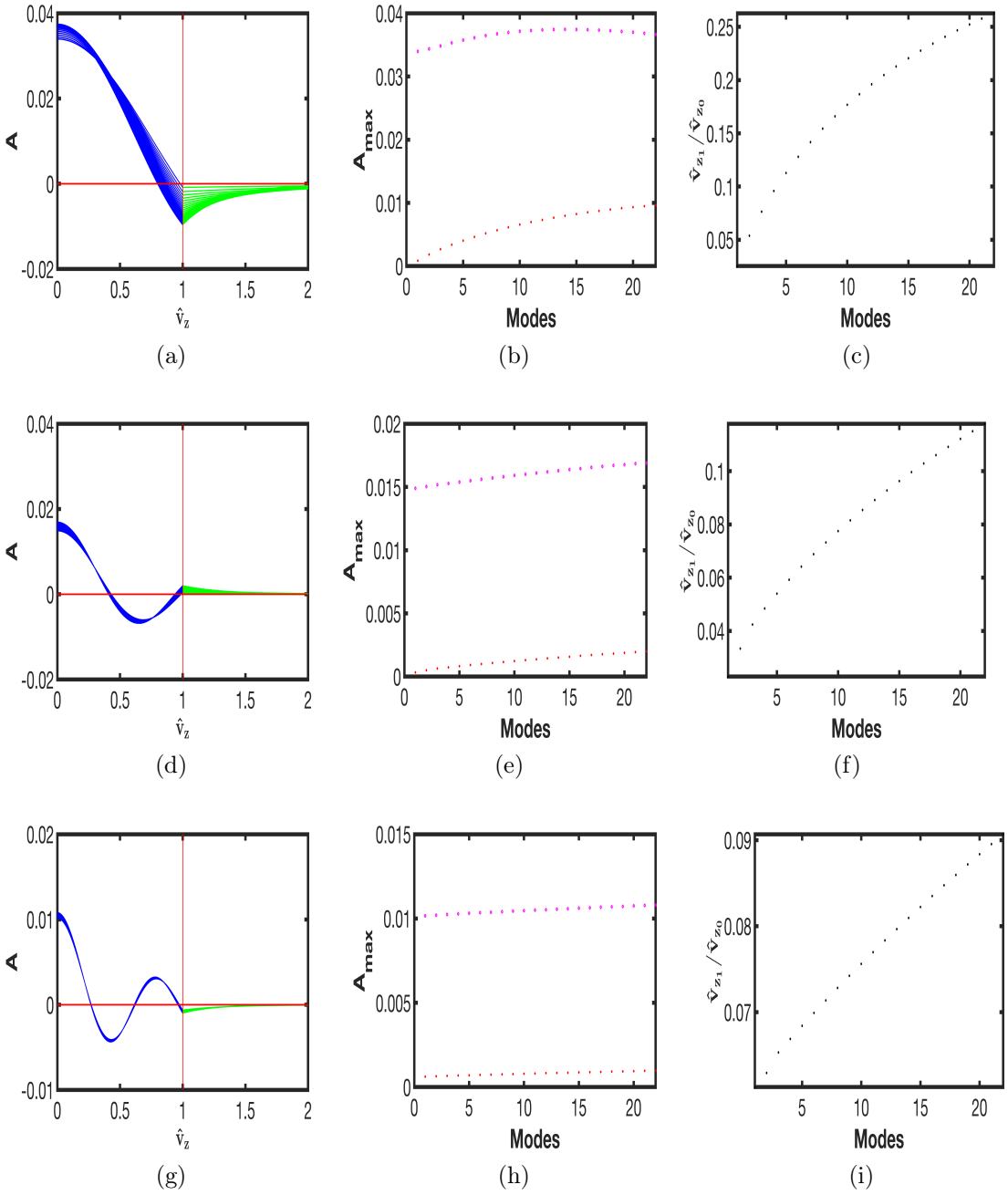

Figure 4.3: In panels (a), (b), and (c) we show the behaviour of various fast sausage body modes, calculated under coronal conditions for the chosen value ($m_i < 4$). The same modes are shown in panels (d), (e), and (f) but for the chosen value ($4 \leq m_i < 8$). In panels (g), (h), and (i), we show various a fast sausage body modes for the chosen value ($m_i \geq 8$). The three left panels, (a), (d) and (g), show the dependence of the amplitude of $\hat{v}_z$ in z direction inside the tube (indicated in blue) and outside (green). The maximum amplitude of $\hat{v}_z$ inside the flux tube and at the boundary, are shown at the middle panels (b), (e) and (h). The purple dots indicate the maximum amplitude of $\hat{v}_z$ inside the flux tube for various modes, while the red dots show the maximum amplitude at the tube boundary. The ratio between maximum $\hat{v}_{z_1}$ at the boundary and $\hat{v}_{z_0}$ has maximum value of $\hat{v}_{zi}$ inside the flux tube are shown in panel (c), (f) and (i).

4.3.1 Test 1: Photospheric conditions

Here we show the $\hat{v}_z$ component for various ω and k which have been obtained from solving Equation (4.6) under photospheric conditions, i.e. $v_{Ai} > c_{Se} > c_{Si} > c_{Ti} > v_{Ae} > c_{Te}$. For illustrative purposes we have taken $c_{Si} = 1$, $v_{Ai} = 2c_{Si}$, $c_{Se} = 1.5c_{Si}$ and $v_{Ae} = 0.5c_{Si}$. These particular conditions play a key role in determining the types of MHD wave modes that can be supported by the considered waveguide. In particular, under these conditions the MHD wave modes are:

- with the largest phase speeds, v_{ph}, in the z direction are surface modes with $v_{ph} \in [c_{Si}, c_{Se}]$,
- slow body modes with the phase speed $v_{ph} \in [c_{Ti}, c_{Si}]$,
- slow surface modes with the phase speed $v_{ph} \in [v_{Ae}, c_{Ti}]$.

We have plotted $\hat{v}_z$, only for the slow body modes, as shown in Figure 4.1. Here, we have ignored solving Equation (4.5) for the surface wave modes because the surface wave is evanescent within the umbra and has maximum amplitude at the umbra/penumbra boundary. This contradicts the hypothesis of the new model, which assumes the $\hat{v}_z$ component will be evanescent at the boundary. We found that the slow body modes under the photospheric conditions have a slight effect at the umbra/penumbra boundary while there is a strong effect inside the umbra (see Figure 4.1). This figure shows $\hat{v}_z$ with analysis of the maximum possible amplitude inside and outside of the tube. It can be clearly seen from panels (a) and (d) of Figure 4.1 that the modes do not perturb the boundary much. The amplitude of $\hat{v}_z$ at the boundary is close to 0, see the red star in panel (b) and (e) of Figure 4.1 which shows the maximum amplitude at the tube boundary. The ratio between the maximum amplitude inside the boundary and at the boundary of the umbra/penumbra region is about 0.1 and 0.3 for both fundamental modes and higher order modes (see panels (c) and (f) of Figure 4.1). We note here that under photospheric conditions there are no fast body modes, but there are fast surface modes and these modes are not consistent with the ones present in our model.

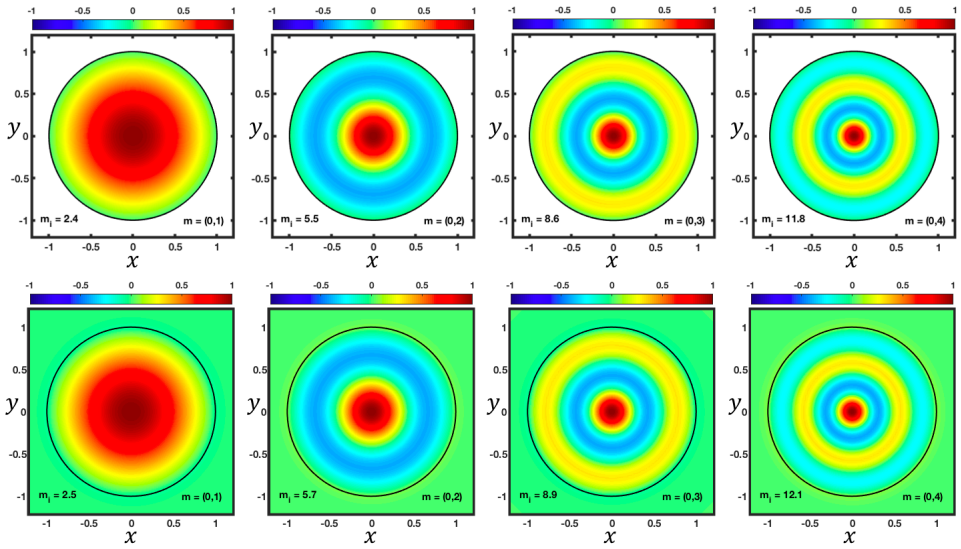

Figure 4.4: Upper panels show different branches of sausage modes obtained by numerical model. Lower panels show different branches of the slow body of sausage modes obtained by cylindrical model. $m = (a, b)$ denotes the type of modes and branch i.e, $a = 0$ means the sausage mode and $b = 2$ means the second branch of solution.

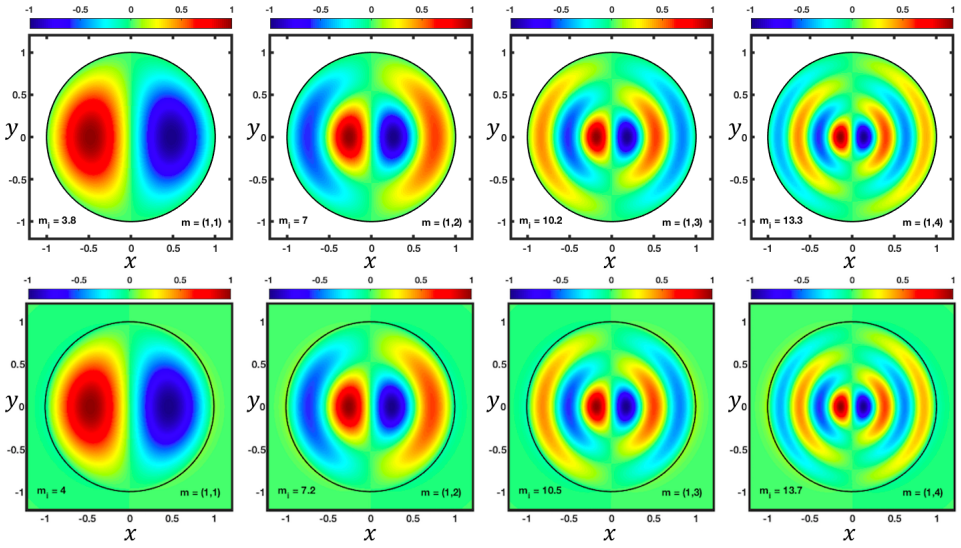

Figure 4.5: Upper panels show different branches of kink modes obtained by numerical model. Lower panels show different branches of the slow body of kink modes obtained by cylindrical model. $(m = (a, b))$ denotes the type of modes and branch i.e, $a = 1$ means the kink mode and $b = 2$ means the second branch of solution.

4.3.2 Test 2: Coronal conditions

Under coronal conditions, we should assume that the internal plasma temperature, density and pressure are greater than at the external region and internal magnetic field strength is less than external.. This leads to the following relations between the characteristic plasma speeds: $v_{Ae} > v_{Ai} > c_{Si} > c_{Ti} > c_{Se} > c_{Te}$. For modelling purposes we have taken $c_{Si} = 1$, $v_{Ai} = 2c_{Si}$, $c_{Se} = 0.5c_{Si}$ and $v_{Ae} = 5c_{Si}$. With these particular assumptions, we found an important consequence for the types of MHD wave modes that can be supported by such a waveguide: the fast body modes propagate with phase speed $v_{ph} \in [v_{Ai}, v_{Ae}]$ and the slow body modes propagate with phase speed $v_{ph} \in [c_{Ti}, c_{Si}]$ in the z direction. Here we present the $\hat{v}_z$ component for various ω and k_z which have been obtained by solving Equation (4.6). We have plotted $\hat{v}_z$ for the slow and fast sausage body modes, shown in Figures 4.2 and 4.3, respectively. Our result show that the fundamental slow modes (i.e one circular node (the outside edge)) have an effect on the boundaries, and that the amplitude at the boundary is very close to the maximum amplitude within the tube (see panel (a) of Figures 4.2). It is obvious from panel (b) of Figure 4.2 that the maximum amplitude of $\hat{v_{z_1}}$ at the boundary is very close to the maximum amplitude of $\hat{v}_{z_0}$ inside the umbra. The ratio between $\hat{v}_{z_1}$ and $\hat{v}_{z_0}$ are high, i.e. between 0.4 and 0.80 (see panel (c) of Figure 4.2).

In addition, we have studied the higher order radial modes (i.e more than one radial node) for the slow body modes separately, and we found that this kind of mode has a small effect on the boundary, which is smaller than the effect of fundamental modes (see panel (d) and (e) of Figure 4.2). The higher order modes have about half of the effect of that caused by fundamental modes.

In the case of the fast body modes, we have found that they have a slight effect on the umbra/penumbra boundary, and their effect is similar to the effect of slow body modes under the photospheric conditions. Both have an amplitude of $\hat{v}_z$, on umbra/penumbra boundary, very close to zero whilst, within the umbra, the amplitude is large. We also note that the higher order modes have less impact at the umbra/ penumbra boundary. As radial nodes increase, the ratio between $\hat{v}_{z_1}$ and $\hat{v}_{z_0}$ decreases (see panel (c), (f) and (i) of Figure 4.3 from top to bottom).

4.3.3 Modes test

In the previous section, we have shown for all cases that can be used with the model by testing the $\hat{v}_z$ component of velocity. In this Section we will show

the 2D plot of the $\hat{v}_z$ component to analyse the extent, to which, the cylinder tube model corresponds to our numerical model. Here we review the sausage and kink slow body modes under photospheric conditions. Figures 4.4 and 4.5 show the value of $\hat{v}_z$ for sausage modes and kink modes, respectively. The comparison of sausage modes with our numerical and cylindrical model are shown in Figure 4.4. Four different branches of sausage mode were chosen, which are represented by $m = (0, 1)$, $m = (0, 2)$, $m = (0, 3)$ and $m = (0, 4)$ where, 0 indicates the sausage mode and 1,2,.. indicate the branch. Figure 4.5 illustrates four different branches of kink modes which have been obtained by both the numerical and cylindrical model. It is clear from Figures 4.4 and 4.5 that the numerical model is consistent with the cylindrical model for all modes presented. The cylindrical model has an amplitude of $\hat{v}_z$, at the umbra/penumbra boundary, very close to zero and this is consistent with the numerical results which has zero amplitude at umbra/penumbra boundary.

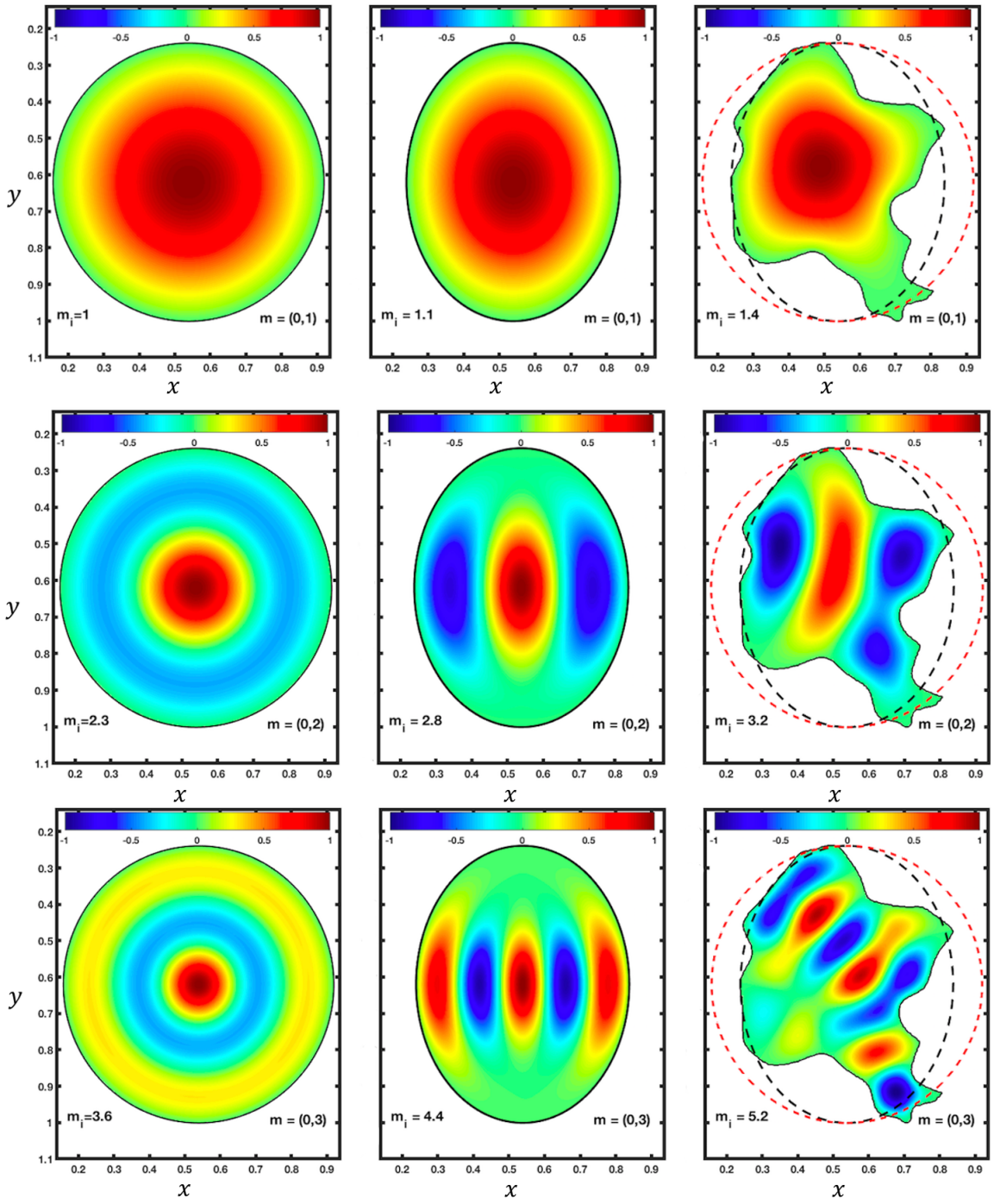

Figure 4.6: The columns from left to right represent the eigenfunction of circular, elliptical and irregular sunspots, respectively. The rows from top to bottom represent the fundamental sausage mode ($m = (0, 1)$), second overtone sausage mode ($m = (0, 2)$) and third overtone of sausage modes ($m = (0, 3)$), respectively. The dashed red and black lines denote the circular and elliptical shape.

4.4 Cylinder model vs actual shape model vs elliptical model

The modal basis used for the modeling of sunspots of irregular shape, which is shown in right panel of Figure 4.6, was computed numerically. The shape in the right panel of Figure 4.6 is not an actual umbral boundary. It is a synthetic image to resemble a non-standard sunspot. We have chosen 1332 discrete points around the umbra/penumbra boundary to model the eigenfunctions with sufficient resolution. We have generated a 68397 x 68397 matrix using DELSQ and found the first 50 eigenvalues and eigenfunctions, and we have shown 3 of them in right columns of Figure 4.6. By using the same methods, we also analysed the first 50 eigenvalues and eigenfunctions of circular and elliptical shapes. Three of them are shown in the left and middle columns of Figure 4.6, respectively. The sausage modes have been plotted for each of the three shapes. It is clear, that the observed mode is the fundamental sausage mode in each of the of three shapes, seen in the first row of Figure 4.6. However, the situation is completely different with the higher order modes. The second row of Figure 4.6 (right panel) represents the sausage mode of the irregular shape, but the obtained pattern does not represent a usual sausage mode (in case of cylindrical geometry). In the case of an elliptical shape (middle panel) this mode is more similar to the kink mode, while it appears as a clear sausage mode in cylindrical geometry (left panel).

We found that the lower order modes are not affected much by the changing of their shape, but the higher-order modes, even with a small-scale spatial structure, are affected by the changing of their shape significantly (see the irregular and elliptical shape in the second and third row of Figure 4.6). Due to the fact that the spatial structure of the eigenmodes is very sensitive to the cross-sectional shape, especially in the higher order modes, we need at least the elliptical model to interpret the observed modes. As we note in the second and third rows of Figure 4.6, the elliptical modes better explain the modes in the irregular shape than the circular does.

4.5 Converting elliptical sunspots into the actual shape

We mentioned in the previous Section that we need at least the elliptical shape in order to give explanations for the patterns that appear in the irregular

shapes. In order to make sure that we can actually use the elliptical shape to interpret these patterns, we have created an algorithm (see appendix G) that works as follows:

- Find the closest ellipse to the desired sunspots shape.
- Gradually transforms the elliptic shape into sunspots shape.
- Apply the numerical method in the Section 4.2 to all shapes obtained from Step 2 and find the desired pattern for all these shapes.

The algorithm has been used on one of the sunspots close to an elliptical shape and we have found many interesting patterns in the eigenfunctions. Here we have illustrated two modes in Figure 4.7 and 4.8. It is clear that the shape begins to convert from ellipse (left) to actual sunspots (right). Figure 4.7 represents the fundamental sausage mode. We can clearly observe the sausage pattern in each of the five shapes, which confirms that the elliptical shape did indeed give a correct interpretation of the observed pattern in actual sunspots. We have previously mentioned that the fundamental modes are not significantly affected by the shape of the borders of sunspots, so the sausage pattern is evident in each of the five shapes in the image. Figure 4.8 shows what the traditional kink pattern associated with the cylindrical model looks like in each of the five shapes. We also note that as the shape of the waveguide is deformed, the kink pattern becomes completely unrecognisable. However, the gradual and smooth change in the mode in each of the five shapes fully proves that we can rely on the modes that appear in the elliptical shape to explain the patterns that appear in the actual shape. In addition, Figure 4.8 illustrates how sensitive the higher order modes are to the shape of the sunspots.

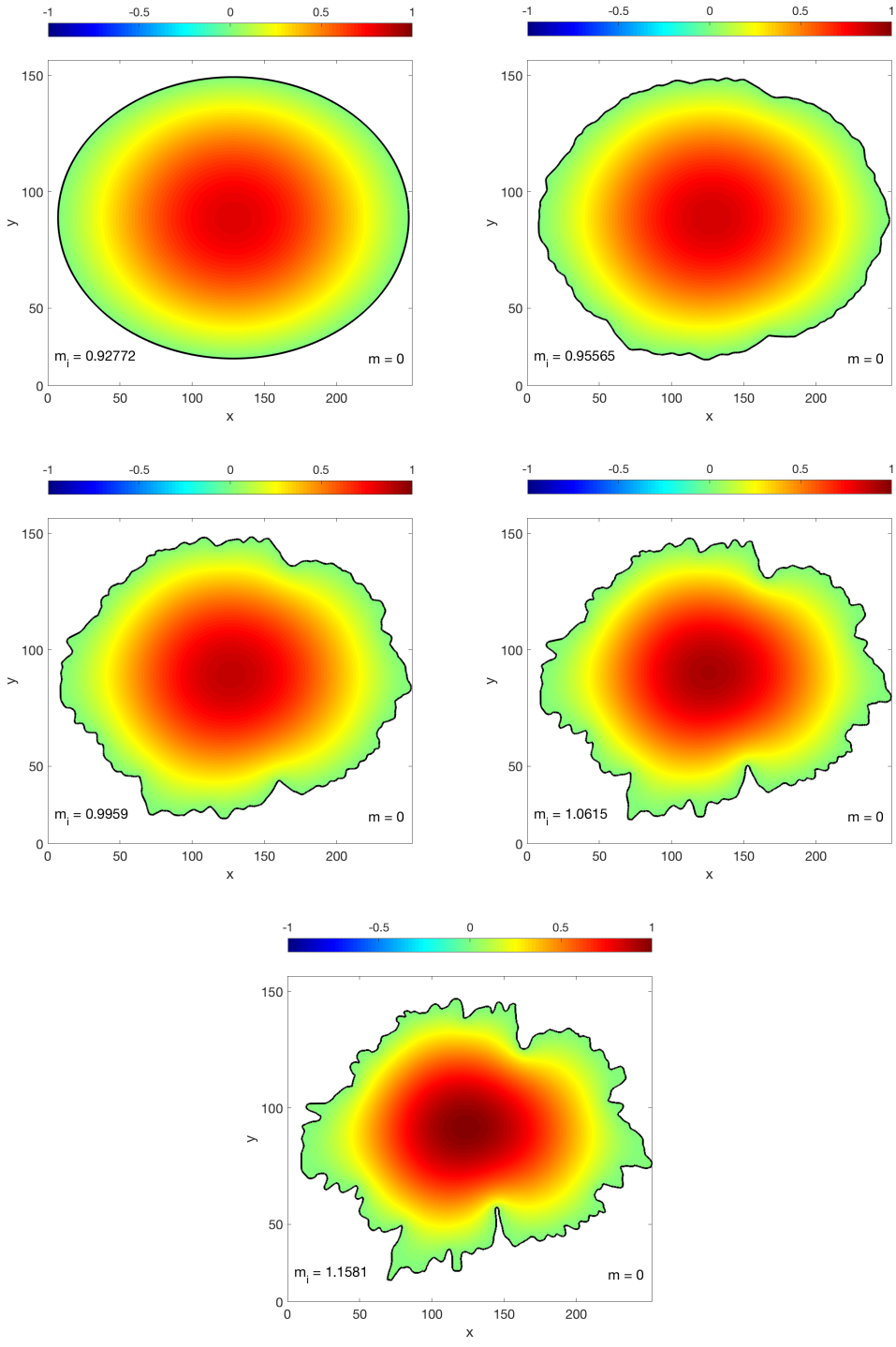

Figure 4.7: From the left to right we show how the shape can be deformed from ellipse to actual sunspots shape. The pattern of the fundamental sausage mode ($m = 0$) is shown for each of the shapes.

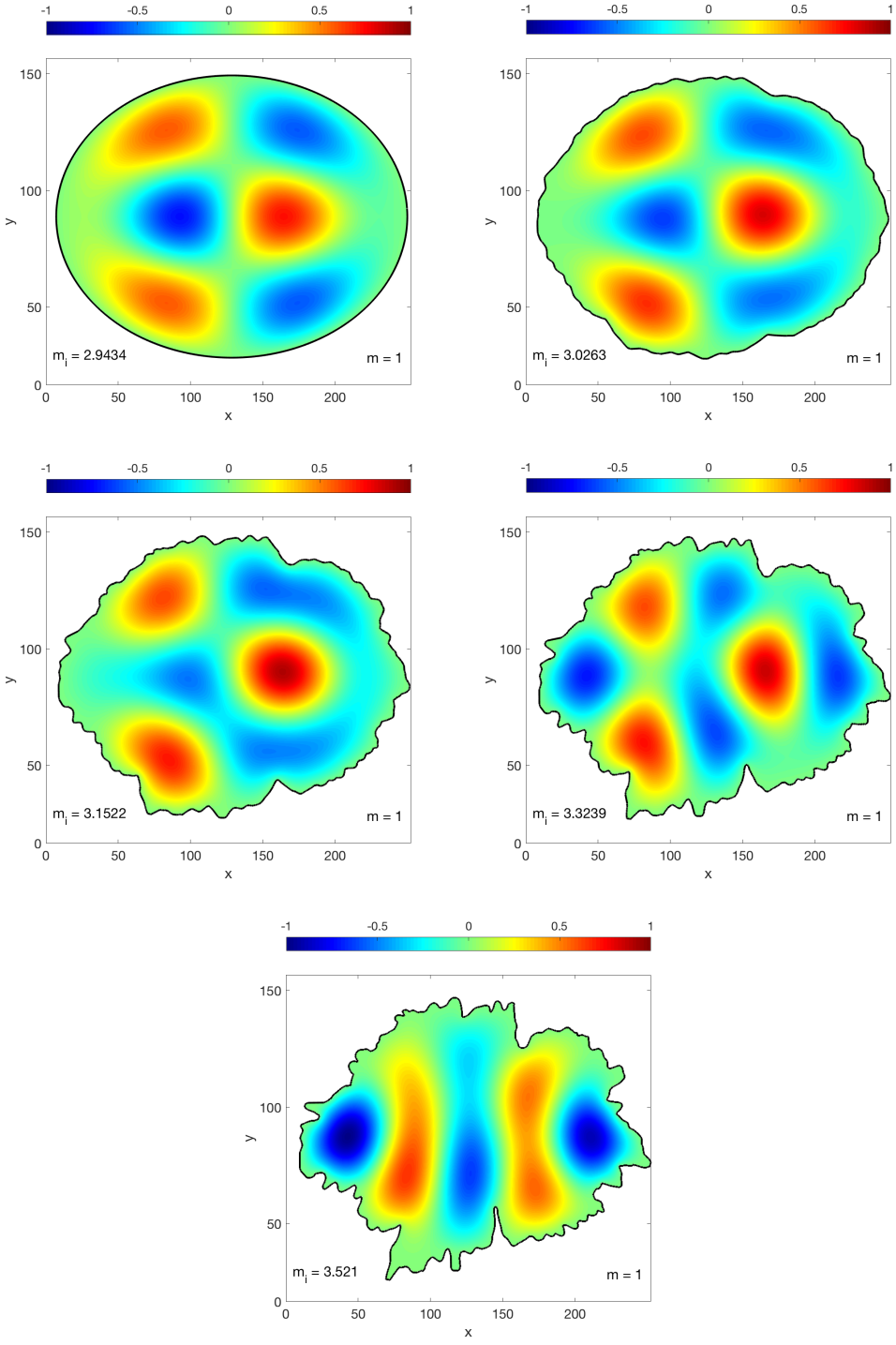

Figure 4.8: From left to right we show how the shape changes from the ellipse to actual sunspots. The second higher order kink mode ($m = 1$) is shown for each of the shapes.

4.6 Is it possible to rely on the cylindrical model to explain the observed patterns in the actual shape?

The wave propagation in cylindrical magnetic flux tubes has been studied for years, and this model has been relied upon to explain the patterns of the observed waves in sunspots, as we did in Section 2.3. Here we will apply our numerical model to the same sunspot that we used previously after we confirmed that it is possible to apply this model for slow body wave in photosphere (see Section 4.3). In Section 2.3, we interpreted the MHD wave in Figure 2.4 as a sausage mode using the cylindrical model. Figure 4.9 represents the eigenfunction using the actual shape of sunspots in Figure 2.4 and the eigenfunctions of an elliptical waveguide which have been obtained by numerical methods. The eignfunction of the actual sunspot shape has also been obtained by using the same numerical method. It is obvious from Figure 4.9 that the mode obtained by numerical methods using the actual shape is close to observational data. The cylinder model gives the same phase and amplitude in each sausage mode annulus. However, in observational data the annuli are more patchy. In our numerical model this "patchiness" is caused by the irregular cross-sectional shape as Figure 4.9 shows. We can say here that it is possible to rely on the circular model to explain the observed patterns if the sunspot shape can be approximated as a circle. Nevertheless, we see that relying on flux tubes with an elliptic cross-section is more preferable, because actually most sunspots cannot be approximated by a circle, but rather by an ellipse that has small eccentricity.

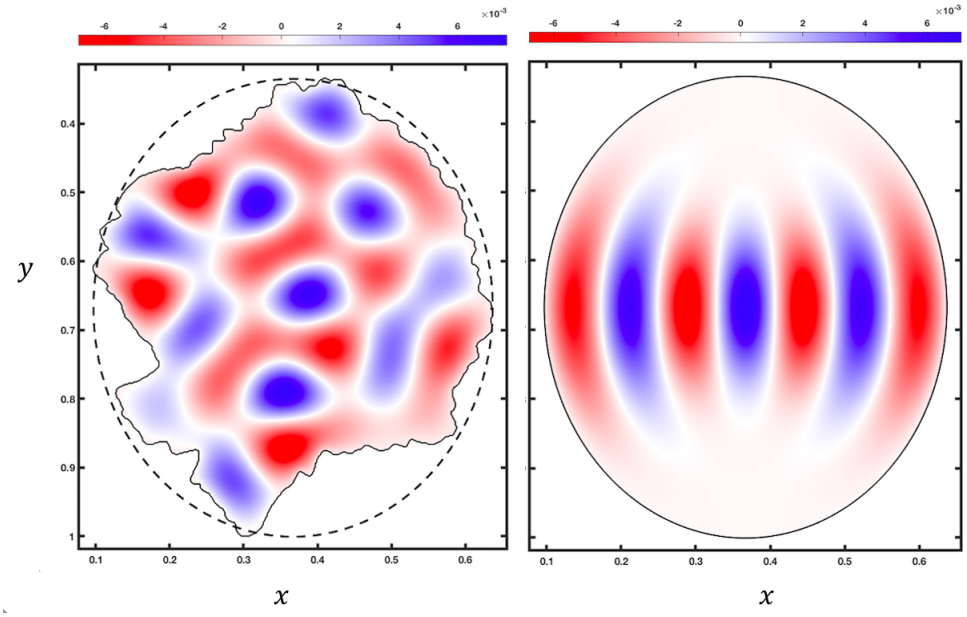

Figure 4.9: The left panel shows the mode obtained by the numerical model after taking into account the boundary of the sunspots have shown on Figure 2.4. The right panel shows the mode of the approximation ellipse of the sunspots (the dashed line).

4.7 Conclusions

The proper interpretation and identification of wave modes detected in the observational data is important for understanding of plasma processes in the solar atmosphere and their connection to space weather. In this Chapter we discussed the possibility of applying a numerical model to provide explanations for the MHD patterns that may be detected in observational data. We also discussed when can we use this form and under what conditions. We concluded in this research that this model cannot be applied to surface waves because surfaces waves are evanescent within the umbra and have maximum amplitude at the umbra/penumbra boundary. We also concluded that this model can be applied to slow waves under the conditions of the photosphere, because its effect on the boundaries is very small. Surprisingly, we found that the numerical model cannot be applied to slow modes under the conditions of the corona because it has an effect on the boundaries, and its amplitude at the borders is very close to its amplitude within the boundary of the umbral region. Nevertheless, this model can be applied to fast modes under coronal conditions; the reason may be due to the fact that when plasma-β is high, slow

waves propagate mainly along magnetic field lines, while when plasma-β is low fast waves propagate mainly along magnetic field lines. We also conclude that the higher modes are very sensitive to the cross sectional shape, so this must be taken into account when analysing and studying the observed patterns in order that waves are not misinterpreted.In this Chapter, we have shown to what extent the cross-sectional shape of the waveguide affects the observed modes and how simple cross-sectional shapes of waveguides, such as a circle, may not give a correct interpretation of the observed modes or cannot provide an explanation of some modes.

CHAPTER 5
Conclusions

5.1 Overview of thesis

The present Thesis constitutes a study of MHD modes in solar magnetic flux tubes with various cross-sectional shapes. Chapter 1 introduces the background material that is needed for MHD wave theory. The equations of ideal MHD were derived from Maxwell's equations and the equations of fluid dynamics. The dispersion relation of wave propagation in unbounded and homogeneous plasma and in a structured plasma such as interface and slab were derived.

MHD wave propagation in cylindrical magnetic flux tubes was studied and reviewed in Chapter 2. In this Chapter, we derived the dispersion relation in such structures and then we presented the algorithm used for solving the dispersion equations. In addition, we have tested the effectiveness of this method by solving the dispersion equations and comparing results with the results obtained previously.

The behaviour of MHD wave propagation in magnetic flux tubes with ellipticial cross section was investigated in Chapter 3. It involved the derivation and study of the dispersion relations. We also studied the effect of ellipticity on solutions of the dispersion relations, in addition to giving an idea of how to observe patterns in elliptical magnetic flux tubes and to what extent the ellipticity of tube affects these patterns.

In Chapter 4 we studied MHD wave modes by considering the actual shape of sunspot boundaries. We solved the governing equation for the $\hat{v}_z$ velocity perturbation by setting $\hat{v}_z = 0$ at the umbra/penumbra boundary to be consistent with the observational data. We discussed how the modes appeared in the flux tube using the actual shape and compared them in the shape of the modes in both the cylindrical and elliptical model.

5.2 Summary of results

5.2.1 Chapter 2

The dispersion relation of waves propagating in a cylindrical flux tube was obtained in Section 2.1.3. We obtained a good agreement with the results of Edwin and Roberts (1983) using the new algorithm. It was found that there are a slow body waves and fast surface waves under photospheric conditions in in Section 2.2.3. The slow and fast body waves were obtained under coronal conditions in Section 2.2.4.

5.2.2 Chapter 3

The dispersion relation of waves propagating in an elliptical flux tube was derived in Section 3.2.3. The solutions were obtained under coronal and photospheric conditions in Section 3.3 and 3.4, respectively. We found that there are slow and fast body waves under coronal condition while there are slow body waves and fast surface waves under photospheric conditions. We showed that there are two kink waves polarised along the major and the minor axes in an elliptical flux tube. The effect of increasing ellipticity is that it increases the difference between the phase speed for modes polarised along the minor and the major axes. The body waves polarised along minor axes have a phase speed greater than those polarised along major axes. However, surface waves polarised along the minor axes have a phase speed less than those polarised along major axes. The MHD wave modes of elliptical flux tubes under coronal and photospheric conditions were obtained in Section 3.5. It was found that the effect of ellipticity is greater on the patterns with higher order and on the polarizing waves on the main axes. In addition, we found that the fundamental modes, such as sausage or kink fundamental modes, beside the polarised waves along the minor axes are less affected by the eccentricity of the flux tube. The surface modes of higher order are more strongly affected by eccentricity than the fundamental surface modes.

5.2.3 Chapter 4

In Section 4.2, the MHD equations were derived in two dimensions using Cartesian coordinates. The numerical results have a very good agreement with the results obtained using the cylindrical model in Section 4.4. The numerical model is very applicable for slow body waves under photospheric conditions,

but it is also applicable for fast body waves under coronal conditions as in Section 4.3. We found that the numerical model is not applicable for slow or fast surface waves. It was concluded that the higher modes are more sensitive to shape of sunspots than fundamental modes in Section 4.4.

5.3 Future work

In solar physics the theory of MHD wave modes in cylindrical magnetic waveguides is well developed. However, realistic forward modelling of the observable signatures of such wave modes to compare them with high resolution data of the Sun's atmosphere is still in its infancy. One of the most important extensions to the investigation, which was performed in Chapter 2 is to forward model how the actual integrated spectral line intensity and Doppler velocity of such MHD wave modes will appear in observational data depending on the particular wavelength used and the observer's line of sight with respect to the magnetic cylinder axes.

Apart from the work in this Thesis the study of waves in an elliptical flux tube has not received much attention in solar physics. An interesting extension to the work in Chapter 3 will be to obtain a dispersion relation for linear wave propagation in a twisted incompressible elliptical magnetic waveguide because of the natural occurrence of twisted magnetic flux tubes from the Sun's interior, throughout the solar atmosphere and knowing the extend of its impact on observed modes. It will also be important to study how the actual integrated spectral line intensity and Doppler velocity of such MHD wave modes will appear in observational data depending the particular wavelength used and the observer's line of sight with respect to the elliptical flux tube axes.

The study and modelling of magnetohydrodynamic waves in waveguides of irregular cross-sectional shape with continuity of the radial velocity component and the total (gas plus magnetic) pressure across the boundary of the actual shape is an important extension of Chapter 4. The investigation of the effect of magnetic field twisting on the observed patterns in the actual sunspot shape is very important.

APPENDIX A

Power series expansions for Mathieu functions in the form of hyperbolic and trigonometric series

The expansion of the Mathieu functions in the form of hyperbolic series in s direction:

$$C_{2n}(s,\, m_0^2) = \sum_{r=0}^{\infty} A_{2r}^{2n} \cosh(2rs) \tag{A.1}$$

$$C_{2n+1}(s,\, m_0^2) = \sum_{r=0}^{\infty} A_{2r+1}^{2n+1} \cosh((2r+1)s) \tag{A.2}$$

$$S_{2n+1}(s,\, m_0^2) = \sum_{r=0}^{\infty} B_{2r+1}^{2n+1} \sinh((2r+1)s) \tag{A.3}$$

$$S_{2n+2}(s,\, m_0^2) = \sum_{r=0}^{\infty} B_{2r+2}^{2n+2} \sinh((2r+2)s) \tag{A.4}$$

The expansion of the Mathieu functions in the form of trigonometric series in ϕ direction.

$$c_{2n}(\phi,\, m_0^2) = \sum_{r=0}^{\infty} A_{2r}^{2n} \cos(2r\phi) \tag{A.5}$$

$$c_{2n+1}(\phi,\, m_0^2) = \sum_{r=0}^{\infty} A_{2r+1}^{2n+1} \cos((2r+1)\phi) \tag{A.6}$$

$$s_{2n+2}(\phi,\, m_0^2) = \sum_{r=0}^{\infty} B_{2r+2}^{2n+2} \sin((2r+2)\phi) \tag{A.7}$$

$$s_{2n+1}(\phi,\, m_0^2) = \sum_{r=0}^{\infty} B_{2r+1}^{2n+1} \sin((2r+1)\phi) \tag{A.8}$$

The coefficients A_{2r}^{2n}, A_{2r+1}^{2n+1}, B_{2r+1}^{2n+1} and B_{2r+2}^{2n+2} are related by recurrence relations which can be obtained by substituting Equations (A.2)-(A.4) in Equation (3.10) or Equations (A.5)-(A.8) in Equation (3.9). The recurrence relations among the expansion coefficients are

- even-even ($c_{2n}(\phi,\, m_0^2)$)

$$\begin{cases} hA_{ee}^{(0)} - m_0^2 A_{ee}^{(2)} = 0, \\ (h-4)\, A_{ee}^{(2)} - m_0^2 \left[2A_{ee}^{(0)} + A_{ee}^{(4)}\right] = 0, \\ [h-(2j)^2]\, A_{ee}^{(2j)} - m_0^2 \left[2A_{ee}^{(2j-2)} + A_{ee}^{(2j+2)}\right] = 0 \quad \text{j=2,3,4...} \end{cases}, \tag{A.9}$$

- even-odd ($c_{2n+1}(\phi,\, m_0^2)$)

$$\begin{cases} (h-1)\, A_{eo}^{(1)} - m_0^2 \left[A_{eo}^{(1)} + A_{eo}^{(3)}\right] = 0, \\ [h-(2j+1)^2]\, A_{eo}^{(2j+1)} - m_0^2 \left[2A_{eo}^{(2j-1)} + A_{eo}^{(2j+3)}\right] = 0 \quad \text{j=2,3,4...} \end{cases}, \tag{A.10}$$

- odd-even ($s_{2n+2}(\phi,\, m_0^2)$)

$$\begin{cases} (h-4)\, B_{oe}^{(2)} - m_0^2 B_{oe}^{(4)} = 0, \\ [h-(2j)^2]\, B_{oe}^{(2j)} - m_0^2 \left[2B_{oe}^{(2j-2)} + B_{oe}^{(2j+2)}\right] = 0 \quad \text{j=2,3,4...} \end{cases}, \tag{A.11}$$

- odd-odd ($s_{2n+1}(\phi,\, m_0^2)$)

$$\begin{cases} (h-1)\, B_{oo}^{(1)} - m_0^2 \left[B_{oo}^{(1)} + B_{oo}^{(3)}\right] = 0, \\ [h-(2j+1)^2]\, B_{oo}^{(2j+1)} - m_0^2 \left[2B_{oo}^{(2j-1)} + B_{oo}^{(2j+3)}\right] = 0 \quad \text{j=1,2,3,4...} \end{cases}, \tag{A.12}$$

where *ee*, *eo*, *oe* and *oo* indicates even-even, even-odd, odd-even and odd-odd respectively for more detail about this see (see e.g., McLachlan, 1947; Abramowitz and Stegun, 1964; Arscott, 1964).

APPENDIX B

Power series expansions for Mathieu functions in terms of Bessel function of the first and second kind

The expansion of the Mathieu functions in terms of Bessel function of the first kind (J_m):

$$C_{2n}(s,\, m_0^2) = \frac{P_{2n}}{A_0^{2n}} \sum_{r=0}^{\infty} (-1)^r A_{2r}^{2n} J_r(v_1) J_r(v_2) \tag{B.1}$$

$$C_{2n+1}(s,\, m_0^2) = \frac{P_{2n+1}}{A_1^{2n+1}} \sum_{r=0}^{\infty} (-1)^r A_{2r+1}^{2n+1} \times \left[J_r(v_1) J_{r+1}(v_2) + J_r(v_2) J_{r+1}(v_1) \right]. \tag{B.2}$$

$$S_{2n+1}(s,\, m_0^2) = \frac{s_{2n+1}}{B_1^{2n+1}} \sum_{r=0}^{\infty} (-1)^r B_{2r+1}^{2n+1} \times \left[J_r(v_1) J_{r+1}(v_2) - J_r(v_2) J_{r+1}(v_1) \right] \tag{B.3}$$

$$S_{2n+2}(s,\, m_0^2) = -\frac{s_{2n+2}}{B_2^{2n+2}} \sum_{r=0}^{\infty} (-1)^r B_{2r+2}^{2n+2} \times \left[J_r(v_1) J_{r+2}(v_2) - J_r(v_2) J_{r+2}(v_1) \right] \tag{B.4}$$

APPENDIX C

The non-oscillatory case

For the non-oscillatory case, the parameter m_0^2 or m_e^2 in the Mathieu equation is negative. A change in sign of parameters m_0^2 or m_e^2 corresponds to replacement of s by $(\frac{\pi i}{2} + s)$. By taking this into account the Fourier series expansion corresponding e.g FeK_{2n} (for more details see Chapter 8 of McLachlan (1947)) when the parameter m_e^2 is positive we have

$$C_{2n}(s_0, -m_e^2) = (-1)^n C_{2n}\left(\left(\frac{\pi i}{2} + s_0\right), m_e^2\right) \tag{C.1}$$

The expansion of the modified Mathieu functions in terms of Bessel function of the first kind (I_m).

$$C_{2n}(s, -m_0^2) = \frac{P'_{2n}}{A_0^{2n}} \sum_{r=0}^{\infty} (-1)^r A_{2r}^{2n} I_r(v_1) I_r(v_2) \tag{C.2}$$

$$C_{2n+1}(s, -m_0^2) = \frac{s'_{2n+1}}{B_1^{2n+1}} \sum_{r=0}^{\infty} (-1)^r B_{2r+1}^{2n+1} \times [I_r(v_1) I_{r+1}(v_2) + I_r(v_2) I_{r+1}(v_1)] \tag{C.3}$$

$$S_{2n+1}(s, -m_0^2) = \frac{P'_{2n+1}}{A_1^{2n+1}} \sum_{r=0}^{\infty} (-1)^r A_{2r+1}^{2n+1} \times [I_r(v_1) I_{r+1}(v_2) - I_r(v_2) I_{r+1}(v_1)] \tag{C.4}$$

$$S_{2n+2}(s, -m_0^2) = \frac{s'_{2n+2}}{B_2^{2n+2}} \sum_{r=0}^{\infty} (-1)^r B_{2r+2}^{2n+2} \times [I_r(v_1) I_{r+2}(v_2) - I_r(v_2) I_{r+2}(v_1)] \tag{C.5}$$

APPENDIX D

Power series expansions of the modified Mathieu functions of the third kind in terms of modified Bessel function of the first and second kind

The expansion of the modified Mathieu functions of the third kind in terms of modified Bessel function of the first kind (I_m) and the second kind (K_m).

$$FeK_{2n}(s,\, -m_0^2) = \frac{P_{2n}^{'}}{\pi A_0^{2n}} \sum_{r=0}^{\infty} A_{2r}^{2n} I_r(v_1) K_r(v_2), \tag{D.1}$$

$$FeK_{2n+1}(s,\, -m_0^2) = \frac{s_{2n+1}^{'}}{\pi B_1^{2n+1}} \sum_{r=0}^{\infty} B_{2r+1}^{2n+1} \left[I_r(v_1) K_{r+1}(v_2) - K_r(v_2) I_{r+1}(v_1) \right], \tag{D.2}$$

$$GeK_{2n+1}(s, -m_0^2) = \frac{P_{2n+1}^{'}}{\pi A_1^{2n+1}} \sum_{r=0}^{\infty} A_{2r+1}^{2n+1} \left[I_r(v_1) K_{r+1}(v_2) + K_r(v_2) I_{r+1}(v_1) \right], \tag{D.3}$$

$$GeK_{2n+2}(s,\, -m_0^2) = \frac{s_{2n+2}^{'}}{\pi B_2^{2n+2}} \sum_{r=0}^{\infty} B_{2r+2}^{2n+2} \left[I_r(v_1) K_{r+2}(v_2) - K_r(v_2) I_{r+2}(v_1) \right], \tag{D.4}$$

where $v_1 = |m_0|\, e^{-s}$, $v_2 = |m_0|\, e^{s}$, and

$$P_{2n}^{'} = \frac{(-1)^n c_{2n}(0,\, m_0^2) c_{2n}(\frac{\pi}{2},\, m_0^2)}{A_0^{2n}} = (-1)^n P_{2n},$$

$$P_{2n+1}^{'} = \frac{(-1)^{n+1} c_{2n+1}(0,\, m_0^2) c_{2n+1}^{'}(\frac{\pi}{2},\, m_0^2)}{m_0 A_1^{2n+1}} = (-1)^n P_{2n+1},$$

$$s_{2n+1}^{'} = \frac{(-1)^n s_{2n+1}^{'}(0,\, m_0^2) s_{2n+1}(\frac{\pi}{2},\, m_0^2)}{m_0 B_1^{2n+1}} = (-1)^n s_{2n+1},$$

$$s_{2n+2}^{'} = \frac{(-1)^{n+1} s_{2n+2}^{'}(0,\, m_0^2) s_{2n+2}^{'}(\frac{\pi}{2},\, m_0^2)}{m_0^2 B_2^{2n+2}} = (-1)^{n+1} s_{2n+2}.$$

APPENDIX E

The chosen values for solution of Chapter 3

ϵ	k_{s_0}	v_{ph}	ϵ	k_{s_0}	v_{ph}
Sausage modes ($m=0$), even $(0,1)$			Kink modes ($m=1$), odd $(1,2)$		
0.241	2.98	3.3547	0.241	3.99	0.9028
0.55	2.98	3.3807	0.55	3.99	0.9020
0.80	2.98	3.5476	0.80	3.99	0.9003
0.89	2.98	3.7626	0.89	3.99	0.8991
Sausage modes ($m=0$), even $(0,2)$			Fluting modes ($m=2$), even $(2,1)$		
0.241	4.53	4.1316	0.241	3.99	4.2523
0.55	4.53	4.2498	0.55	3.99	4.1590
0.80	4.53	4.6510	0.80	3.99	3.9591
0.89	4.53	4.9935	0.89	3.99	3.9012
kink modes ($m=1$), even $(1,1)$			Fluting modes ($m=2$), odd $(2,1)$		
0.241	3.99	3.5748	0.241	3.99	4.2556
0.55	3.99	3.5108	0.55	3.99	4.2236
0.80	3.99	3.4887	0.80	3.99	4.0088
0.89	3.99	3.6007	0.89	3.99	3.7333
kink modes ($m=1$), odd $(1,1)$			Fluting modes ($m=3$), even $(3,1)$		
0.241	3.99	3.6080	0.241	3.99	4.9322
0.55	3.99	3.7100	0.55	3.99	4.8564
0.80	3.99	4.0059	0.80	3.99	4.5414
0.89	3.99	4.3085	0.89	3.99	4.3602
Kink modes ($m=1$), even $(1,2)$			Fluting modes ($m=3$), odd $(3,1)$		
0.241	3.99	0.9031	0.241	3.99	4.9325
0.55	3.99	0.9030	0.55	3.99	4.9117
0.80	3.99	0.9017	0.80	3.99	4.9270
0.89	3.99	0.9007	0.89	3.99	4.9807

Table E.1: The chosen values for all modes under coronal condition.

ϵ	k_{s_0}	v_{ph}
Sausage surface modes, even $(0,1)$		
0.241	2.50	1.4386
0.55	2.50	1.4394
0.80	2.50	1.4449
0.89	2.50	1.4528
Kink surface modes, even $(1,1)$		
0.241	2.50	1.3325
0.55	2.50	1.3573
0.80	2.50	1.4091
0.89	2.50	1.4468
Kink surface modes, odd $(1,1)$		
0.241	2.50	1.3225
0.55	2.50	1.2972
0.80	2.50	1.2417
0.89	2.50	1.1968
Fluting surface modes ($m=2$), even $(2,1)$		
0.241	2.50	1.2856
0.55	2.50	1.2882
0.80	2.50	1.3061
0.89	2.50	1.3308
Fluting surface modes ($m=2$), odd $(2,1)$		
0.241	2.50	1.2854
0.55	2.50	1.2817
0.80	2.50	1.2564
0.89	2.50	1.2207
Fluting surface modes ($m=3$), even $(3,1)$		
0.241	11.0	1.2741
0.55	11.0	1.2981
0.80	11.0	1.3388
0.89	11.0	1.3747
Fluting surface modes ($m=3$), odd $(3,1)$		
0.241	11.0	1.2597
0.55	11.0	1.1787
0.80	11.0	1.4349
0.89	11.0	1.3636

Table E.2: The chosen values for all modes under photospheric condition.

.

APPENDIX F

Tool for analysis of oscillatory modes

The Tool for Analysis of Oscillatory Modes (TAOM) version 1.0 (TAOM v1.0, written in MatLab) is designed to detect and trace the boundary of binary image of sunspots umbra (or other feature for which boundary can be traced) and then calculate the eigenmodes and eigenfunctions of the shape of the input sunspots image with implies a fixed boundary condition using discrete Laplacian in MatLab. The code scans parameter space for eigenvalues and orthogonal eigenvectors that match the boundary conditions for any given cross-sectional shape. This code is designed to find the best elliptical (or other shape) approximation of the sunspot, calculate the eigenmodes/ eigenfunctions and provides the comparison between the umbra of the sunspots and elliptical membrane. This code works with binary image only.

F.1 Usage

This manual includes the following parts:

(1) software environment setting;
(2) description of the tool functions;
(3) overall procedure how to use the TAOM;
(4) examples of use.

F.1.1 Software environment setting

We recommend to use MatLab 2017a or later versions to avoid any incompatible conflicts with software.

F.1.2 Description of the tool functions

Table F.1: Description of the tool functions

Function name	Description of function
`TAOM_v2`	This is the main function which should be used to analysis of oscillatory modes of input image.
`redblue.m`	This code change the colormap from bright blue, white to bright red, see copyright details https://www.mathworks.com/matlabcentral/fileexchange/25536-red-blue-colormap
`subplot_tight.m`	This code is defining margins and wrapping the existing subplot function, see copyright details https://uk.mathworks.com/matlabcentral/fileexchange/27991-tight_subplot-nh-nw-gap-marg_h-marg_w

Apart from the redblue.m programme the all other parts of the code were developed by the Author. Description and usage of redblue.m programme can be found at: https://www.mathworks.com/matlabcentral/fileexchange/25536-red-blue-colormap (including copyright details).

F.1.3 Overall procedure on the use of TAOM

Step 1: Input the parameters

1 Input image `input_image`.
2 Input how many modes do you want to obsreved `e_N`.
3 Input the grid size `h_S`.
4 To create video for modes input `vd` equal to 1, otherwise 0.
5 To save data for observed modes input `da` equal to 1, otherwise 0.

Step 2: Run the main function

The `TAOM_v2` function will work only with binary images.

F.2 Example 1 (sunspot shape)

In this part, we will show how to analyse the oscillatory modes of the shape `ex_1.png` which is located in (`TAOM_v2`) folder.

```
input_image = imread(ex_1.jpg)
```

```
e_N=51

h_S=500

vd=1

ad=1

[V0,omg,V1,omg1]=TAOM_v2(input_image,e_N,h_S,vd,da)
```

Processes and results

Step 1 First, scan the binary image and detect the boundary.

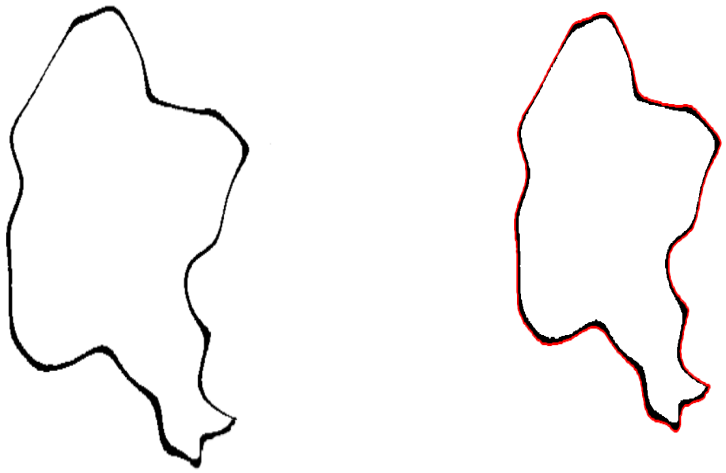

Figure F.1: Left panel (a) shows observed sunspots. Right panel (b) shows the observed sunspots with the detection the boundary of sunspots in red colour.

Step 2 Finding the best ellipse approximation for observed shape.

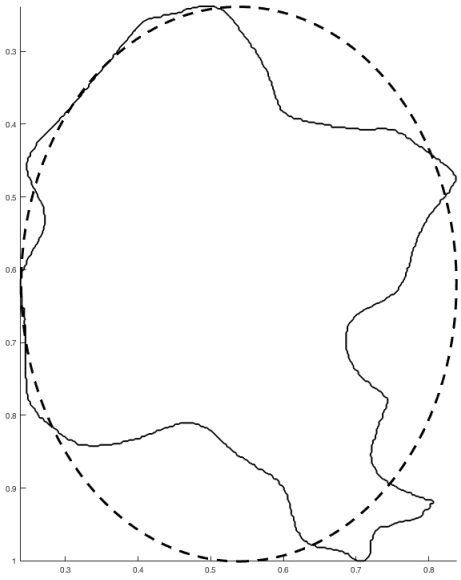

Figure F.2: Approximation of ellipse (the dash line).

Step 3 Compute the eigenvalues and eigenfunctions of each shape.

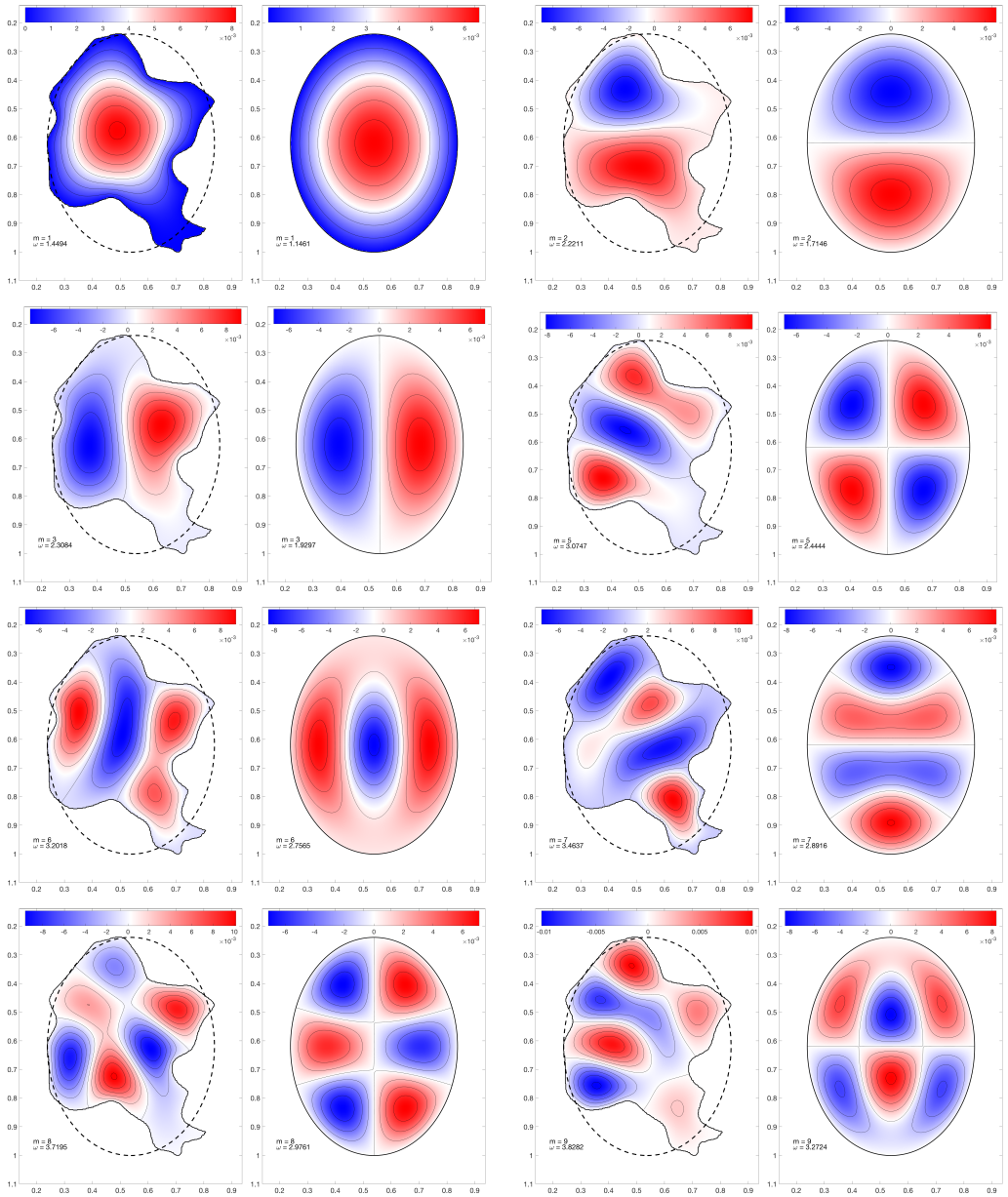

Figure F.3: Left panel on each image shows the eigenfunction of observed sunspots. Right panel on each image shows the eigenfunction of elliptical sunspot.

Step 4 Make `TAOM_avi` movie for all modes (optional) .

Step 5 Save data for the exact shape `TAOM_data.mat` file for all modes (optional).

F.3 Example 2 (modelled shape)

We used the figure `ex1_1.png` which is located in the (`TAOM_v2`) folder.

```
input_image = imread(ex1_1.jpg)

   e_N=51

   h_S=500

   vd=1

   ad=1

   [V0,omg,V1,omg1]=TAOM_v2(input_image,e_N,h_S,vd,da)
```

Processes and results

Step 1 First, scan the binary image and detect the boundary.

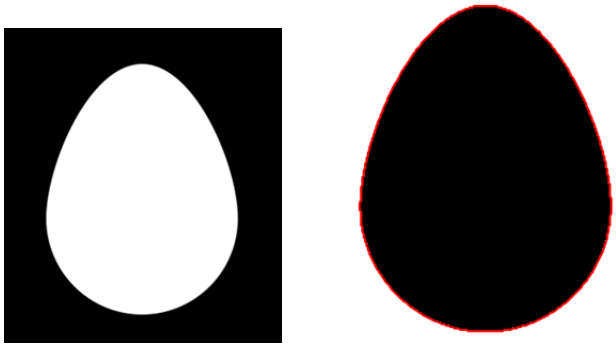

Figure F.4: Left image shows the input shape. Right image shows the the input shape with the detection the boundary in red colour.

Step 2 Finding the best ellipse approximation for detected shape.

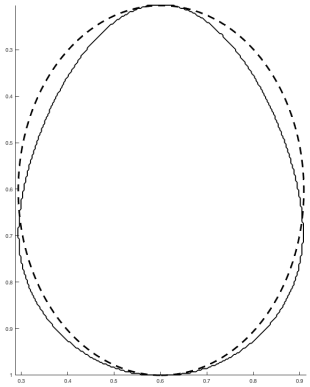

Figure F.5: Approximation of ellipse (the dash line).

Step 3 Compute the eigenvalues and eigenfunctions of each shape.

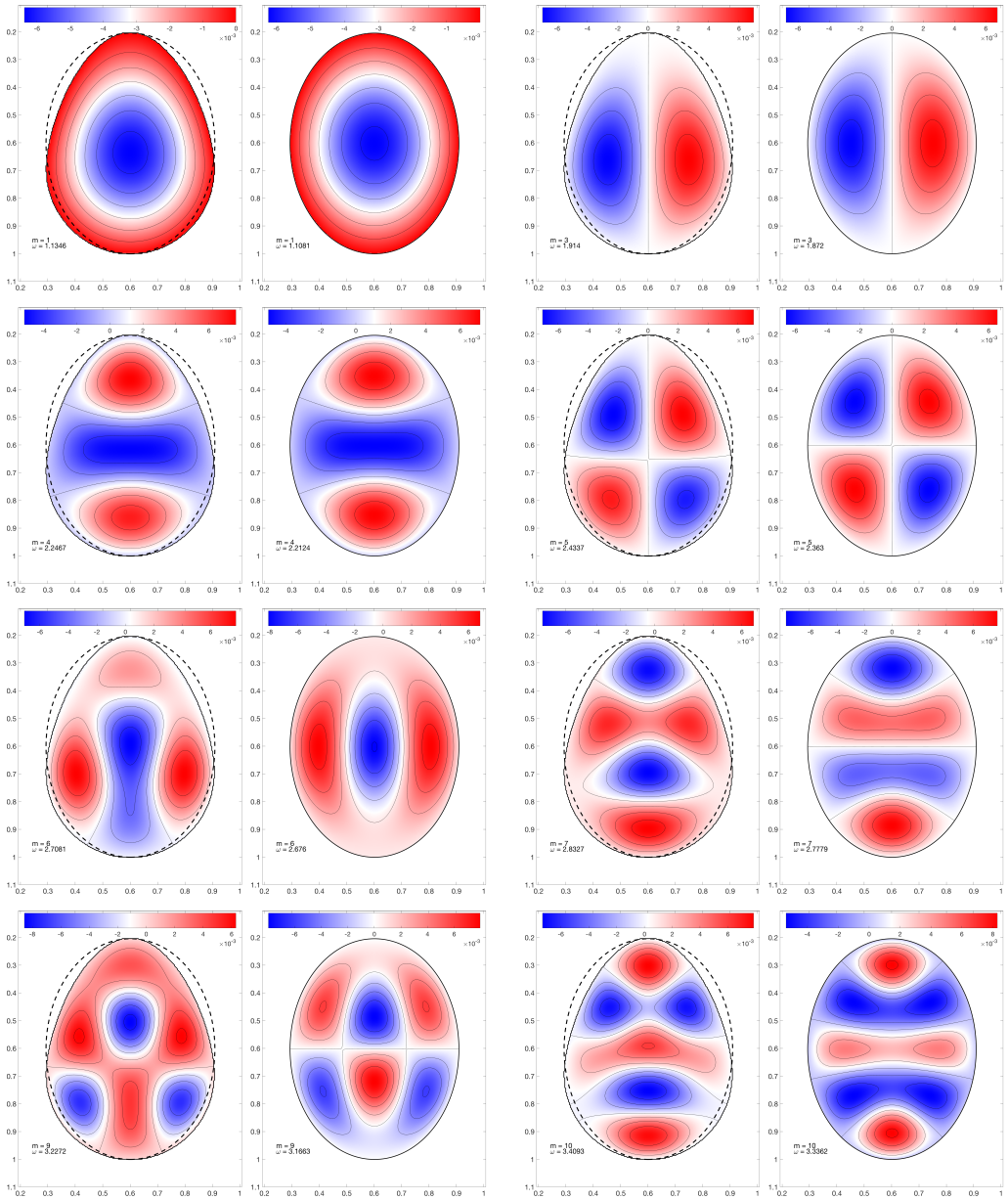

Figure F.6: Left panel on each image shows the eigenfunction of observed sunspots. Right panel on each image shows the eigenfunction of elliptical sunspot.

Step 4 Make `TAOM_avi` movie for all modes (optional) .

Step 4 Save data for the exact shape `TAOM_data.mat` file for all modes (optional).

APPENDIX G

Tool for transformation of oscillatory modes from circular-elliptical to actual shape.

Here, I describe a tool for the transformation of the circular or elliptical cross-sectional shape to the actual cross-sectional shape. Version 1.0 (TCETA v1.0, written in MatLab) is designed to detect and trace the boundary of the binary image of sunspots umbrae (or other features for which boundary can be traced) and then find the approximated circular or elliptic shape of actual sunspots. Then, calculate the eigenmodes and eigenfunctions of the all transformations shapes of the input sunspots image with implies a fixed boundary condition using discrete Laplacian in MatLab. The code scans parameter space for eigenvalues and orthogonal eigenvectors that match the boundary conditions for all shapes and then collects all similar modes on one video to show how each mode is changing when the shape of sunspots is changed, i.e., sausage mode or kink mode. This code only work with binary images only.

G.1 Usage

This manual includes the following parts:

(1) software environment setting;
(2) description of the tool functions;
(3) overall procedure how to use the TCETA;
(4) examples of use.

G.1.1 Software environment setting

We recommend to use MatLab 2017a or later versions to avoid any incompatible conflicts with software.

Table G.1: Description of the tool functions

Function name	Description of function
`TCETA_v1`	This is the main function which should be used to analysis of oscillatory modes of input image.
`redblue.m`	This code change the colormap from bright blue, white to bright red (https://www.mathworks.com/matlabcentral/fileexchange/25536-red-blue-colormap)

G.1.2 Description of the tool functions

Apart from the redblue.m programme the all other parts of the code were developed by the Author. Description and usage of redblue.m programme can be found at: https://www.mathworks.com/matlabcentral/fileexchange/25536-red-blue-colormap (including copyright details).

G.1.3 Overall procedure how to use the TCETA

Step 1: Input the parameters

1 Input image `input_image`.
2 Input how many shapes do you want for transform the ellipse to the actual shape `n_S`.
3 Input what type of mode do you want for example mode number 50 which corresponds to sausage waves `n_m`.
4 Input how many modes do you want to obsreve `e_N`.
5 Input the grid size `h_S`.
6 To create video for modes input `vd` equal to 1, otherwise 0.

Step 2: Run the main function

The `TCETA_v1` function will work only with binary images.

G.2 Example 1 (sunspot shape)

In this part, we will show how to analyse the oscillatory modes of the shape `ex_1.png`, which is located in the (`TCETA_v1`) folder.

```
input_image = imread(pp.png)

   e_N=50

   h_S=400

   vd=1

   n_S=200

   n_m=39

   [h1]=TCETA_v1(input_image,n_S,e_N,n_m,h_S,vd)
```

Processes and results

Step 1 First, scan the binary image and detect the boundary.

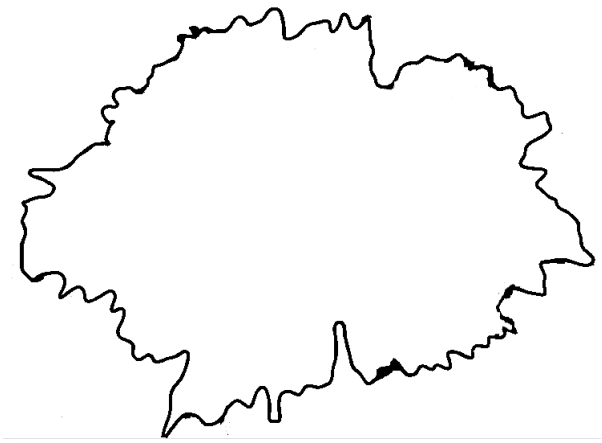

Figure G.1: The image shows observed sunspots.

Step 2 Finding the best ellipse approximation for observed shape.

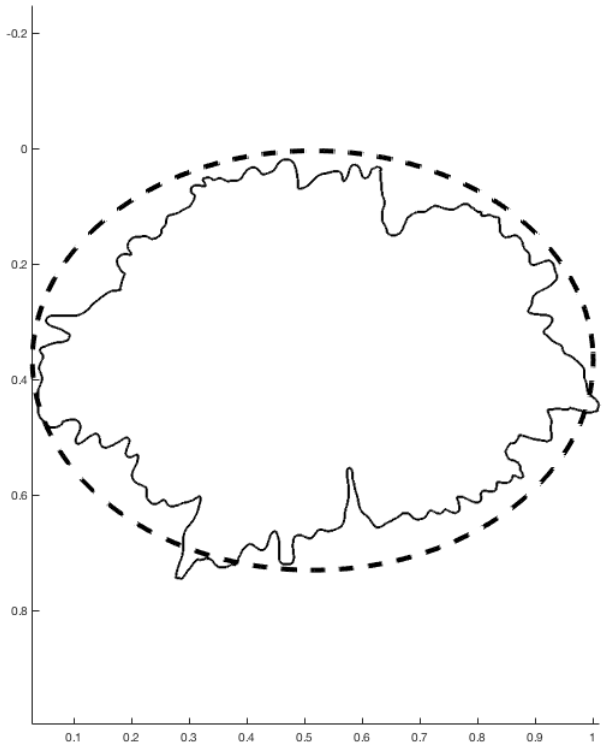

Figure G.2: Approximation of ellipse (the dashed line).

Step 3 Calculate all the transformation shapes from ellipse to actual shape.

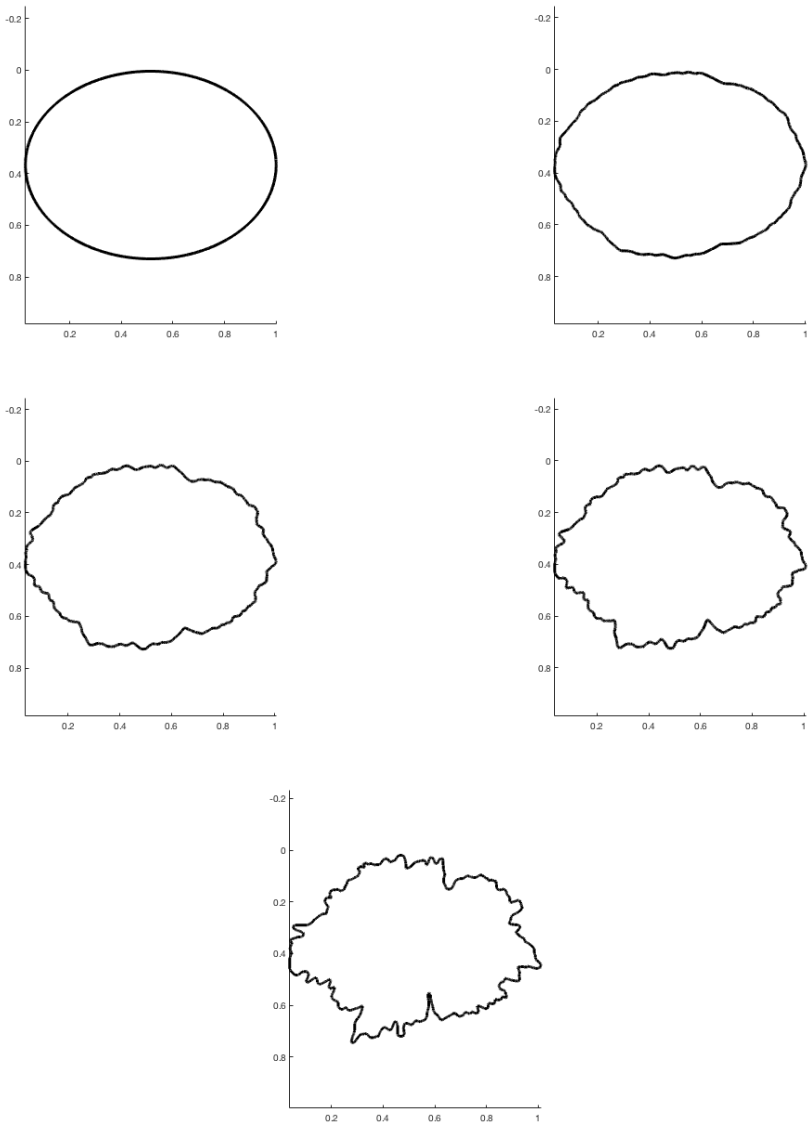

Figure G.3: Transform the ellipse into the actual shape.

Step 4 Compute the eigenvalues and eigenfunctions of each shape.

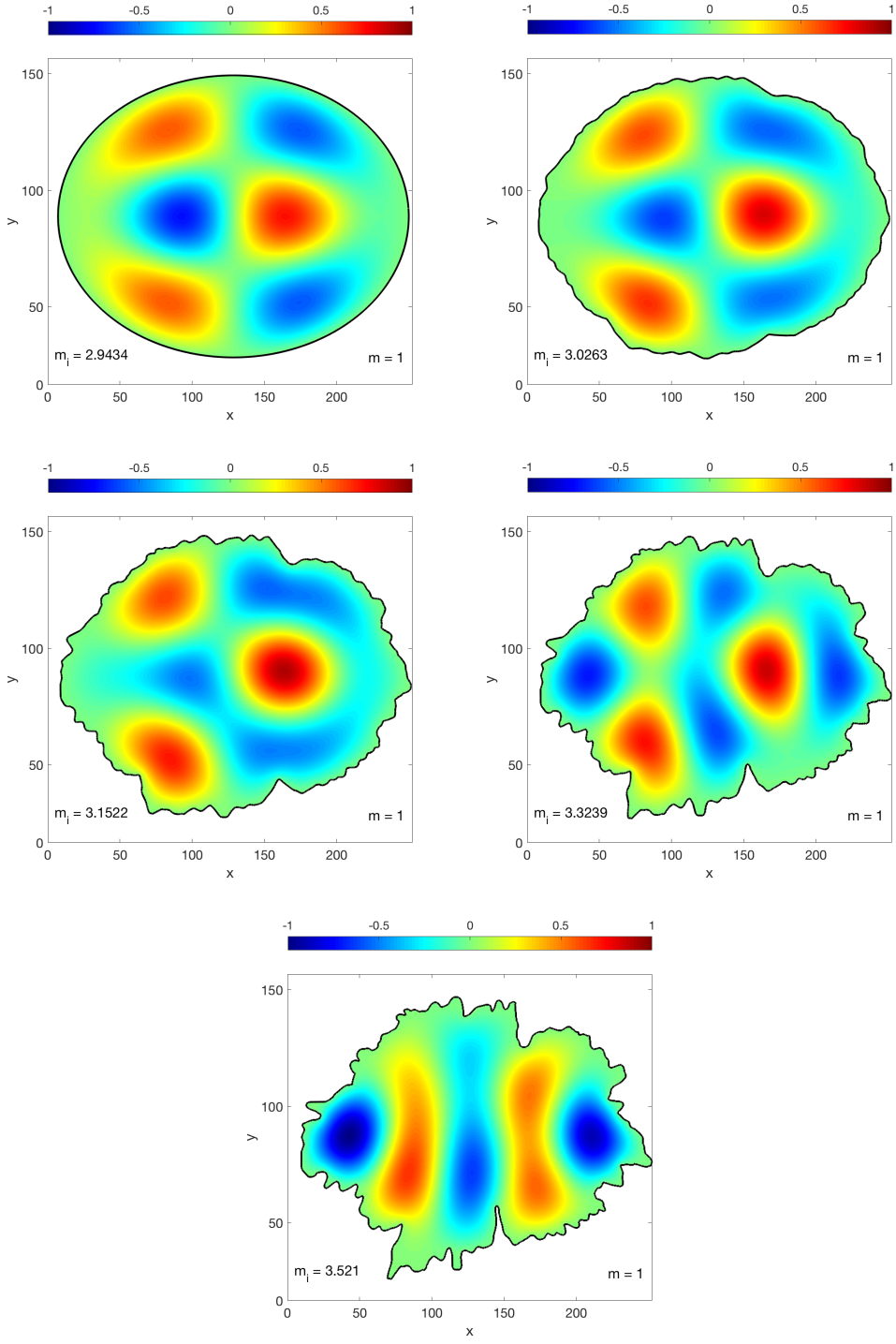

Figure G.4: From left to right we show how the shape deform from ellipse to actual sunspots. The second higher order kink mode ($m = 1$) is shown in each of the shapes.

Step 5 Make `TCATA_avi` movie for all modes (optional).

Bibliography

Abramowitz, M. and Stegun, I. (1964), *Handbook of Mathematical Functions (National Bureau of Standards)*, ninth dover printing, tenth gpo printing edn, Dover, New York City.

Albidah, A. B., Brevis, W., Fedun, V., Ballai, I., Jess, D. B., Stangalini, M., Higham, J. and Verth, G. (2021), 'Proper orthogonal and dynamic mode decomposition of sunspot data', *Philosophical Transactions of the Royal Society of London Series A* **379**(2190), 20200181.

Aldhafeeri, A. A., Verth, G., Brevis, W., Jess, D. B., McMurdo, M. and Fedun, V. (2021), 'Magnetohydrodynamic Wave Modes of Solar Magnetic Flux Tubes with an Elliptical Cross Section', *Astrophys. J.* **912**(1), 50.

Alfvén, H. (1942), 'Existence of Electromagnetic-Hydrodynamic Waves', *Nature* **150**(3805), 405–406.

Arlt, R. (2014), 'Sunspots from the past, treasures for today', *Astronomy and Geophysics* **55**(3), 3.24–3.27.

Arscott, F. M. (1964), 'Integral equations and relations for Lame functions', *The Quarterly Journal of Mathematics* **15**(1), 103–115.

Aschwanden, M. J. (2005), *Physics of the Solar Corona. An Introduction with Problems and Solutions (2nd edition)*.

Avrett, E. H. and Loeser, R. (2008), 'Models of the Solar Chromosphere and Transition Region from SUMER and HRTS Observations: Formation of the Extreme-Ultraviolet Spectrum of Hydrogen, Carbon, and Oxygen', *Astrophys. J. Suppl.* **175**(1), 229–276.

Ballai, I., Forgács-Dajka, E. and Douglas, M. (2011), 'Magnetoacoustic surface gravity waves at a spherical interface', *Astron. Astrophys.* **527**, A12.

Beckers, J. M. and Tallant, P. E. (1969), 'Chromospheric Inhomogeneities in Sunspot Umbrae', *Solar Phys.* **7**(3), 351–365.

Bharti, L., Hirzberger, J. and Solanki, S. K. (2013), 'Fine structures in the atmosphere above a sunspot umbra', *Astron. Astrophys.* **552**, L1.

Binns, K. J. K. J. and Lawrenson, P. J. (1973), *Analysis and computation of electric and magnetic field problems / by K. J. Binns and P. J. Lawrenson.*, 2d ed. edn, Pergamon Press, Oxford ; New York.

Bloomfield, D. S., Lagg, A. and Solanki, S. K. (2007), 'The Nature of Running Penumbral Waves Revealed', *Astrophys. J.* **671**(1), 1005–1012.

Boehm-Vitense, E. (1984), 'Chromospheres, Transition Regions, and Coronas', *Science* **223**(4638), 777–784.

Bogdan, T. J. and Judge, P. G. (2006), 'Observational aspects of sunspot oscillations', *Philosophical Transactions of the Royal Society of London Series A* **364**(1839), 313–331.

Bonnet, R. M. (1978), 'High Resolution UV Solar Spectroscopy', *Space Sci. Rev.* **21**(4), 379–409.

Borrero, J. M. and Ichimoto, K. (2011), 'Magnetic Structure of Sunspots', *Living Reviews in Solar Physics* **8**(1), 4.

Bourdin, P.-A., Bingert, S. and Peter, H. (2014), 'Coronal loops above an active region: Observation versus model', *Pub. Astron. Soc. Japan* **66**, S7.

Bray, R. J. and Loughhead, R. E. (1974), *The solar chromosphere.*

Burton, W. M., Jordan, C., Ridgeley, A. and Wilson, R. (1971), 'The Structure of the Chromosphere-Corona Transition Region from Limb and Disk Intensities', *Philosophical Transactions of the Royal Society of London Series A* **270**(1202), 81–98.

Buss, A. A. (1926), 'Persistent Solar Prominences', *Nature* **118**(2968), 412.

Carpmael, E. (1870), 'The Solar Prominences', *Nature* **1**(24), 607.

Centeno, R., Collados, M. and Trujillo Bueno, J. (2006), 'Spectropolarimetric Investigation of the Propagation of Magnetoacoustic Waves and Shock Formation in Sunspot Atmospheres', *Astrophys. J.* **640**(2), 1153–1162.

Chari, M. and Salon, S. (2000), 3 - the finite difference method, *in* M. Chari and S. Salon, eds, 'Numerical Methods in Electromagnetism', Electromagnetism, Academic Press, San Diego, pp. 105 – 141.
URL: *http://www.sciencedirect.com/science/article/pii/B9780126157604500043*

Chen, F. F. (1984), 'Book-Review - Introduction to Plasma Physics and Controlled Fusion', *Journal of the British Astronomical Association* **95**(1), 45.

Chen, F. F. (2016), *Introduction to Plasma Physics and Controlled Fusion*, Springer International Publishing Switzerland.

Choudhuri, A. R. (2018), 'The Sun as a Laboratory for Plasma Physics', *arXiv e-prints* p. arXiv:1808.10186.

Cowling, T. G. (1976), *Magnetohydrodynamics*, Monographs on Astronomical Subjects, Bristol.

Cram, L. E. and Wilson, P. R. (1975), 'Hydromagnetic Waves in Structured Magnetic Fields', *Solar Phys.* **41**(2), 313–327.

Cranmer, S. R. (2020), Alfven Waves in the Solar Corona and Solar Wind: An Updated Energy Budget, *in* 'American Astronomical Society Meeting Abstracts', Vol. 52 of *American Astronomical Society Meeting Abstracts*, p. 149.08.

Demerdash, N. A. and Nehl, T. W. (1979), 'An evaluation of the methods of finite elements and finite differences in the solution of nonlinear electromagnetic fields in electrical machines', *IEEE Transactions on Power Apparatus and Systems* **PAS-98**(1), 74–87.

Demirbaş, M. D., Ekici, R. and Apalak, M. K. (2020), 'Thermoelastic analysis of temperature-dependent functionally graded rectangular plates using finite element and finite difference methods', *Mechanics of Advanced Materials and Structures* **27**(9), 707–724.

Despois, D. and Gargaud, M. (2006), 'From Suns to Life: A Chronological Approach to the History of Life on Earth: 8. A Synthetic Interdisciplinary "Chronological Frieze": an Attempt', *Earth Moon and Planets* **98**(1-4), 291–297.

Ding, H., Shu, C., Yeo, K. and Xu, D. (2007), 'Numerical simulation of flows around two circular cylinders by mesh-free least square-based finite difference methods', *International journal for numerical methods in fluids* **53**(2), 305–332.

Eddy, J. A. (1980), The historical record of solar activity, *in* R. O. Pepin, J. A. Eddy and R. B. Merrill, eds, 'The Ancient Sun: Fossil Record in the Earth, Moon and Meteorites', pp. 119–134.

Edwin, P. M. and Roberts, B. (1983), 'Wave Propagation in a Magnetic Cylinder', *Solar Phys.* **88**(1-2), 179–191.

Erdélyi, R. and Fedun, V. (2006), 'Sausage MHD Waves in Incompressible Flux Tubes with Twisted Magnetic Fields', *Solar Phys.* **238**(1), 41–59.

Erdélyi, R. and Fedun, V. (2007), 'Linear MHD Sausage Waves in Compressible Magnetically Twisted Flux Tubes', *Solar Phys.* **246**(1), 101–118.

Erdélyi, R. and Morton, R. J. (2009), 'Magnetohydrodynamic waves in a compressible magnetic flux tube with elliptical cross-section', *Astron. Astrophys.* **494**(1), 295–309.

Fedun, V. (2008), MHD Sausage Waves in Compressible Magnetically Twisted Flux Tubes, *in* '37th COSPAR Scientific Assembly', Vol. 37, p. 864.

Fedun, V., Cheremnykh, O., Kryshtal, A. and Verth, G. (2017), MHD Wave Modes of Twisted Magnetic Flux Tube, *in* 'AGU Fall Meeting Abstracts', Vol. 2017, pp. SH42B–05.

Fedun, V. and Erdélyi, R. (2010), 3D numerical simulations of a torsional Alfven waves, *in* '38th COSPAR Scientific Assembly', Vol. 38, p. 3.

Felipe, T., Khomenko, E. and Collados, M. (2010), 'Magneto-acoustic Waves in Sunspots: First Results From a New Three-dimensional Nonlinear Magnetohydrodynamic Code', *Astrophys. J.* **719**(1), 357–377.

Giagkiozis, I., Goossens, M., Verth, G., Fedun, V. and Van Doorsselaere, T. (2016), 'Resonant Absorption of Axisymmetric Modes in Twisted Magnetic Flux Tubes', *Astrophys. J.* **823**(2), 71.

Giovanelli, R. G. (1972), 'Oscillations and Waves in a Sunspot', *Solar Phys.* **27**(1), 71–79.

Goedbloed, J. P. H. and Poedts, S. (2004), *Principles of Magnetohydrodynamics*, Cambridge University Press.

Goossens, M., Soler, R., Terradas, J., Van Doorsselaere, T. and Verth, G. (2014), 'The Transverse and Rotational Motions of Magnetohydrodynamic Kink Waves in the Solar Atmosphere', *Astrophys. J.* **788**(1), 9.

Guo, M., Van Doorsselaere, T., Karampelas, K. and Li, B. (2019), 'Wave Heating in Simulated Multistranded Coronal Loops', *Astrophys. J.* **883**(1), 20.

Guo, Z., Lin, P., Lowengrub, J. and Wise, S. M. (2017), 'Mass conservative and energy stable finite difference methods for the quasi-incompressible navier–stokes–cahn–hilliard system: Primitive variable and projection-type schemes', *Computer Methods in Applied Mechanics and Engineering* **326**, 144–174.

Gurman, J. B., Leibacher, J. W., Shine, R. A., Woodgate, B. E. and Henze, W. (1982), 'Transition region oscillations in sunspots.', *Astrophys. J.* **253**, 939–948.

Gurnett, D. A. and Bhattacharjee, A. (2005), *Introduction to Plasma Physics*, Cambridge University Press.

Hoole, P. and Pearmain, A. (1992), 'A review of the finite-difference method for multidielectric electrostatic field problems with sharp-edged electrodes', *Electric Power Systems Research* **24**(1), 19 – 30.
URL: *http://www.sciencedirect.com/science/article/pii/037877969290041X*

Hornsey, C., Nakariakov, V. M. and Fludra, A. (2014), 'Sausage oscillations of coronal plasma slabs', *Astron. Astrophys.* **567**, A24.

Houston, S. J., Jess, D. B., Asensio Ramos, A., Grant, S. D. T., Beck, C., Norton, A. A. and Krishna Prasad, S. (2018), 'The Magnetic Response of the Solar Atmosphere to Umbral Flashes', *Astrophys. J.* **860**(1), 28.

Huang, Y., Song, P. and Vasyliunas, V. M. (2017), MHD Wave Propagation at the Interface Between Solar Chromosphere and Corona, *in* 'AGU Fall Meeting Abstracts', Vol. 2017, pp. SH43A–2788.

Jardine, M. (1994), 'Book Review: Plasma physics. An introductory course / Cambridge U Press, 1993', *The Observatory* **114**(1121), 193.

Jess, D. B., Mathioudakis, M., Christian, D. J., Keenan, F. P., Ryans, R. S. I. and Crockett, P. J. (2010), 'ROSA: A High-cadence, Synchronized Multi-camera Solar Imaging System', *Solar Phys.* **261**(2), 363–373.

Jess, D. B., Morton, R. J., Verth, G., Fedun, V., Grant, S. D. T. and Giagkiozis, I. (2015), 'Multiwavelength Studies of MHD Waves in the Solar Chromosphere. An Overview of Recent Results', *Space Sci. Rev.* **190**(1-4), 103–161.

Jess, D. B., Van Doorsselaere, T., Verth, G., Fedun, V., Krishna Prasad, S., Erdélyi, R., Keys, P. H., Grant, S. D. T., Uitenbroek, H. and Christian, D. J. (2017), 'An Inside Look at Sunspot Oscillations with Higher Azimuthal Wavenumbers', *Astrophys. J.* **842**(1), 59.

Kang, J., Chae, J., Nakariakov, V. M., Cho, K., Kwak, H. and Lee, K. (2019), 'The Physical Nature of Spiral Wave Patterns in Sunspots', *Astrophys. J. Lett.* **877**(1), L9.

Karampelas, K., Van Doorsselaere, T. and Guo, M. (2019), 'Wave heating in gravitationally stratified coronal loops in the presence of resistivity and viscosity', *Astron. Astrophys.* **623**, A53.

Kazem, S. and Dehghan, M. (2018), 'Application of finite difference method of lines on the heat equation', *Numerical Methods for Partial Differential Equations* **34**(2), 626–660.
URL: *https://onlinelibrary.wiley.com/doi/abs/10.1002/num.22218*

Kentischer, T. J. and Mattig, W. (1995), 'Oscillations above sunspot umbrae.', *Astron. Astrophys.* **300**, 539.

Kerr, R. A. (2012), 'Why Is the Sun's Corona So Hot?', *Science* **336**(6085), 1099.

Keys, P. H., Morton, R. J., Jess, D. B., Verth, G., Grant, S. D. T., Mathioudakis, M., Mackay, D. H., Doyle, J. G., Christian, D. J., Keenan, F. P. and Erdélyi, R. (2018), 'Photospheric Observations of Surface and Body Modes in Solar Magnetic Pores', *Astrophys. J.* **857**(1), 28.

Kobanov, N. I. (1990), 'On Spatial Characteristics of Five-Minute Oscillations in the Sunspot Umbra', *Solar Phys.* **125**(1), 25–30.

Lehoucq, R. B., Sorensen, D. C. and Yang, C. (1998), *ARPACK users' guide: solution of large-scale eigenvalue problems with implicitly restarted Arnoldi methods*, SIAM.

Leighton, R. B., Noyes, R. W. and Simon, G. W. (1962*a*), 'Velocity Fields in the Solar Atmosphere. I. Preliminary Report.', *Astrophys. J.* **135**, 474.

Leighton, R. B., Noyes, R. W. and Simon, G. W. (1962*b*), 'Velocity Fields in the Solar Atmosphere. I. Preliminary Report.', *Astrophys. J.* **135**, 474.

Lighthill, M. J. (1960), 'Studies on Magneto-Hydrodynamic Waves and other Anisotropic Wave Motions', *Philosophical Transactions of the Royal Society of London Series A* **252**(1014), 397–430.

Liszka, T. and Orkisz, J. (1980), 'The finite difference method at arbitrary irregular grids and its application in applied mechanics', *Computers Structures* **11**(1), 83 – 95. Special Issue-Computational Methods in Nonlinear Mechanics.
URL: *http://www.sciencedirect.com/science/article/pii/0045794980901492*

Lites, B. W. (1986), 'Photoelectric Observations of Chromospheric Sunspot Oscillations. III. Spatial Distribution of Power and Frequency in Umbrae', *Astrophys. J.* **301**, 992.

Lites, B. W. (1988), 'Photoelectric Observations of Chromospheric Sunspot Oscillations. V. Penumbral Oscillations', *Astrophys. J.* **334**, 1054.

Liu, C., Xu, Y., Cao, W., Deng, N., Lee, J., Hudson, H. S., Gary, D. E., Wang, J., Jing, J. and Wang, H. (2016), 'Flare differentially rotates sunspot on Sun's surface', *Nature Communications* **7**, 13104.

Lockyer, N. and Lockyer, W. J. S. (1902), 'Solar Prominence and Spot Circulation, 1872-1901', *Proceedings of the Royal Society of London Series I* **71**, 446–452.

Lockyer, W. J. S. (1904), *Sunspot variation in latitude, 1861-1902.*, London, Harrison and sons, printers.

Maltby, P., Avrett, E. H., Carlsson, M., Kjeldseth-Moe, O., Kurucz, R. L. and Loeser, R. (1986), 'A New Sunspot Umbral Model and Its Variation with the Solar Cycle', *Astrophys. J.* **306**, 284.

Mather, J. F., Ballai, I. and Erdélyi, R. (2018), 'Dissipative instabilities in a partially ionised prominence plasma slab. II. The effect of compressibility', *Astron. Astrophys.* **610**, A56.

Mathew, S. K., Lagg, A., Solanki, S. K., Collados, M., Borrero, J. M., Berdyugina, S., Krupp, N., Woch, J. and Frutiger, C. (2003), 'Three dimensional structure of a regular sunspot from the inversion of IR Stokes profiles', *Astron. Astrophys.* **410**, 695–710.

Mathieu, E. (1868), 'Mémoire sur le mouvement vibratoire d'une membrane de forme elliptique', *Journal des Mathématiques Pures et Appliquées* **13**, 137–203.

Mattiussi, C. (2000), The finite volume, finite element, and finite difference methods as numerical methods for physical field problems, Vol. 113 of *Advances in Imaging and Electron Physics*, Elsevier, pp. 1 – 146.
URL: *http://www.sciencedirect.com/science/article/pii/S1076567000800129*

McIntosh, P. S. (1990), 'The Classification of Sunspot Groups', *Solar Phys.* **125**(2), 251–267.

McLachlan, N. (1947), *Theory and Application of Mathieu Functions*, Journal of Mathematics and Physics.

Morton, R. J., Verth, G., Jess, D. B., Kuridze, D., Ruderman, M. S., Mathioudakis, M. and Erdélyi, R. (2012), 'Observations of ubiquitous compressive waves in the Sun's chromosphere', *Nature Communications* **3**, 1315.

Musielak, Z. E., Huang, P. and Ulmschneider, P. (2000), 'Time-dependent analytical solutions for MHD surface waves propagating in a compressible plasma', *Astron. Astrophys.* **362**, 359–370.

Oran, R., Landi, E., van der Holst, B., Sokolov, I. V. and Gombosi, T. I. (2017), 'Alfvén Wave Turbulence as a Coronal Heating Mechanism: Simultaneously Predicting the Heating Rate and the Wave-induced Emission Line Broadening', *Astrophys. J.* **845**(2), 98.

Parker, E. N. (1974), 'The Nature of the Sunspot Phenomenon. II: Internal Overstable Modes', *Solar Phys.* **37**(1), 127–144.

Parker, E. N. (2004), 'Principles of Magnetohydrodynamics, with Applications to Laboratory and Astrophysical Plasma. By H. GOEDBLOED & S. POEDT. Cambridge University Press, 2004. 632 pp. ISBN 0521 623472, £80 (hardback); ISBN 0521 626072, £40 (paperback)', *Journal of Fluid Mechanics* **519**, 377–379.

Pascoe, D. J. and Nakariakov, V. M. (2016), 'Standing sausage modes in curved coronal slabs', *Astron. Astrophys.* **593**, A52.

Perrone, N. (1978), 'Finite Element and Finite Difference Methods in Engineering', *Journal of Mechanical Design* **100**(1), 188–192.
URL: *https://doi.org/10.1115/1.3453885*

Peter, H., Bingert, S. and Gudiksen, B. V. (2008), On the nature of coronal loops, *in* 'AGU Spring Meeting Abstracts', Vol. 2008, pp. SP41C–05.

Porfir'eva, G. A. and Yakunina, G. V. (2016), 'Chromospheric spicules and solar corona', *Astronomical and Astrophysical Transactions* **29**(4), 567–580.

Priest, E. (2014), *Magnetohydrodynamics of the Sun*, Cambridge University Press.

Rappazzo, A. F. and Velli, M. M. (2010), Coronal Loops Dynamics and Photospheric Forcing Patterns, *in* 'AGU Fall Meeting Abstracts', Vol. 2010, pp. SM51C–1846.

Richardson, L. F. and Glazebrook, R. T. (1911), 'Ix. the approximate arithmetical solution by finite differences of physical problems involving differential equations, with an application to the stresses in a masonry dam', *Philosophical Transactions of the Royal Society of London. Series A, Containing Papers of a Mathematical or Physical Character* **210**(459-470), 307–357.
URL: *https://royalsocietypublishing.org/doi/abs/10.1098/rsta.1911.0009*

Roberts, B. (1981*a*), 'Wave Propagation in a Magnetically Structured Atmosphere - Part One - Surface Waves at a Magnetic Interface', *Solar Phys.* **69**(1), 27–38.

Roberts, B. (1981*b*), 'Wave Propagation in a Magnetically Structured Atmosphere - Part Two - Waves in a Magnetic Slab', *Solar Phys.* **69**(1), 39–56.

Rouppe van der Voort, L. H. M., Rutten, R. J., Sütterlin, P., Sloover, P. J. and Krijger, J. M. (2003), 'La Palma observations of umbral flashes', *Astron. Astrophys.* **403**, 277–285.

Ruderman, M. S. (2003), 'The resonant damping of oscillations of coronal loops with elliptic cross-sections', *Astron. Astrophys.* **409**, 287–297.

Ruderman, M., Terradas, J. and Jose-Luis Ballester, P. (2014), Kink oscillations of twisted coronal magnetic loops, *in* '40th COSPAR Scientific Assembly', Vol. 40, pp. E2.2–30–14.

Russell, A. J. B. (2018), 'Commentary: Discovery of the Sun's million-degree hot corona', *Frontiers in Astronomy and Space Sciences* **5**, 9.

Russell, T. F. and Wheeler, M. F. (1983), Finite element and finite difference methods for continuous flows in porous media, *in* 'The mathematics of reservoir simulation', SIAM, pp. 35–106.

Ryutova, M., Berger, T. and Title, A. (2008), 'On the Fine Structure and Formation of Sunspot Penumbrae', *Astrophys. J.* **676**(2), 1356–1366.

Scheuer, M. A. and Thomas, J. H. (1981), 'Umbral Oscillations as Resonant Modes of Magneto-Atmospheric Waves', *Solar Phys.* **71**(1), 21–38.

Schlichenmaier, R., von der Lühe, O., Hoch, S., Soltau, D., Berkefeld, T., Schmidt, D., Schmidt, W., Denker, C., Balthasar, H., Hofmann, A., Strassmeier, K. G., Staude, J., Feller, A., Lagg, A., Solanki, S. K., Collados, M., Sigwarth, M., Volkmer, R., Waldmann, T., Kneer, F., Nicklas, H. and Sobotka, M. (2016), 'Active region fine structure observed at 0.08 arcsec resolution', *Astron. Astrophys.* **596**, A7.

Sobotka, M. and Rezaei, R. (2017), 'The Temperature - Magnetic Field Relation in Observed and Simulated Sunspots', *Solar Phys.* **292**(12), 188.

Sobotka, M., Vázquez, M., Bonet, J. A., Hanslmeier, A. and Hirzberger, J. (1999), 'Temporal Evolution of Fine Structures in and around Solar Pores', *Astrophys. J.* **511**(1), 436–450.

Socas-Navarro, H., McIntosh, S. W., Centeno, R., de Wijn, A. G. and Lites, B. W. (2009), 'Direct Imaging of Fine Structure in the Chromosphere of a Sunspot Umbra', *Astrophys. J.* **696**(2), 1683–1688.

Solanki, S. K. (2003), 'Sunspots: An overview', *Astron. Astrophys. Rev.* **11**(2-3), 153–286.

Spruit, H. C. (1982*a*), 'Propagation Speeds and Acoustic Damping of Waves in Magnetic Flux Tubes', *Solar Phys.* **75**(1-2), 3–17.

Spruit, H. C. (1982*b*), 'Propagation Speeds and Acoustic Damping of Waves in Magnetic Flux Tubes', *Solar Phys.* **75**(1-2), 3–17.

Stangalini, M., Giannattasio, F., Del Moro, D. and Berrilli, F. (2012), 'Three-minute wave enhancement in the solar photosphere', *Astron. Astrophys.* **539**, L4.

Széliga, M. R. (2014), Defin - computational application of finite difference method in hydraulics engineering.

Tavabi, E., Koutchmy, S. and Ajabshirizadeh, A. (2012), solar spicules and jets, *in* M. Faurobert, C. Fang and T. Corbard, eds, 'EAS Publications Series', Vol. 55 of *EAS Publications Series*, pp. 71–78.

Thomas, J. H. (1984), 'Umbral oscillations in sunspots', *Astron. Astrophys.* **135**(1), 188.

Thomas, J. H. and Scheuer, M. A. (1982), 'Umbral Oscillations in a Detailed Model Umbra', *Solar Phys.* **79**(1), 19–29.

Thomas, J. H., Weiss, N. O., Tobias, S. M. and Brummell, N. H. (2002), 'Downward pumping of magnetic flux as the cause of filamentary structures in sunspot penumbrae', *Nature* **420**(6914), 390–393.

Tiwari, A. K., Morton, R. J., Régnier, S. and McLaughlin, J. A. (2019), 'Damping of Propagating Kink Waves in the Solar Corona', *Astrophys. J.* **876**(2), 106.

Usmanov, A. V., Matthaeus, W. H. and Goldstein, M. L. (2016), Heating and Acceleration of the Solar Corona and Solar Wind: Effects of Turbulence Transport, *in* 'AGU Fall Meeting Abstracts', pp. SH43B–2573.

Vaquero, J. M. and Vázquez, M. (2009), *The Sun Recorded Through History: Scientific Data Extracted from Historical Documents*, Vol. 361.

Verth, G. (2007), 'Magneto-seismology of the solar atmosphere', *Astronomische Nachrichten* **328**(8), 764.

Verth, G. (2008), Magneto-seismology: effect of inhomogeneous magnetic field on transversal coronal loop oscillations, *in* R. Erdélyi and C. A. Mendoza-Briceno, eds, 'Waves & Oscillations in the Solar Atmosphere: Heating and Magneto-Seismology', Vol. 247 of *IAU Symposium*, pp. 123–132.

Verth, G., Terradas, J. and Goossens, M. (2010), 'Observational Evidence of Resonantly Damped Propagating Kink Waves in the Solar Corona', *Astrophys. J. Lett.* **718**(2), L102–L105.

Vickers, E., Ballai, I. and Erdélyi, R. (2018), 'Propagation of Leaky MHD Waves at Discontinuities with Tilted Magnetic Field', *Solar Phys.* **293**(10), 139.

Wedemeyer-Böhm, S., Lagg, A. and Nordlund, Å. (2009), 'Coupling from the Photosphere to the Chromosphere and the Corona', *Space Sci. Rev.* **144**(1-4), 317–350.

Wentzel, D. G. (1979), 'Hydromagnetic surface waves on cylindrical fluxtubes.', *Astron. Astrophys.* **76**(1), 20–23.

Williams, T., Taroyan, Y. and Fedun, V. (2016), 'The Non-linear Evolution of a Twist in a Magnetic Shocktube', *Astrophys. J.* **817**(2), 92.

Wilson, P. R. (1979), 'Hydromagnetic wave modes in magnetic flux tubes.', *Astron. Astrophys.* **71**, 9–13.

Winebarger, A. R., Warren, H. P., Cirtain, J. W., Kobayashi, K., Korreck, K. E., Golub, L., Kuzin, S., Walsh, R. W., DeForest, C., De Pontieu, B., Title, A. M. and Weber, M. (2012), The Fundamental Structure of Coronal Loops, *in* 'AGU Fall Meeting Abstracts', Vol. 2012, pp. SH31B–06.

Witze, A. (2017), 'Mysteries of Sun's corona on view during upcoming eclipse', *Nature* **548**(7666), 146–147.

Yurchyshyn, V., Abramenko, V., Kosovichev, A. and Goode, P. (2014), 'High Resolution Observations of Chromospheric Jets in Sunspot Umbra', *Astrophys. J.* **787**(1), 58.

Zirin, H. (1998), Dynamics of solar spicules, *in* T.-D. Guyenne, ed., 'Solar Jets and Coronal Plumes', Vol. 421 of *ESA Special Publication*, p. 39.

Zirin, H. and Stein, A. (1972), 'Observations of Running Penumbral Waves', *Astrophys. J. Lett.* **178**, L85.